Features of the Technology and Properties of Photodetectors Based on Metal–Porous Silicon Carbide Structures

A. V. Afanas'ev, V. A. Il'in, N. M. Korovkina, and A. Yu. Savenko

St. Petersburg State Electrotechnical University, St. Petersburg, 197376 Russia

e-mail: root@post.etu.spb.ru

Received March 11, 2005

Abstract—Some technological aspects of the formation of UV photodetector structures based on gold–porous silicon carbide (Au–PSC) Schottky diodes are considered. The data of atomic force microscopy and ion microprobe measurements in the regimes of depth profiling and contrast formation show that the adopted technology yields PSC layers with a thickness of 230–250 nm, a well developed surface, and an average roughness size of 60–80 nm. A comparative analysis of the photoelectric properties of Au–SiC(6H) and Au–PSC diode structures shows that the latter exhibits a higher photosensitivity and somewhat different spectral characteristic. © 2005 Pleiades Publishing, Inc.

Porous silicon carbide (PSC) is a promising material for the epitaxial technology of light-emitting diodes and photodetectors [1]. However, data on PSC-based photodetectors in the available literature are virtually absent. In order to fill this gap, we have studied Au–PSC photodiodes and compared their properties to those of the Au–SiC photodetectors.

PSC layers are usually prepared by anodizing single crystal SiC plates in acids or alkaline electrolytes. The process is most frequently carried out in aqueous or ethanol solutions of hydrofluoric acid, either under UV illumination [2] or in the dark [3].

We have studied the UV detectors based on epitaxial $n–n^+$ SiC(6H) structures. The uncompensated hole density in the epilayers was $N_d - N_a \approx 5 \times 10^{15}$ cm^{-3}, and the layer thickness was 2–4 μm. A part of the plate was anodized in a 2% HF solution at 10 mA/cm^2 for 1 min without UV illumination. The anodized area acquired a light gray color, which was indirect evidence for the formation of a PSC layer. According to our estimates, this regime ensures the formation of a PSC layer with a thickness not exceeding 500 nm, that is, in the near-surface region of the epitaxial SiC(6H) layer.

The samples were cleaned by ultrasonic treatment and rinsing in deionized water and oxidized in dry oxygen for 30 min at 900°C, which resulted in the formation of a 5-nm-thick intrinsic silicon oxide layer with a clear oxide–substrate interface. Then, a thick (0.3 μm) SiO$_2$ layer was grown using plasmachemical deposition for the creation of the required device topology by means of conventional photolithography. The ohmic contacts were formed by nickel deposition using a method described in [4]. Finally, semitransparent gold (Au) electrodes with a thickness of ~150 Å were

formed by thermal deposition in vacuum onto 500 × 500-μm windows made in the silicon oxide film. Thus, we obtained photodetector structures based on Schottky diodes of the gold–silicon carbide (Au–SiC) and gold–porous silicon carbide (Au–PSC) types. The current–voltage (I–U) and capacitance–voltage (C–U) characteristics of the diodes of both exhibited no significant differences: the Schottky barrier heights determined from the C–U measurements were 1.63–1.65 eV, the reverse dark currents at a 1-V bias did not exceed 10^{-12} A, and the I–U curve ideality factors fell within 1.09–1.12.

The depth–composition profiles of the near-surface layers of photosensitive areas in the Au–SiC and Au−PSC diodes were obtained using a Strata FIB 205 instrument in the regime of high-precision sputtering by a focused beam of gallium ions. The walls of craters and the adjacent sample surface areas were imaged using the same instrument in the regime of secondary electron emission induced by ion bombardment. Typical images are presented in Fig. 1. As can be seen from Fig. 1b, the anodic processing leads to the formation of a PSC layer with a thickness of $d \approx$ 230–250 nm.

The thickness W of a depleted layer of the Schottky diode can be estimated using the formula [5]

$$W = \sqrt{\frac{2\varepsilon\varepsilon_0}{q(N_d - N_a)}\left(U_d - \frac{kT}{q} - U\right)}, \qquad (1)$$
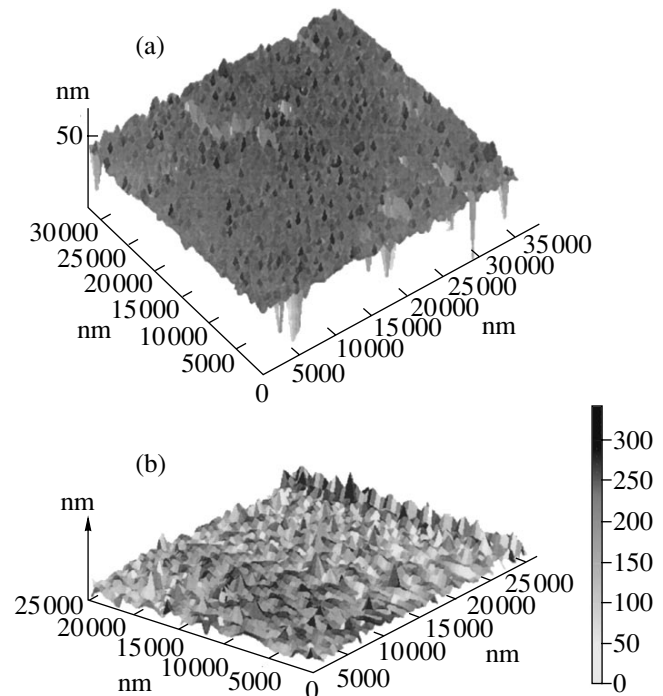
where $\varepsilon = 9.8$ is the permittivity and $U_d = 1.48$ V is the diffusion potential determined from the C–U curves. Substituting the known values of the parameters into
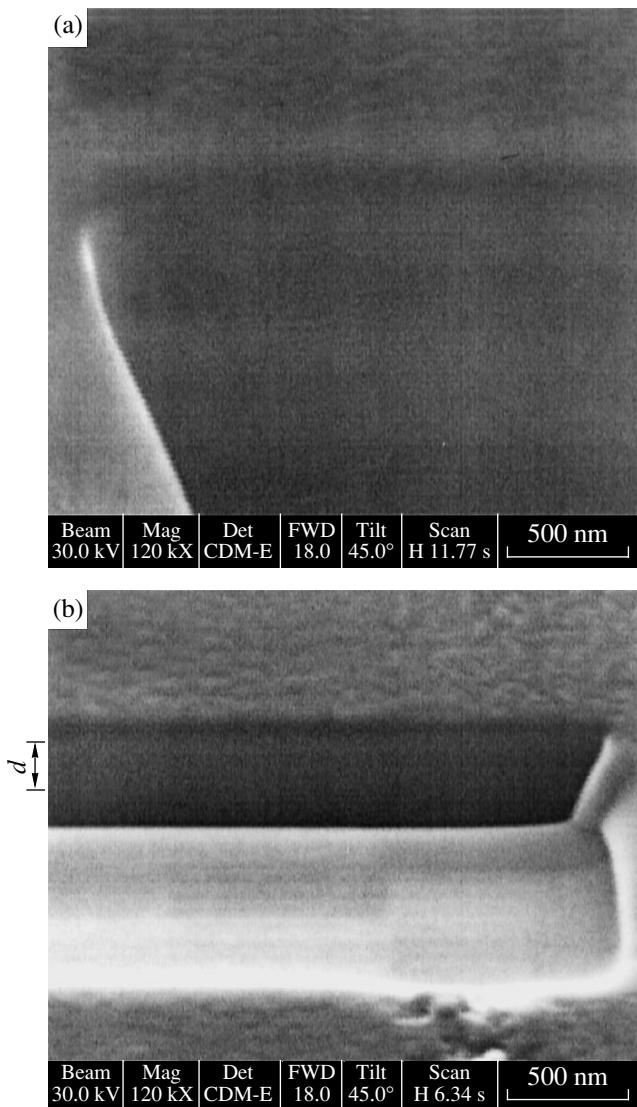
Fig. 1. Secondary-electron micrographs of the cross sections of near-surface regions of photosensitive areas in (a) Au–SiC and (b) Au–PSC photodetectors.

Fig. 2. AFM images of the surface of photosensitive areas in (a) Au–SiC and (b) Au–PSC photodetectors.

formula (1) for $U = 0$ yields $W = 566$ nm, which considerably exceeds the PSC layer thickness. This circumstance explains the absence of significant differences between the electric characteristics (barrier height, I–V curve ideality factor, reverse dark current) of Schottky diodes based on the Au–SiC and Au–PSC structures.

The photoelectric properties of samples were studied in a spectral range from 200 to 1200 nm. The PSC-based photodetectors were sensitive in the 200- to 430-nm wavelength interval. The absorption edge in these samples is shifted to longer wavelength as compared to that in the Au–SiC photodetectors, where the photosensitivity interval was restricted to 420 nm. Similar results were reported in [1] for freestanding PSC films with a thickness of about 150 μm. Appar-

ently, the presence of a porous layer of even a small thickness influences the spectral characteristic of photodetectors.

The current responsivity (S_I) at 254 nm determined in the short-circuit regime for the PSC-based samples amounted to 45–55 mA/W, which was more than 1.5 times the level for Au–SiC structures ($S_I = 27$–32 mA/W). This difference is probably related to a surface microrelief formed in the course of anodization, which is known to increase the S_I value of photodetectors [6]. This assumption is confirmed by the results of our investigation of the surface morphology of photosensitive areas by means of atomic force microscopy (AFM). As can be seen from Fig. 2, the anodization processing of SiC leads to the formation of a more developed surface with a characteristic roughness size of 60–80 nm (Fig. 2b), in contrast to 6–8 nm for the surface of a photosensitive area in the Au–SiC structures (Fig. 2a). This difference corresponds to a much greater effective area of the photodetector in the former case and, in addition, to a lower losses for reflection, thus leading to a significant increase in the efficiency of photoconversion.

To summarize, we have proposed a way to increase the efficiency of SiC-based UV photodetectors by means of a short-time anodization of the SiC substrate. This is probably the only real method of obtaining a silicon carbide surface with developed relief, since the

chemical etching of SiC (unlike silicon and $A^{III}B^{V}$ semiconductor compounds) is impossible.

REFERENCES

1. S. Kim, J. E. Spanier, and I. P. Herman, Jpn. J. Appl. Phys. **39**, 5875 (2000).

2. L. M. Sorokin, N. S. Savkina, A. A. Lebedev, *et al.*, Pis'ma Zh. Tekh. Fiz. **28** (22), 23 (2002) [Tech. Phys. Lett. **28**, 935 (2002)].

3. R. S. Okojie, A. A. Ned, and A. D. Kurtz, Sens. Actuators A **66**, 200 (1998).

4. A. V. Afanas'ev, V. A. Il'in, A. A. Petrov, and I. G. Kazarin, Zh. Tekh. Fiz. **71** (5), 78 (2001) [Tech. Phys. **46**, 584 (2001)].

5. S. Sze, *Physics of Semiconductor Devices* (Wiley, New York, 1981), Vol. 1.

6. N. A. Dmitruk, O. Yu. Borkovskaya, R. V. Konakova, *et al.*, Zh. Tekh. Fiz. **72** (6), 44 (2002) [Tech. Phys. **47**, 698 (2002)].

Translated by P. Pozdeev

Spectra and Kinetics of Emission from the Products of Explosive Decomposition of Silver Azide

B. P. Aduev, D. É. Aluker, S. S. Grechin, and E. V. Tupitsin

Kemerovo State University, Kemerovo, Russia

Institute of Solid State Chemistry and Mechanochemistry (Kemerovo Department), Siberian Division,
Russian Academy of Sciences, Kemerovo, Russia

e-mail: lira@kemsu.ru; filial@kemnet.ru

Received March 22, 2005

Abstract—The spectrum and kinetics of optical emission from the products of explosive decomposition of silver azide (AgN_3) initiated by a pulsed electron beam (0.5 MeV, 1 kA/cm^2, 20 ns) have been experimentally studied. The stage of preexplosion luminescence is followed by the formation of a continuous emission spectrum due to a dense plasma of decomposition products. This spectrum exhibits variations within a time interval of 0.6–0.9 μs, which can be related to the self-heating of plasma from 3000 to 3600 K as a result of the exothermal reaction $2N_3 \longrightarrow 3N_2$. © *2005 Pleiades Publishing, Inc.*

Previously, we have studied the optical emission accompanying the explosive decomposition of silver azide (AgN_3) initiated by laser and electron beams [1–3]. It was found that the initial stage of the explosive decomposition reaction develops according to the chain mechanism and is accompanied by preexplosion luminescence, which can be used for monitoring the reaction kinetics [1, 2]. The spectrum and kinetics of this emission exhibit the following features. The excitation pulse is accompanied by the first continuous emission component in the kinetic curve, which is referred to as radioluminescence. This peak is followed by the second component, called preexplosion luminescence, also with a continuous spectrum. An increase in the excitation energy density leads to a growth in the radioluminescence intensity and to a decrease in the time (increase in the rate) of the preexplosion luminescence buildup in the time interval of $t \sim 0.5 \pm 0.1$ μs [3]. At $t > 1$ μs, the third kinetic component of luminescence with a line spectrum is observed, which has been attributed to the emission from excited nitrogen molecules [2]. It has been found that the radioluminescence and preexplosion luminescence spectra coincide, at least in the initial ascending branch of the kinetics, which indicates that a chemical reaction responsible for the explosive decomposition of silver azide is directly initiated by the exciting pulse [3].

This Letter presents the results of a more detailed investigation of the spectrum and shape of the second continuous component of the emission kinetics accompanying the explosive decomposition of silver azide initiated by a pulsed electron beam.

The experiments were performed with silver azide single crystals having the characteristic dimensions $3 \times 3 \times 1$ mm and placed in a vacuum test chamber with a residual pressure of 10^{-2} Pa at $T = 295$ K. The explosive decomposition was initiated by a pulsed electron beam with an effective electron energy of 0.25 MeV, a beam current density of 1 kA/cm^2, and a pulse duration of 20 ns. The spectrum of emission accompanying the explosion of each sample was measured in the wavelength range from 550 to 1000 nm using an experimental setup based on an ISP-51 spectrograph and a FER-7 photochronograph (streak camera). The experimental instrumentation and procedure are described in detail elsewhere [2]. The spectral characteristic of a measuring tract was preliminarily determined using a standard incandescent lamp with a known color temperature. The time resolution in our experiments was about 50 ns, as determined by the photochronograph sweep parameters

Figure 1 shows the typical kinetic curve measured at a wavelength of $\lambda = 810$ nm. The time interval studied includes two emission components with a continuous spectrum, which correspond to the radioluminescence (with a maximum intensity at $t = 50$ ns) and the subsequent preexplosion luminescence. The normalized emission spectra for several particular moments are presented in Fig. 2.

The results of data processing showed a coincidence of the emission spectra measured for the first and second kinetic components in the time interval from 0.2 to 0.6 μs (Fig. 2). This result agrees with our previous observation [3]. In the interval of times $t > 0.6$ μs, the

emission spectrum exhibits changes, whereby the times of emission from excited nitrogen molecules at $\lambda = 770$ and 810 nm are superimposed on the continuous spectrum (Fig. 2).

The experimental results can be interpreted as follows. The development of the reaction of explosive decomposition of silver azide results in that, within ~0.5 μs after the initiating pulse, the sample crystal is converted into the state of dense plasma with a continuous emission spectrum. In the time interval under consideration, the spectrum exhibits continuous transformations (a decay in the emission intensity observed for $t > 1$ μs is probably related to the plasma expansion). It should be noted that the emission spectra in Fig. 2 are not described by the Planck formula. At present, the observed transformations cannot be given unambiguous explanation. It is possible that, as the explosive decomposition reaction proceeds, the emission intensity varies as a sum of contributions due to the preexplosion luminescence from a part of the crystal and due to increasing amounts of the dense plasma.

An alternative possibility is that the explosive is virtually completely converted from the solid state into plasma within a time of $t \sim 0.6$ μs and that the subsequent variations reflect only processes in the plasma proper. The emission from plasma can be also related to various mechanisms. In particular, a quasi-continuous spectrum will be observed in the case of closely spaced lines exhibiting overlap as a result of pressure-induced broadening [4]. A continuous emission spectrum can form when free electrons are decelerated in the field of positive ions (free–free transitions). In the latter case, the emission intensity is independent of the wavelength in the region of low frequencies sufficiently far from the boundary ν_q of the series.

In the region of $\nu > \nu_q$,

$$I \sim \frac{1}{\sqrt{T}} e^{-\frac{h\nu}{kT}}, \qquad (1)$$

where I is the emission intensity, $h\nu$ is the energy of the emission quantum, T is the absolute temperature, and k is the Boltzmann constant. From this we infer that, using an experimental curve plotted as

$$\ln I \sim \frac{1}{kT} h\nu, \qquad (2)$$

it possible to estimate the temperature of plasma from the slope of this plot.

We have processed the results of spectral measurements performed for $t > 600$ ns within the framework of the above model. Figure 2 shows a curve for $t = 850$ ns plotted in terms of Eq. (2). Determining varia-
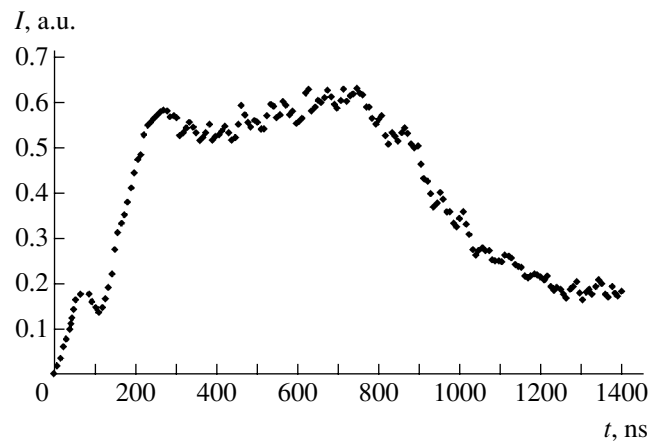

Fig. 1. Typical kinetics of the explosive luminescence from silver azide single crystals at $\lambda = 810$ nm (in relative units).
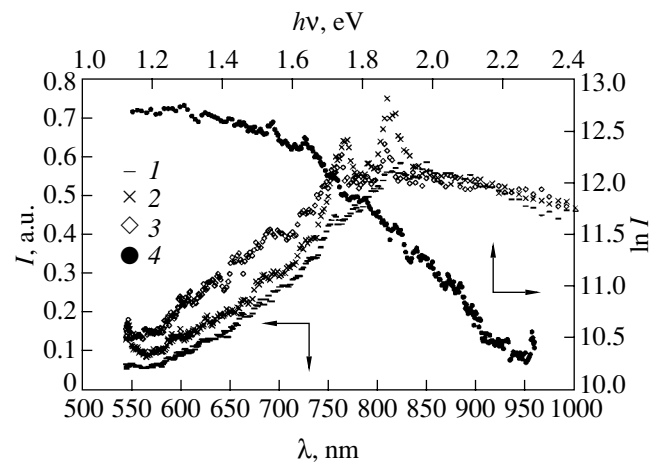

Fig. 2. The spectra of explosive luminescence from silver azide single crystals measured at various moments of time after the initiation pulse front: (1) 500 ns (spectra measured in the time interval from 50 to 600 ns coincide to within the experimental error); (2) 700 ns; (3) 850 ns. Curve (4) shows the data for $t = 850$ ns plotted as $\ln I = f(h\nu)$; linear approximation of this curve in the interval from 1.6 to 2.2 eV in terms of formula (2) yields $T = 3600$ K.

tion of the slope of this curve in the time interval from 0.6 to 0.9 μs, we conclude that the plasma temperature changes from 3000 to 3600 K. Thus, according to the proposed model, the observed transformation of the emission spectra can be related to the self-heating of plasma formed as a result of the explosive decomposition of silver azide. This variant is possible, in particular, if one of the decomposition products is the N_3 radical. In this case, the plasma features the exothermal reaction $2N_3 \longrightarrow 3N_2 + (\sim 232$ kcal) [5], which results in self-heating. It should be noted that the above estimates of the temperature corresponding to the explosive luminescence from AgN_3 agree with the experimentally measured temperature of the products of decomposition of some high explosives [6].

REFERENCES

1. B. P. Aduev, E. D. Aluker, G. M. Belokurov, *et al.*, Zh. Éksp. Teor. Fiz. **116**, 1667 (1999) [JETP **89**, 906 (1999)].

2. Yu. A. Zakharov, E. D. Aluker, B. P. Aduev, and A. G. Krechetov, *Pre-Denotation Phenomena in Azides of Heavy Metals* (TsÉI KhimMash, Moscow, 2002) [in Russian].

3. B. P. Aduev, G. M. Belokurov, S. S. Grechin, and E. V. Tupitsin, Pis'ma Zh. Tekh. Fiz. **30** (18), 46 (2004) [Tech. Phys. Lett. **30**, 774 (2004)].

4. *High Speed Physics*, Ed. by K. Vollrath and G. Thomer (Springer, Vienna, 1967; Mir, Moscow, 1971), Vol. 1.

5. F. P. Bowden and A. D. Yoffe, *Fast Reactions in Solids* (Academic Press, New York, 1958).

6. C. S. Yoo, H. C. Holmes, and P. C. Souers, Mater. Res. Soc. Symp. Proc. **418**, 397 (1996).

Translated by P. Pozdeev

Nonlinear Oscillations of the Free Surface of a Charged Drop of a Highly Viscous Liquid

A. N. Zharov, A. I. Grigor'ev*, and S. O. Shiryaeva

Yaroslavl State University, Yaroslavl, Russia
* e-mail: grig@uniyar.ac.ru
Received February 8, 2005

Abstract—An analytical expression for the shape of a charged drop of a highly viscous, incompressible conducting liquid performing nonlinear axisymmetric oscillations upon a small multimode initial deformation have been obtained by direct expansion within the second order of smallness. Using the obtained expression, it is possible to study the temporal evolution of the shape of initially deformed viscous drops bearing charges that are both sub- and supercritical from the standpoint of the Rayleigh criterion of stability. © 2005 Pleiades Publishing, Inc.

Introduction. Analytical investigations into the nonlinear oscillations of charged liquid drops were started about two decades ago, and the relevant literature now includes several dozen papers. However, all of these investigations were performed within the framework of the ideal liquid approximation [1–4]. This circumstance is obviously related to the fact that calculations of the nonlinear oscillations of a viscous liquid drop involve very cumbersome expressions. Nevertheless, it will be demonstrated below that this system is quite accessible for analytical description by means of a simple asymptotic method based on a direct expansion with respect to the initial perturbation amplitude, at least in the quadratic approximation (i.e., in the second order of smallness). The final results have the simplest form in the case of high viscosity (see [4]), whereby the liquid motions related to various deformation modes become aperiodic. An analytical expression obtained for the generatrix of the surface of the viscous liquid drop under such conditions is applicable to cases of both small (subcritical) and supercritical charges from the standpoint of the drop stability with respect to the intrinsic charge.

Formulation of the problem. We consider a drop of a perfectly conducting incompressible liquid with radius r_0, density ρ, kinematic viscosity ν, surface tension σ, and the total electric charge Q. Let us introduce a spherical coordinate system (r, ϑ, t) and denote the field of velocities in the drop as $\mathbf{U}(r, \vartheta, t)$, the field pressures as $p(r, \vartheta, t)$, and the electric field potentials near the drop and on its surface as $\phi(r, \vartheta, t)$ and $\phi_S(t)$, respectively. Then, an equation describing the surface shape of the drop performing axisymmetric oscillations about an equilibrium sphere of radius R at an arbitrary time can be written as

$$F(r, \vartheta, t) \equiv r - r_0 - \xi(\vartheta, t) = 0.$$

At the initial moment of time, $t = 0$, the equilibrium spherical shape of the drop is subject to an initial deformation representing a superposition of several virtually excited modes:

$$\xi = \varepsilon \sum_{m \in \Omega} h_m P_m(\mu), \quad \mu \equiv \cos(\vartheta),$$

$$\sum_{m \in \Omega} h_m = 1,$$

where ε is a parameter characterizing the amplitude of the initial perturbation of the drop surface; $P_m(\mu)$ is the Legendre polynomial of the mth order; and Ω is the set of indices of the numbers of initially excited surface modes.

The mathematical formulation of the problem of description of nonlinear axisymmetric capillary oscillations of a charged drop of a viscous incompressible conducting liquid has the following form:

$$\partial_t \mathbf{U} + (\mathbf{U} \cdot \nabla)\mathbf{U} = -\frac{1}{\rho}\operatorname{grad} p + \nu \Delta \mathbf{U};$$

$$\operatorname{div}\mathbf{U} = 0; \quad \Delta \phi = 0,$$

$$t = 0: \mathbf{U} = 0; \quad r \longrightarrow 0: \mathbf{U} < \infty;$$

$$r \longrightarrow +\infty: \nabla \phi \longrightarrow 0;$$

$$r = r_0 + \xi(\vartheta, t): \phi = \phi_S(t); \quad \partial_t F + (\mathbf{U} \cdot \nabla)F = 0;$$

$$\boldsymbol{\tau} \cdot (\mathbf{n} \cdot \nabla)\mathbf{U} + \mathbf{n} \cdot (\boldsymbol{\tau} \cdot \nabla)\mathbf{U} = 0;$$

$$-p + 2\rho\nu\mathbf{n} \cdot (\mathbf{n} \cdot \nabla)\mathbf{U} - p_Q + p_\sigma = 0;$$

$$\int_S \mathbf{n} \cdot \nabla \phi \, dS = -4\pi Q;$$

$$S = \{r, \vartheta, \varphi \,|\, r = r_0 + \xi; \; 0 \le \vartheta \le \pi; \; 0 \le \varphi \le 2\pi\};$$

$$\int_V r^2 \sin\vartheta \, dr d\vartheta d\varphi = \frac{4\pi}{3} r_0^3;$$

$$V = \{r, \vartheta, \varphi \,|\, 0 \le r \le r_0 + \xi; \; 0 \le \vartheta \le \pi; \; 0 \le \varphi \le 2\pi\};$$

$$\int_V \mathbf{r} \, r^2 \sin\vartheta \, dr d\vartheta d\varphi = 0.$$

Here, ∂_t denotes the partial derivative with respect to the variable t; $\boldsymbol{\tau}$ and $\mathbf{n}$ are the unit vectors of the tangent and normal to the free surface of the drop, respectively; and p_σ and p_Q are the pressures of the surface tension and the electric field of the intrinsic charge.

Solution of the problem. A solution to the above problem in the quadratic approximation with respect to a small parameter ε can be obtained using the conventional method of direct expansion in terms of the Laplace time transform. The final analytical expression for a generatrix of the free surface of a drop of highly viscous ($\nu\rho^{1/2}/(r_0\sigma)^{1/2} \ge 1$ [5]) incompressible conducting liquid performing oscillations of finite amplitude is as follows:

$$r(\vartheta, t) = r_0 + \varepsilon \sum_{n \in \Omega} h_n \exp\left(-\tau_n \beta_n \frac{r_0^2 \omega_n^2}{2\nu} t\right) P_n(\mu)$$

$$-\frac{\varepsilon^2}{r_0} \sum_{m \in \Omega} \frac{h_m}{2m+1} \exp\left(-\tau_m \beta_m \frac{r_0^2 \omega_m^2}{\nu} t\right) P_0(\mu) - \frac{9\varepsilon^2}{r_0}$$

$$\times \sum_{m \in \Omega} \frac{(m+1)h_m h_{m+1}}{(2m+1)(2m+3)} \exp\left(-\tau_m \beta_m \frac{r_0^2 \omega_m^2}{2\nu} t\right) \quad (1)$$

$$-\tau_{m+1}\beta_{m+1} \frac{r_0^2 \omega_{m+1}^2}{2\nu} t\bigg) P_1(\mu) + \varepsilon^2 \sum_{n=2}^{+\infty} \xi_n^{(2)}(t) P_n(\mu);$$

$$\xi_n^{(2)}(t) = \sum_{k, m \in \Omega} \left\{ \left\{ \exp\left(-(\tau_k \beta_k \omega_k^2 + \tau_m \beta_m \omega_m^2) \frac{r_0^2}{2\nu} t\right) \right. \right.$$

$$-\exp\left(-\tau_n \beta_n \omega_n^2 \frac{r_0^2}{2\nu} t\right) \bigg\} \frac{2n+1}{(n-1)(2n(n+2)+3)}$$

$$\times \frac{h_k h_m}{\tau_n \beta_n \omega_n^2 - \tau_k \beta_k \omega_k^2 - \tau_m \beta_m \omega_m^2}$$

$$\times \left\{ \frac{n\sigma}{\rho r_0^4} K_{kmn} \left(2(k(k+1)-1) + \left(3 + k(m+1) \right. \right. \right.$$

$$\left. - m(7+2m-2n))\frac{W}{2} \right) + \frac{W}{2}\frac{n\sigma}{\rho r_0^4}\alpha_{kmn}$$

$$-\left(K_{kmn} + \frac{\alpha_{kmn}}{km}\right)\frac{n\omega_k^2}{2r_0}$$

$$\times \frac{(2k+1)(m-1)(m+1)(2m+3)}{(k-1)(2k(k+2)+3)(2m+1)}$$

$$-\frac{1}{2kmr_0}(km(6(2k+1)(m+1)$$

$$+ (20m - k(k(2k+3)(2m+1) - 2(16m+5)) + 7)n$$

$$+ 2(7m + k(6(m+3) - k(2k+3)(2m+1)) + 11)n^2$$

$$- 4(2k+1)(m-1)n^3)K_{kmn} + (3(2m+1)n(2n+1)$$

$$- 2k^3(2m+1)n(2n+1)$$

$$+ 2k(2n(m+2+2(m-1)n-3n^2)+9)$$

$$- 3k^2(n(2n(2m+4n+5)+2m-3)-12)\alpha_{kmn}$$

$$+ 6k(2k+1)n(n+1)(m(m(2m-1)-4)\Gamma_{kmn}$$

$$+ 3\Lambda_{kmn})\omega_m^2/((2k+1)$$

$$\times (m-1)(2m(m+2)+3)(2n+1) \bigg\} \bigg\};$$

$$\omega_n^2 = \frac{\sigma}{\rho r_0^3} n(n-1)(n+2-W); \quad W = \frac{Q^2}{4\pi\sigma r_0^3};$$

$$\tau_n = \frac{(2n+1)(2n+5)(n-1)(2n^2+4n+3)}{3(4n^3+8n^2+6n+3)};$$

$$\beta_n = \frac{3(4n^3+8n^2+6n+3)}{(2n+5)(n-1)^2(2n^2+4n+3)^2};$$

$$\alpha_{kmn} = -C_{k0m0}^{n0} C_{k(-1)m1}^{n0} \sqrt{k(k+1)m(m+1)};$$

$$K_{kmn} = (C_{k0m0}^{n0})^2;$$

$$\Gamma_{kmn} = \frac{(2n+1)}{n(n+1)(2k+1)}\alpha_{nmk};$$

$$\Lambda_{kmn} = \frac{2n+1}{n(n+1)}\left(-\frac{m^2}{2m+1}\alpha_{nkm} + \sum_{j=1}^{[m/2]}\alpha_{n,k,m-2j}\right).$$

Here, C_{k0m0}^{n0} and $C_{k(-1)m1}^{n0}$ are the Clebsch–Gordan coefficients, and square brackets in the upper limit of the sum in expression for the coefficient Λ_{kmn} denote the integer part.

Analysis of the solution. Solution (1) determines the law of the temporal evolution of the shape of a liquid drop perturbed at the initial moment. When the Rayleigh parameter characterizing the stability of the drop with respect to the intrinsic charge is $W < 4$, the fundamental mode and, hence, the whole drop are stable. Figure 1 shows the time variation of a nonlinear correction to the fundamental mode for various values of the Rayleigh parameter.

In the case of $4 < W < 5$, the fundamental mode ($n = 2$) becomes unstable, while the higher modes remain stable, and the temporal evolution of the surface shale becomes more complicated (Fig. 2). The exponents containing the square of the fundamental mode frequency (ω_2^2) change their sign upon passage through $W = 4$. As a result, the corresponding term exponentially grows with the current time, whereas the other components in expression (1) keep decreasing with the time. Thus, in some period of time, the initial deformation ceases and the drop shape (determined by the fundamental mode) evolves into a figure resembling an elongated spheroid. For the conducting liquid drop, the degree of elongation due to an increase in the fundamental mode amplitude is limited either (i) by the onset of field emission at a sufficiently high intrinsic field strength (growing with the surface curvature at the apices) [5] or (ii) by partition of the drop into two smaller drops of comparable size [5, 6]. It should be noted that the instability of the fundamental mode is realized independently of whether this mode entered into the spectrum of modes determining the initial perturbation. Indeed, the fundamental mode is always excited in the second order of smallness due to the nonlinear interaction of modes, irrespective of the shape of the initial deformation [3, 7, 8].

For the Rayleigh parameter within $5 < W < 6$, the third mode ($n = 3$) also becomes unstable. Whether or not this additional instability leads to violation of the spheroid shape depends on whether the third mode was present in the spectrum of the initial perturbation or in the spectrum of modes excited due to the nonlinear
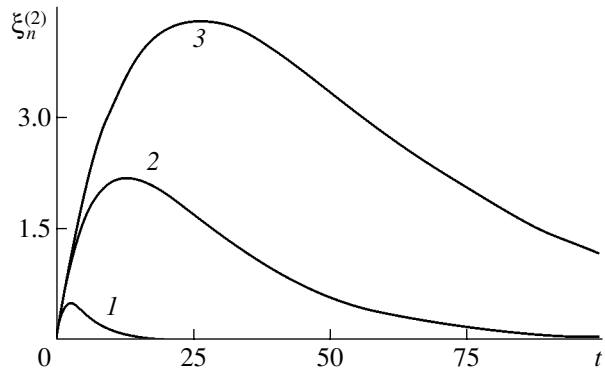
Fig. 1. Plots of the dimensionless parameter $\xi_2^{(2)}(t)$ of the fundamental mode versus dimensionless time, constructed using solution (1) in terms of the dimensionless variables ($\rho = \sigma = r_0 = 1$) for a single-mode initial perturbation with $k = m = 2$, $h_2 = 1$, $\nu = 1$, $n = 2$ and various values of the Rayleigh parameter $W = 3$ (1), 3.8 (2), and 3.9 (3) (the critical value of this parameter for realization of the instability of the fundamental mode is $W = 4$).
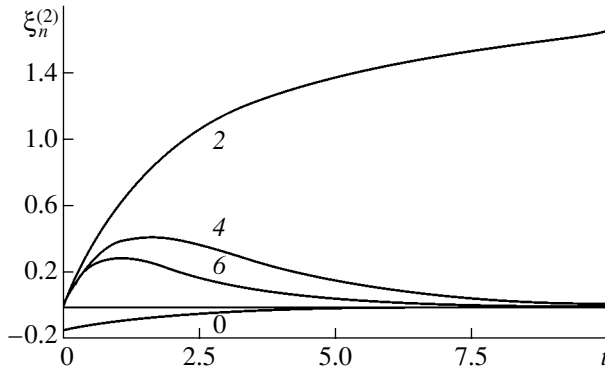
Fig. 2. Plots of the dimensionless parameter $\xi_n^{(2)}(t)$ versus dimensionless time, constructed for various mode numbers n (indicated at the curves) using solution (1) for a single-mode initial perturbation with $k = m = 3$, $h_3 = 1$, $\nu = 1$, $W = 4.1$ (supercritical value of the Rayleigh parameter for the fundamental mode).

interaction. If this mode is absent from both initial and excited sets, then—according to solution (1)—it will not influence the drop shape (apart from an oscillating thermal correction with negligibly small amplitude).

Conclusions. Nonlinear oscillations of viscous liquid drops can be analytically studied using classical asymptotic techniques. In the high viscosity limit, the final analytical expressions have a sufficiently compact form. An analysis of the obtained expression describing the temporal evolution of the shape of a deformed drop of such a strongly viscous liquid allows the time evolution of each excited mode to be traced.

REFERENCES

1. J. A. Tsamopolous and R. A. Brown, J. Fluid Mech. **147**, 373 (1984).

2. Z. C. Feng, J. Fluid Mech. **333**, 1 (1997).

3. A. N. Zharov, S. O. Shiryaeva, and A. I. Grigor'ev, Zh. Tekh. Fiz. **73** (12), 9 (2003) [Tech. Phys. **48**, 1511 (2003)].

4. A. N. Zharov and A. I. Grigor'ev, Zh. Tekh. Fiz. **75** (1), 22 (2005) [Tech. Phys. **50**, 19 (2005)].

5. A. I. Grigor'ev, Zh. Tekh. Fiz. **71** (10), 1 (2001) [Tech. Phys. **46**, 1457 (2001)].

6. D. F. Belonozhko, S. O. Shiryaeva, and A. I. Grigor'ev, Pis'ma Zh. Tekh. Fiz. **26** (19), 16 (2000) [Tech. Phys. Lett. **26**, 857 (2000)].

7. S. O. Shiryaeva, Zh. Tekh. Fiz. **71** (2), 27 (2001) [Tech. Phys. **46**, 158 (2001)].

8. V. A. Koromyslov, A. I. Grigor'ev, and Shiryaeva, Zh. Tekh. Fiz. **74** (9), 23 (2004) [Tech. Phys. **49**, 1126 (2004)].

Translated by P. Pozdeev

Effect of the Sublimation Coefficient
on the Photophoresis of Aerosol Particles
with Inhomogeneous Thermal Conductivity

Yu. I. Yalamov and A. S. Khasanov

Moscow State Regional University, Moscow, Russia
e-mail: rectorat@mgou.ru
Received February 8, 2005

Abstract—An analytical expression for the velocity of photophoresis of a large spherical solid aerosol particle is obtained, which takes into account evaporation (sublimation) of the particle material and its inhomogeneity with respect to thermal conductivity. © *2005 Pleiades Publishing, Inc.*

Consider a large spherical solid aerosol particle suspended in a single-component gas and let a homogeneous flux of electromagnetic radiation be incident onto the particle. The energy of radiation absorbed by the particle leads to the appearance of internal heat sources. In the general case, the particle is inhomogeneous with respect to heat conduction: the thermal conductivity coefficient at each point is a function of the radius vector. The surface of the particle features a phase transition, whereby the particle material evaporates (sublimes) with the formation of a viscous binary mixture surrounding the solid core. The interaction of this binary mixture with the inhomogeneously heated surface of the particle leads to thermal slide of the mixture over the surface, while the concentration inhomogeneity creates a diffusion slide component. In a coordinate system with the origin at the particle center, the problem of photophoresis reduces to the description of streamlining a sphere by the flow of a viscous binary mixture, with a certain constant (in both magnitude and direction) velocity $\mathbf{v}_\infty$ at the infinity. Let the positive direction of the Oz axis to coincide with the direction of propagation of the incident homogeneous radiation flux. Denoting by $\mathbf{U}_s$ the particle center-of-mass velocity relative to the external medium, we have $\mathbf{v}_\infty = -\mathbf{U}_s = U\mathbf{k}$, where U is the value to be found.

Now, let us formulate the equations and boundary conditions for the problem under consideration. Stationary motion of the binary mixture is described by the equations $\eta\nabla^2\mathbf{v} = \nabla p$, $\mathrm{div}\,\mathbf{v} = 0$ [1] and obeys the conditions $v_r = U\cos\theta$, $v_\theta = -U\sin\theta$, $p = p_\infty$ as $r \longrightarrow \infty$, where η is the dynamic viscosity coefficient of the binary mixture, $\mathbf{v}$ is the velocity field, p is the pressure field, and p_∞ is a certain constant. Let n_1, n_2 be the number densities of the first (evaporated particle material) and second (single-component gas) components of the

binary mixture, respectively, $n = n_1 + n_2$, and let c_1, c_2, be the relative concentrations of the corresponding components. Since $c_1 + c_2 = 1$, it is sufficient to find c_1 obeying the conditions $\nabla^2 c_1 = 0$, $c_1 = c_\infty = \mathrm{const}$ for $r \longrightarrow \infty$ [1].

In the boundary conditions, the quantities n_1, n_2, n, ρ (the density of the binary mixture), T_e (the temperature of the mixture), and T_i (the temperature inside the particle) will be replaced by their average values n_{01}, n_{02}, n_0, ρ_0, T_{0e}, and T_{0i} [1]. The surface of the particle is assumed to be impermeable for the second (gas) component of the binary mixture [1]: $n_{02}v_r - D\beta_1(c_2)'_r = 0$) for $r = a$, where $\beta_1 = n_0^2 m_1/\rho_0$, a is the particle radius, m_1 is the mass of evaporated molecules, and D is the coefficient of mutual diffusion in the binary mixture. The velocity component v_θ at $r = a$ obeys the condition $v_\theta = [K_{Tsl}^{(e)}/(aT_{0e})](T_e)'_\theta + (K_{sl}D/a)(c_1)'_\theta$ [1], where $K_{Tsl}^{(e)}$ and K_{sl} are the thermal and diffusion slide coefficients for the binary mixture.

Let $q_i(r, \theta)$ be the density of heat sources inside the particle and $\kappa_i(r)$ be the thermal conductivity coefficient in the particle. Then, the heat balance is described by the equations $\nabla^2 T_i = -(\kappa_i'/\kappa_i)(T_i)'_r - q_i/\kappa_i$, $\nabla^2 T_e = 0$ [2] with the boundary conditions $T_e = T_{0e}$ at $r \longrightarrow \infty$ and $T_e = T_i$ for $r = a$. The phase transition on the particle surface is described by the following equations [3]: $n_{01}v_r - D\beta_2(c_1)'_r = n_0\alpha v(s_1 - c_1)$, $-\kappa_e(T_e)'_r + \kappa_i(T_i)'_r = -Lm_1n_0\alpha v(s_1 - c_1)$ for $r = a$, where $\beta_2 = n_0^2 m_2/\rho_0$, m_2 is the mass of molecules of the second (gas) component of the binary mixture, $\alpha \in [0, 1]$ is the evaporation (sublimation) coefficient, $v = \sqrt{kT_{0e}/(2\pi m_1)}$ is one-fourth of the absolute thermal velocity of the evaporated mol-

ecules, s_1 is relative saturation concentration, L is the specific heat of the phase transition for the first component, and k is the Boltzmann constant. The relative saturation concentration s_1 of the first component at $r = a$ is described by the linearized formula [1] $s_1(T_i) = s +$ $\delta(T_i - T_{0i})$, where s and δ are the values of s_1 and $(s_1)'_{T_i}$ on the particle surface at $T_i = T_{0i}$.

Upon solving the problem with the boundary conditions formulated above, we obtain

$$\mathbf{U}_s = \frac{2}{3T_{0e}} \frac{2K_{Tsl}^{(e)}Dn_0 + \alpha va[(K_{Tsl}^{(e)} + K_{sl}D\delta T_{0e})n_{02} + \delta T_{0e}D\beta_1]}{2(2\kappa_e + \gamma\kappa_i)Dn_0 + \alpha va[(2\kappa_e + \gamma\kappa_i)n_{02} + 2\delta Lm_1 Dn_0^2]}$$
$$\times \left(\frac{1}{V}\int_V (Q_i \mathbf{r}, \mathbf{k})dV\right)\mathbf{k}, \tag{1}$$

where

$$Q_i = q_i(r, \theta)\frac{M(r)/r}{M(a)/a}, \quad \gamma = \frac{M'(a)a}{M(a)}, \tag{2}$$

V is the particle volume, $(\mathbf{a}, \mathbf{b})$ denotes the scalar product, and $M(r) = r\sum_{s=0}^{\infty}\alpha_s r^s$. The coefficients α_s are determined from the following recurrent formulas: if $b_0 = 2$, $b_1 = \kappa_{i,1}/\kappa_{i,0}$ and $b_s = (s\kappa_{i,s} - \sum_{j=1}^{s-1}\kappa_{i,j}\beta_{s-j})/\kappa_{i,0}$ for $s \geq 2$ (where $\kappa_i(r) = \sum_{s=0}^{\infty}\kappa_{i,s}r^s$), then $\alpha_0 = 1$ and $\alpha_s = -\sum_{j=1}^{s}(s+1-j)\alpha_{s-j}b_j/(s^2+3s)$ for $s \geq 1$.

The case of a homogeneous particle corresponds to $M(r) \equiv r$ and $\gamma = 1$. For $\kappa_i(r) = \kappa_i(0)\exp(kr)$, we have

$$M(r) = -\frac{6}{k^3 r^2}\left(\exp(-kr) - 1 + kr - \frac{k^2 r^2}{2}\right), \tag{3}$$

$$\gamma = \frac{M(a)a}{M(a)} = -2 - ka\frac{\exp(-ka) - 1 + ka}{\exp(-ka) - 1 + ka - 0.5k^2 a^2}. \tag{4}$$

If a phase transition does not take place on the particle surface, then $\alpha = 0$, $K_{Tsl}^{(e)} = K_{Tsl}\eta/\rho$ [1], and formula (1) yields an expression for the velocity $\mathbf{U}$ of an inhomogeneous nonvolatile particle. In the presence of a phase transition, the evaporated material concentrations are small and, hence, we may take $K_{Tsl}^{(e)} = K_{Tsl}\eta/\rho$, $n_{02} = n_0$, and $\rho_0 = \rho$, which yields

$$\mathbf{U}_s = \mathbf{U}\frac{1 + 0.5\alpha[1 + \rho K_{sl}D\delta T_{0e}/(K_{Tsl}\eta) + D\delta T_{0e}n_0 m_1/(K_{Tsl}\eta)]/D}{1 + 0.5\alpha[1 + 2D\delta Lm_1 n_0/(2\kappa_e + \gamma\kappa_i)]va/D}.$$

For the surface of an ice particle, which exhibits melting and evaporation into air [4], we obtain [4]

$$U_s = U\frac{1 + 45.41\alpha}{1 + 37.77\alpha(0.75 + 0.25/\gamma)}. \tag{5}$$

Let us consider this formula for $\kappa_i(r) = \kappa_i(0)\exp(kr)$, with a change over the particle radius a obeying the condition $0.1 \leq \kappa_i(a)/\kappa_i(0) \leq 10$. Then, formula (4) yields $\gamma \in [0.59; 1.81]$. When α varies in the interval $[0, 1]$, the correction coefficient in formula (5) changes within 0–1.024 for $\gamma = 0.59$, 1–1.197 for $\gamma = 1$, and 1–1.343 for $\gamma = 1.81$. Thus, allowance for the possible variation of the evaporation (sublimation) coefficient α can provide for a significant (up to 20%) contribution to the photophoresis velocity of a homogeneous particle ($\gamma = 1$), while inhomogeneous heat conduction may either increase (for $\gamma > 1$) or decrease (for $\gamma < 1$) this contribution.

REFERENCES

1. Yu. I. Yalamov and V. S. Galoyan, *Dynamics of Drops in Inhomogeneous Viscous Media* (Luis, Yerevan, 1985) [in Russian].

2. E. R. Shchukin, Yu. I. Yalamov, and Z. L. Shulimanova, *Selected Problems of the Physics of Aerosols* (Mosk. Pedagog. Univ., Moscow, 1992) [in Russian].

3. Yu. I. Yalamov and A. S. Khasanov, Zh. Tekh. Fiz. **74** (7), 13 (2004) [Tech. Phys. **49**, 818 (2004)].

4. B. Vargaftik, Y. K. Vinogradov, and V. S. Yargin, *Handbook of Physical Properties of Liquids and Gases: Pure Substances and Mixtures* (Nauka, Moscow, 1972; Begell House, New York, 1996).

Translated by P. Pozdeev

Hydrogen Production from Methane in Electron-Beam-Generated Plasma

R. G. Sharafutdinov[a], A. E. Zarvin[b],*, V. Zh. Madirbaev[b], V. V. Gagachev[a], and G. G. Gartvich[b]

[a] *Institute of Thermophysics, Siberian Division, Russian Academy of Sciences, Novosibirsk, Russia*
[b] *Novosibirsk State University, Novosibirsk, Russia*
* e-mail: zarvin@phys.nsu.ru
Received March 29, 2005

Abstract—Processes in a rarefied flow of methane activated by a high-energy electron beam have been studied as dependent on the gas pressure and the electron energy and total current. The electron beam initiates reactions leading to the conversion of methane into molecular hydrogen. The conversion coefficient has been determined as a function of the process parameters. By selecting proper parameters, it is possible to provide for a high rate of the conversion reaction. © *2005 Pleiades Publishing, Inc.*

Analysis of the modern trends in natural gas processing technologies shows that new methods are now being extensively invented to supplement the traditional chemistry and catalysis, which have provided for the creation and development of the chemical industry in the 20th century. According to these new technologies, the reactions proceed in the gas phase rather than on the catalyst surface, and the reaction rates are determined by excited and ionized particles rather than by neutrals (the reaction cross sections of the former species being several orders of magnitude higher than those of the latter).

We distinguish three main stages in the initiation and conduction of plasmachemical reactions. In the first state, energy is transferred from an external source to the electron component of plasma. In the second stage, the energy is transferred from the excited electron gas to heavy particles in the course of heating, excitation of the internal degrees of freedom of atoms and molecules, and their ionization and dissociation. As a result, the energy supplied from the external source is redistributed between molecules of the reactants, which leads to the formation of chemically active particles. As a rule, the fraction of energy spent for the direct gas heating is relatively small: the energy is spent primarily for exciting the internal degrees of freedom in atoms and molecules. The third stage involves chemical transformations in this reactive medium. Thus, plasmachemical processes involve all the species existing in the plasma, including electrons, ions, and neutrals in the ground and excited states, but the determining role in the initiation of reactions is played by the electron component.

In recent years, the plasmachemical conversion of methane into hydrogen has been extensively studied in many countries [1–7]. Unfortunately, significant drawbacks hindering the creation of commercial technologies based on thermal plasma and various types of discharge have not yet been eliminated. The main difficulties are related to a short working life of the equipment, high consumption of energy, significant influence of electrodes on the course of processes in the plasma flow, and high rate of reverse reactions [8–10]. These problems stimulate the search for new—more convenient, controllable, and efficient—methods of the initiation of plasmachemical reactions.

This Letter presents the results of our investigations into plasmachemical reactions initiated by electron beams with energies on the order of several kiloelectronvolts generated by hollow-cathode electron guns.

The experiments were performed on a VS-4 setup created at the Institute of Thermophysics (Novosibirsk) [11], which was additionally equipped with a rough pumping stage and an electron gun generating an electron beam directed along the gas flow axis. A schematic diagram of the system is presented in the inset to Fig. 1. Methane was supplied via inlet pipe *1* to the output of the roughing stage, with a circular nozzle *5* creating a supersonic stream along the axis of an electron beam produced by a hollow-cathode electron gun *6*. The electron-beam-generated plasma jet entered an axial quartz tube reactor *2* with a geometry selected so as to provide for a low pressure at the input and to ensure the jet stopping at the output. The samples of gaseous reaction products for the composition analysis were taken from the flow axis via a skimmer of the molecular beam system *3* arranged immediately at the reactor output. The supersonic molecular beam was detected and analyzed by a monopole mass spectrometer *4* (MX-7305) entering into a computer-controlled system of data acquisition and processing.
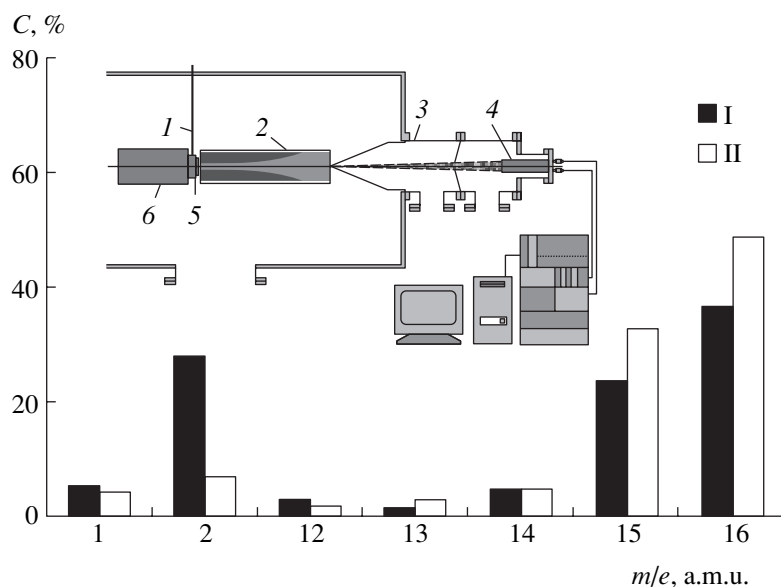
Fig. 1. Mass spectra of (I) methane and (II) the products of methane conversion in electron-beam-generated plasma. The inset shows a schematic diagram of the experimental setup: (*1*) working gas supply; (*2*) reactor; (*3*) molecular beam generator; (*4*) mass spectrometer; (*5*) circular supersonic nozzle; (*6*) electron gun.

The initiation of chemical reactions by means of the combination of a supersonic jet and a high-energy electron beam has two important advantages: (i) the electron energy distribution in the reactor is significantly shifted toward higher energies as compared to that in the case of a discharge plasma and (ii) a sharp drop in the plasma density along the jet ensures "closing" of the reverse reactions, thus preventing a decrease in the target product yield from the plasmachemical reaction.

Figure 1 shows the typical results of mass-spectrometric measurements in the flow of pure methane processed in the system described above. The histogram compares the intensities C (percentage) of ion peaks measured in the activated (I, electron gun on) and neutral (II, electron gun off) flows. As can be seen, the electron beam action leads to a decrease in intensities of the peaks of methane ($m/e = 16$, $[CH_4]^+$) and its dissociative ionization products ($m/e = 15$ $[CH_3]^+$, 14 $[CH_2]^+$, 13 $[CH]^+$, and 12 C^+), with a simultaneous increase in the peak of molecular hydrogen ion ($m/e = 1$ $[H_2]^+$).

The coefficient of methane conversion into hydrogen achieved for the optimum ratio between the densities of the gas flow and the electron beam current in the activation region was $K_{conv} = 0.9$–0.95, at a coefficient of methane use up to $K_{use} = 0.5$. Thus, the combination of a supersonic jet and a high-energy electron beam provides, at a comparable degree of conversion, a record high reaction rate, even in comparison to processes initiated by electric discharges of other types. Figure 2 presents comparative data on the time t of gas occurrence in the reactor versus K_{conv} for various methods of conversion. The electron-beam activation of plasmachemical processes shifts the electron energy distribution in the reactor toward higher energies and,

hence, increases the product yield as compared to that reached with discharge plasmas. The ion-molecular processes in the electron-beam-generated plasma are not affected by electrodes, walls, and background gases. The high efficiency of the proposed process is
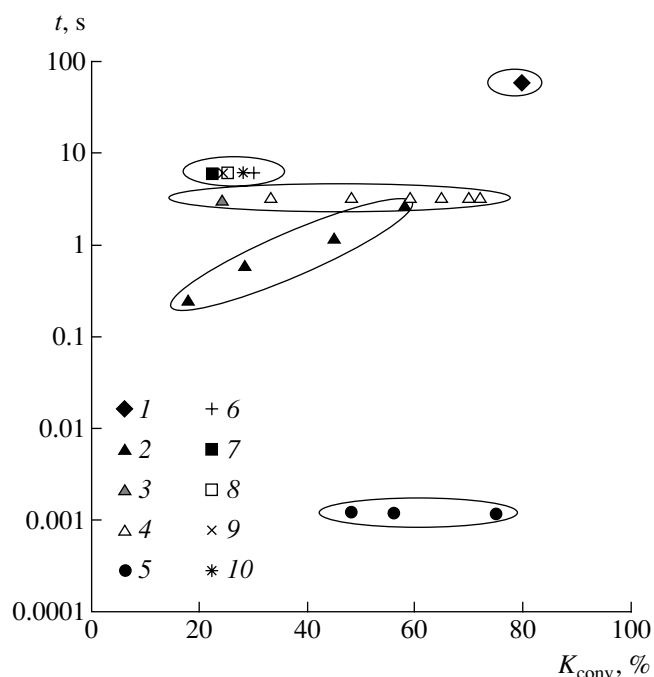
Fig. 2. A plot of the time t of gas occurrence in the reactor versus conversion coefficient K_{conv} for various methods of conversion: (*1*) steam conversion; (*2*) streamer discharge [12]; (*3*) barrier discharge [13]; (*4*) barrier discharge [14]; (*5*) this study; (*6–10*) SHS catalysts [15], including MgO (*6*), LaCaB$_6$–MgO (*7*), SmCaB$_6$–MgO (*8*), LaBaB$_6$–MgO (*9*), and LaCaB$_6$–MgO/Mn$_3$O$_4$–NaCl (*10*).

combined with a relatively low consumption of energy per unit weight of converted methane (below 1 kJ/g). It is possible to independently vary the gas jet and the electron beam parameters, thus controlling the conditions of discharge in the plasma flow, the course of chemical reactions, and the yield of a target product.

In conclusion, the proposed approach allows compact reactors to be developed for the processing of natural and oil-accompanying gases. By changing the conditions in the reaction zone, it is possible to modify the composition of by-products from pure carbon (deposited as soot) to heavy liquid hydrocarbons. Our technical solutions can be implemented in hydrogen generators for cars operating on fuel cells.

REFERENCES

1. L. Bromberg, D. R. Cohn, J. Heywood, *et al.*, in *Proceedings of the 8th Diesel Engine Emissions Reduction (DEER) Meeting, San Diego, 2002.*

2. K. Supat, S. Chavadej, L. L. Lobban, *et al.*, Energy Fuels **17**, 474 (2003).

3. J. R. Fincke, R. P. Anderson, T. Hyde, *et al.*, Plasma Chem. Plasma Process. **22**, 105 (2002).

4. J.-J. Zou, Y.-P. Zhang, C.-J. Liu, *et al.*, Plasma Chem. Plasma Process. **23**, 69 (2003).

5. Yun Yang, Plasma Chem. Plasma Process. **23**, 283 (2003).

6. S. L. Yao, E. Suzuki, N. Meng, *et al.*, Plasma Chem. Plasma Process. **22**, 225 (2002).

7. M. Deminsky, V. Jivotov, B. Potapkin, *et al.*, Pure Appl. Chem. **74**, 413 (2002).

8. E. Ruzinska, M. Kurdel, and M. Morvova, in *Proceedings of the 5th International Symposium on High Pressure Low Temperature Plasma Chemistry (HAKONE-5), Milovy, 1996,* pp. 290–294.

9. K. V. Kozlov, P. Michel, and H.-E. Wagner, in *Proceedings of the 6th International Symposium on High Pressure Low Temperature Plasma Chemistry (HAKONE-6), Cork, 1998,* pp. 78–82.

10. K. Thanyachotpaiboon, S. Chavadej, T. A. Caldwell, *et al.*, AIChE J. **44**, 2252 (1998).

11. A. E. Zarvin and R. G. Sharafutdinov, *Rarefied Gas Dynamics* (IT SO RAN, Novosibirsk, 1976), pp. 19–37 [in Russian].

12. C. L. Gordon, L. L. Lobban, and R. G. Mallinson, in *Advances in Hydrogen Energy*, Ed. by C. E. G. Padro and F. Lau (Kluwer Academic/Plenum, New York, 2000), pp. 57–67.

13. L. M. Zhou, B. Xue, U. Kogelschatz, *et al.*, Plasma Chem. Plasma Process. **18**, 375 (1998).

14. C.-J. Liu, B. Xue, B. Eliasson, *et al.*, Plasma Chem. Plasma Process. **21**, 301 (2001).

15. É. A. Grigoryan and A. G. Merzhanov, Nauka Proizvod., No. 3, 30 (1998).

Translated by P. Pozdeev

GaAs Nanowhisker Arrays
Grown by Magnetron Sputter Deposition

I. P. Soshnikov

Ioffe Physicotechnical Institute, Russian Academy of Sciences, St. Petersburg, Russia
St. Petersburg Physical Engineering Research and Education Complex, Russian Academy of Sciences,
St. Petersburg, Russia
Received March 16, 2005

Abstract—Arrays of cone-shaped GaAs nanowhiskers (NWs) with a surface number density of up to 10^9 cm^{-2}, a height ranging from 300 to 10000 nm, and a diameter of about 200 nm at the base and from 200 to 10 nm and below at the top have been obtained by means of magnetron sputtering. The characteristic NW height is proportional to the effective thickness of a deposited material layer and inversely proportional to the transverse whisker size at the top. An analysis of the NW parameters confirms the validity of the Dubrovskii–Sibirev diffusion mechanism of NW formation. © 2005 Pleiades Publishing, Inc.

The arrays of vertical nanowires or nanowhiskers (NWs) grown from semiconductor materials are promising anisotropic materials for various applications, in particular, for opto- and microelectronics [1, 2]. NWs can be used for the creation of field emission cathodes, quantum-wire diodes and transistors, microdevices for the adsorption chromatography of organic substances, etc. As a rule, NW arrays are obtained by means of molecular beam epitaxy (MBE) [2–6] or chemical vapor deposition (CVD) [1, 7–9]. Disadvantages of these technologies are the relatively high cost of production and/or insufficient ecological safety. These circumstances pose the currently important problem of developing alternative, ecologically safe, and economical methods of obtaining NW arrays.

This Letter presents the results of our investigation into the possibility of growing NW arrays by the method of magnetron sputter deposition.

The formation of whiskers can proceed according to the vapor–liquid–solid (VLS) mechanism [6–9], whereby the components are adsorbed on an intermediate element (a catalyst droplet), transferred via this droplet or over its surface by means of diffusion, and built into the NW growing at the interface. The VLS mechanism predicts an increase in the NW growth rate V with increasing transverse size (diameter) of the whiskers according to the law $V \sim (A - B/D)^2$, where A and B are constant parameters [8, 10, 11]. An alternative diffusion mechanism is characterized by a monotonic decrease in the NW growth rate with increasing whisker diameter: $V \sim D^{-1}$ [6, 10, 11]. The VLS mechanism is usually realized in a CVD process under conditions of suppressed growth on the base substrate surface [1, 7–9]. The growth via a diffusion mechanism or a combined diffusion/VLS process usually takes place under MBE conditions [3–6, 10, 11]. It should be noted

that, in the case of a diffusion mechanism, the base surface may also continuously grow and supply material to NWs [8, 11].

The magnetron sputtering of GaAs is accompanied by deposition of the sputtered particles with a high average energy (up to 10 eV) [12, 13], which must favor the diffusion of adsorbed atoms on the surface at a weak desorption in the range of temperatures below $T \sim 600°C$. Therefore, it was expected that the NW growth under such conditions would proceed predominantly by the diffusion mechanism.

The experiments with magnetron sputter deposition of GaAs and Si were performed in a vacuum system (VUP-2M) equipped with a dc magnetron and a resistive evaporator. The latter was used for depositing thin gold (NW growth activator) films (99.99% Au). The substrates were mounted on a special movable table, on which the samples could be heated up to $T \sim 800°C$ in a position away from the sputter deposition zone. The targets were made of commercial GaAs wafers (AGChK-3 grade). The residual gas pressure in the vacuum chamber was initially below 3×10^{-6} Torr and increased to $(2–5) \times 10^{-2}$ Torr due to the leak of argon (99.99% Ar) in the course of magnetron operation. In some experiments, Au films were deposited in a different vacuum setup (VUP-5) equipped with electron-beam heaters.

The substrates were (111)B- and (100)-oriented single crystal GaAs plates. In order to avoid the influence of surface oxides and contaminations, the substrates were preliminarily sequentially treated with organic solvents, a sulfuric acid–hydrogen peroxide–water mixture (H_2SO_4–H_2O_2–H_2O, 5 : 2 : 2), and an aqueous hydrochloric acid solution (HCl–H_2O, 1 : 10).

The NW growth was carried out according to the following scheme. After evacuation of the working chamber, the samples were heated to about 150°C and covered with a gold activator layer to a thickness of about 1 nm. Then, argon was admitted to the magnetron working pressure and the magnetron plasma discharge was initiated. Simultaneously, the samples were heated to $T \sim 625$°C and kept at this temperature for ~1 min away from the magnetron sputter deposition zone. Then, the temperature was reduced to 575°C and the table with samples was moved to the zone of deposition. The deposition time was controlled so as to provide for the formation of a layer with a desired effective thickness varying from 0.1 to 1 μm. Finally, the magnetron discharge and the sample heater were switched off and the samples were kept in a flow of argon until they cooled to a temperature below 50°C. The effective thickness of the deposited semiconductor layer was determined using a satellite substrate not covered with the Au activator layer.

The experiments with the deposition of Au and the semiconductor in different vacuum chambers were performed according to an analogous scheme involving an additional stage of sample transfer from one chamber to another. The results of experiments performed in the same chamber (without sample transfer) and with a transport of samples within 24 h exhibited no significant differences.

The sample surface was studied in a CamScan S4-90FE scanning electron microscope (SEM) with a field emission cathode. Figure 1 presents a SEM micrograph showing the typical morphology of a deposit formed on a GaAs($1\bar{1}1$)B surface. As can be seen, the substrate surface bears an array of NWs having the characteristic shape of truncated cones with a small apical angle (below 10°) and the axes oriented predominantly along the (111) direction. The NW surface number density was on the order of 10^9 cm^{-2}. The NWs range from 300 to 10 000 nm in height and have diameters of about 200 nm at the base, while the transverse size at the top varies from 200 to 10 nm and below. The NW height is proportional to the effective thickness of a deposited semiconductor layer (in the range studied) and may exceed this value by a factor of ten or more.

The morphology of a deposit grown on a GaAs(100) surface corresponds to NWs oriented predominantly in the ($1\bar{1}0$) plane along the (111)B direction. However, some of the NWs are oriented in the (110) plane and aligned in the normal direction. The dimensions of NWs grown on the GaAs(100) surface are generally smaller than those obtained in the (111)B substrate.

Figure 2 presents data on the dimensions of NWs grown on the GaAs(111)B surface. This plot of the NW height versus diameter at the top (which virtually coincides with the diameter of the catalyst droplet) corresponds to the inverse proportionality $h \sim D^{-1}$. This result is consistent with the above considerations concerning the most probable NW growth mechanism and agrees
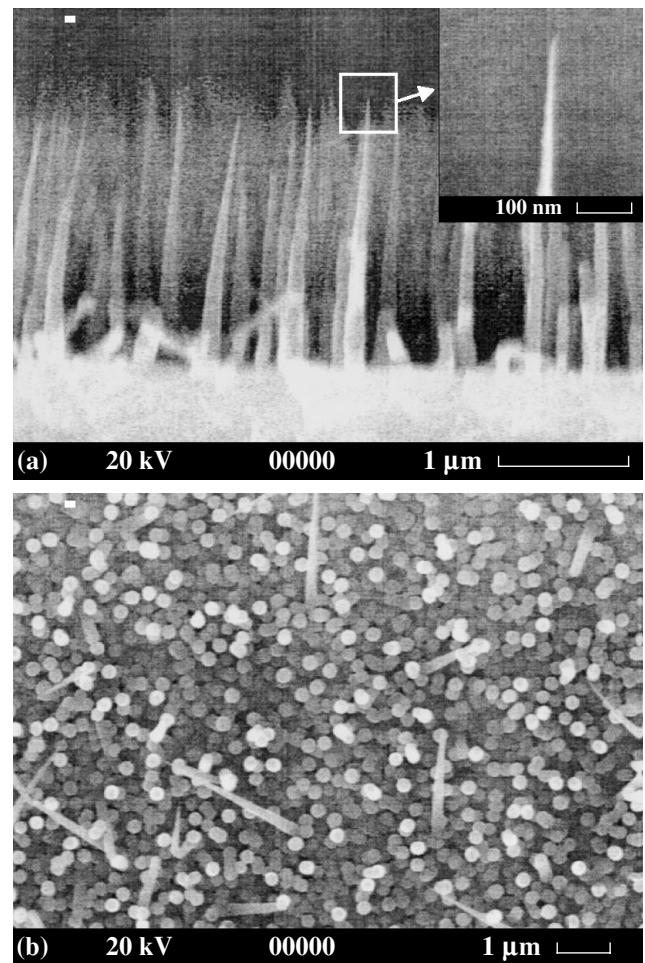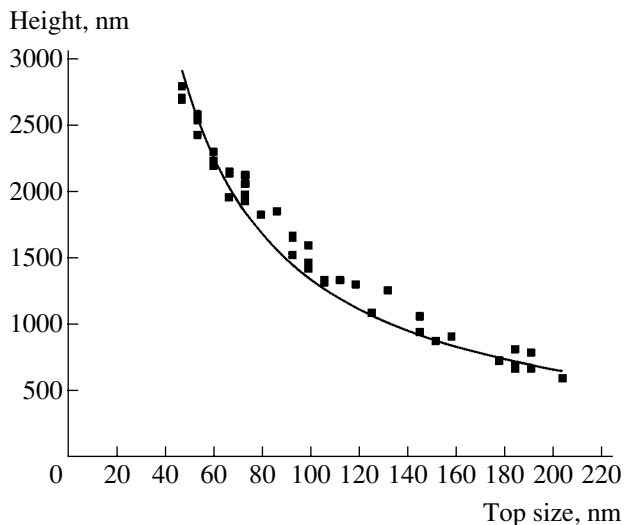

Fig. 1. Field-emission SEM images showing the typical surface morphology of samples after deposition of a 1-nm-thick Au activator layer and a GaAs layer with an effective thickness of 170 nm by magnetron sputtering onto a GaAs(111)B substrate at a temperature of 575°C: (a) transverse cross section; (b) top view. Probing electron beam energy, 20 keV.

well with the Dubrovskii–Sibirev model [6, 10, 11] stipulating the NW growth according to the diffusion mechanism.

Special experiments with GaAs deposition onto samples without chemical pretreatment and/or after prolonged exposure to the atmosphere showed that NW arrays are not formed on such substrates. This is probably related to a decrease in the rate of surface diffusion on oxidized surfaces

To summarize, it was demonstrated that the arrays of vertical GaAs NWs with a surface number density of up to 10^9 cm^{-2}, a height ranging from 300 to 10 000 nm, and a diameter of about 200 nm at the base and from 200 to 10 nm and below at the top can be obtained by means of magnetron sputter deposition. The characteristic NW height is proportional to the effective thickness of a deposited material layer and inversely proportional to the transverse whisker size at the top. An anal-

Height, nm

Fig. 2. A plot of the GaAs whisker height h versus diameter D at the top for the GaAs NWs obtained after deposition of a 1-nm-thick Au activator layer and a GaAs layer with an effective thickness of 170 nm by magnetron sputtering onto a GaAs(111)B substrate at a temperature of 575°C. Points present the experimental data; the solid curve shows the calculated $h = D^{-1}$ dependence.

ysis of the NW parameters shows evidence for the diffusion mechanism of NW formation.

REFERENCES

1. K. Hiruma, M. Yazawa, K. Haraguchi, *et al.*, Appl. Phys. **74**, 3162 (1993).
2. B. J. Ohlsson, M. T. Bjork, M. H. Magnusson, *et al.*, Appl. Phys. Lett. **79**, 3335 (2001).
3. A. A. Tonkikh, G. E. Cirlin, Yu. B. Samsonenko, *et al.*, Fiz. Tekh. Poluprovodn. (St. Petersburg) **38**, 1256 (2004) [Semiconductors **38**, 1217 (2004)].
4. I. P. Soshnikov, A. A. Tonkikh, G. E. Cirlin, *et al.*, Pis'ma Zh. Tekh. Fiz. **30** (19), 28 (2004) [Tech. Phys. Lett. **30**, 765 (2004)].
5. I. P. Soshnikov, G. E. Cirlin, A. A. Tonkikh, *et al.*, Fiz. Tverd. Tela (St. Petersburg) (2005) (in press).
6. V. G. Dubrovskii, G. E. Cirlin, I. P. Soshnikov, *et al.*, Phys. Rev. B (2005) (in press).
7. E. I. Givargizov, Kristallografiya **20**, 812 (1975) [Sov. Phys. Crystallogr. **20**, 498 (1975)].
8. S. M. Polyakov, E. N. Laverko, and V. M. Marakhonov, Kristallografiya **15**, 598 (1970) [Sov. Phys. Crystallogr. **15**, 519 (1970)].
9. R. S. Wagner and W. C. Ellis, Appl. Phys. Lett. **4**, 89 (1964).
10. V. G. Dubrovskii and N. V. Sibirev, Phys. Rev. E **70**, 031604 (2004).
11. G. E. Cirlin, V. G. Dubrovskii, N. V. Sibirev, *et al.*, Fiz. Tverd. Tela (St. Petersburg) **39**, 587 (2005) [Phys. Solid State **39**, 557 (2005)].
12. V. T. Barchenko, Yu. A. Bystrov, and E. A. Kolgin, *Ion–Plasma Technologies in Electronic Technologies* (Énergoatomizdat, St. Petersburg, 2001) [in Russian].
13. *Sputtering of Solids: Principles and Applications*, Ed. by E. S. Mashkova (Mir, Moscow, 1989) [in Russian].

Translated by P. Pozdeev

Rarefaction of the Spectrum of H-Type Whispering-Gallery Modes in a Hemispherical Dielectric Resonator

G. V. Golubnichaya, A. Ya. Kirichenko, and I. G. Maksimchuk

Usikov Institute of Radiophysics and Electronics, National Academy
of Sciences of Ukraine, Kharkov, Ukraine
e-mail: kharkovs@ire.kharkov.ua
Received January 19, 2005

Abstract—A dense spectrum of H-type resonance oscillations (whispering-gallery modes) is observed in a hemispherical dielectric resonator excited by a capacitive slit situated on the equatorial metal mirror surface. The spectrum can be significantly rarefied by exciting the WG modes in the resonator by means of distributed coupling to a dielectric waveguide arranged in a certain special position relative to the hemisphere base. © *2005 Pleiades Publishing, Inc.*

Introduction. Dielectric resonators featuring high-Q oscillations of the whispering-gallery (WG) type are attracting increasing attention from the standpoint of both basic science and microwave device applications (especially in the millimeter- and submillimeter-wave ranges). Such resonators are used for frequency stabilization of self-excited oscillators [1], for obtaining bandstop filters [2], for the measurement of dielectric properties of low-loss materials [3], etc. Most widely used are the disk-shaped and spherical dielectric resonators. The main advantage of disk-shaped resonators is the relatively simplicity of the calculations of their electrodynamic properties, resonance frequencies, and wave field distributions. However, since the WG modes excited in such resonators are doubly degenerate, even a slight inhomogeneity frequently leads to the splitting and overlap of the resonance bands. This gives rise to additional difficulties in determining the quality factors, which is especially important in the measurements of dielectric properties [4].
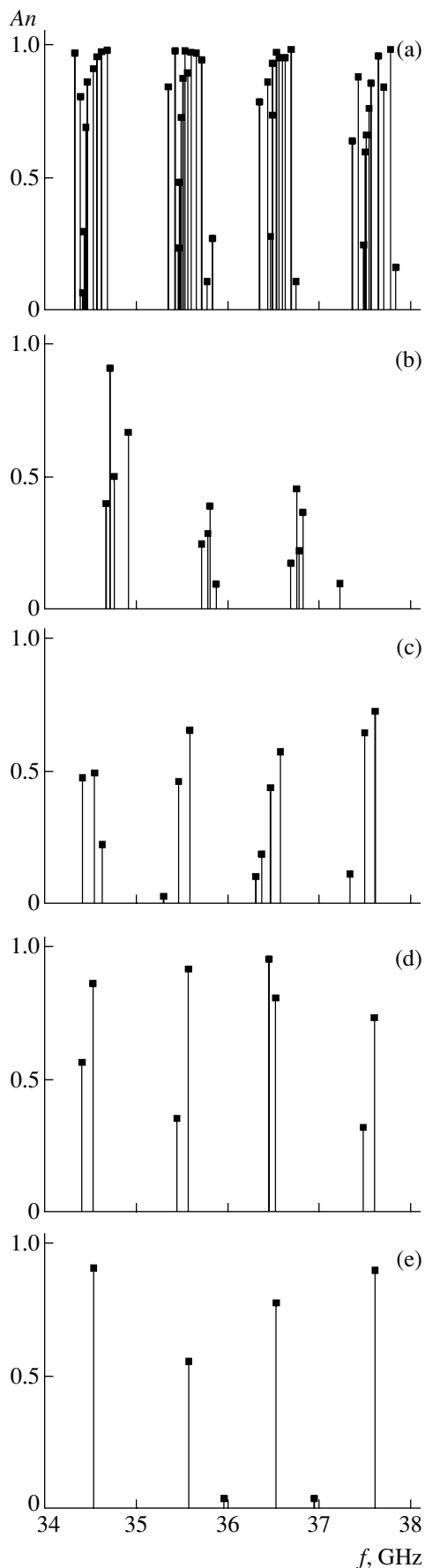
The quality factors for oscillations excited in a spherical dielectric resonator are higher than those for the modes excited in a disk-shaped resonator, which is explained by a decrease in the radiation losses from curvilinear surfaces in the former case. For a more convenient excitation of oscillations in such resonators and for expanding their functional possibilities, it was suggested to use dielectric resonators in the form of a hemisphere with a metal mirror in the equatorial plane [5]. When the E-type modes are excited in a hemispherical dielectric resonator by a capacitive slit situated on the mirror surface, resonance oscillations are observed whose fields on the curvilinear surface form "belts" in the polar direction with one or two field variations along the azimuthal coordinate. These belts are formed by the waves normally incident onto the

mirror surface and, hence, normally reflected from this surface. Thus, the presence of a metal mirror is a necessary prerequisite for the appearance of such oscillations. However, when the H-type WG modes are excited in this resonator by a capacitive slit on the mirror, the observed spectrum of resonance oscillations is extremely dense [6]. This circumstance not only hinders the practical implementation of hemispherical dielectric resonators with H-type WG modes: it even complicates the investigation of such oscillations.

The aim of this study was to assess the possibility of rarefying the spectrum of the H-type resonance oscillations in a hemispherical dielectric resonator by selecting a proper method of excitation.

Experimental methods. The H-type WG modes were studied using hemispherical dielectric resonators with and without an equatorial mirror. The hemisphere with a radius of 37 mm was made of Teflon. The copper mirror had a diameter much in excess of the hemisphere base. We used the following methods for the excitation of oscillations: (i) via a radial capacitive 7.2×1.7-mm slit in the mirror; (ii) via a 7×1.0-mm open end of a metal waveguide; and (iii) via a 7.2×3.4-mm dielectric (Teflon) waveguide with the narrow wall situated near the curvilinear surface of the hemisphere and oriented perpendicular to the base (it was also possible to move the exciting waveguide from the base toward the pole).

The signal from a klystron was passed via a ferrite gate and an attenuator and fed to the dielectric resonator. The reflected signal from the measurement arm of a directional coupler was fed to a crystal detector, amplified, and displayed by an oscilloscope. The resonance frequency was determined using a resonance wavemeter. The working frequency range was determined by the interval of mechanical tuning (32–38 GHz) of the

Fig. 1. Relative amplitude *A* versus frequency *f* of the H-type resonance WG modes in a hemispherical dielectric resonator (a, b) with and (c–e) without a metal mirror, excited via (a) a slit in the mirror, (b) a dielectric waveguide, (c) a metal waveguide with narrowed end; (d) a dielectric waveguide at $h = 0$; (e) a dielectric waveguide at $h = 6$ mm.

klystron frequency. Thus, we have measured the amplitude–frequency characteristics for the WG modes excited by different methods in a hemispherical dielectric resonator.

Experimental results. Figure 1a shows a plot of the relative amplitude of the resonance H-type WG modes versus frequency for the hemispherical dielectric resonator with a metal mirror in the equatorial plane. The WG modes were excited via a radial capacitive slit in the mirror plane. As can be seen, the spectrum is highly complicated, dense, and multicomponent, displaying repeated series of the resonance H-type WG modes spaced by ~1-GHz intervals. In each series, more than ten WG modes are excited over an interval of several tens of megahertz, the resonance peaks of which can overlap. This behavior explains why the H-type oscillations in a mirror dielectric hemisphere resonator have not been studied so far.

When the same hemisphere with the equatorial mirror is excited via a dielectric waveguide, the resulting spectrum of resonance frequencies is significantly rarefied (Fig. 1b), and only resonance frequencies are retained. Apparently, a decrease in the number of resonances is related to a change in the conditions of WG mode reflection from the metal mirror upon a change of the site of excitation. Note that the modes of lowest frequencies are absent from each series, for which the belts of the field distribution pass (like those for the E-type oscillations [6]) through the pole of the hemisphere. In addition, the entire spectrum is somewhat displaced (approximately by 0.25 GHz) toward higher frequencies.

During this investigation, it was established that the H-type WG modes (in contrast to the E-type modes) can be excited in the dielectric hemisphere even without the metal mirror. Figure 1c shows the spectrum of resonance frequencies excited via the open end of a metal waveguide with a narrow wall width reduced so as to obtain a 7.2×1.0-mm slit. The waveguide slit was situated in the base plane of the hemisphere and oriented in the radial direction. Here, each series of the excited WG modes comprises two main frequencies and several additional components of lower intensity, while some WG modes (effectively excited previously due to reflection from the metal mirror) are absent.

An even more rarefied spectrum of resonance frequencies is observed when the H-type WG modes are excited in the dielectric hemisphere without a mirror by means of a rectangular dielectric waveguide situated near the hemisphere base (Fig. 1d). Here, the spectrum contains only two degenerate resonance modes. Inves-
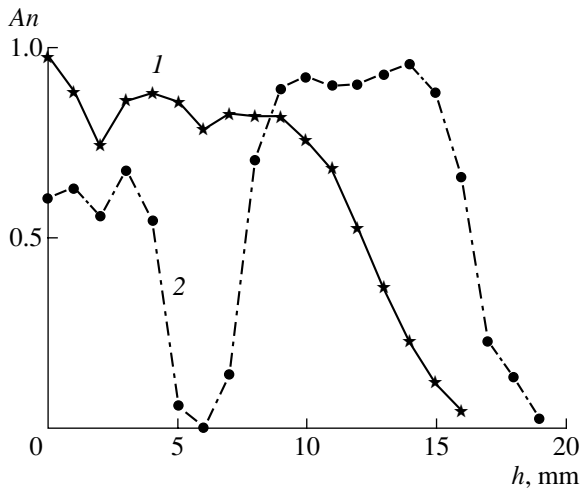
Fig. 2. Plots of the relative amplitude A of the H-type resonance WG mode with (*1*) $f = 37.55$ GHz and (*2*) $f = 37.45$ GHz in a hemispherical dielectric resonator without a metal mirror, as a function of the distance from the hemisphere base to the exciting dielectric waveguide displaced in the polar direction.

tigation of the H-type WG mode field distribution showed that these fields form two belts in the azimuthal direction (i.e., parallel to the equator), both adjoining the hemisphere base. Since the difference between the two resonance frequencies was approximately 0.10 GHz, it was established that the quality factor for the high-frequency component in the series ($f = 37.55$ GHz) exceeds 2000, whereas that for the low-frequency component ($f = 37.45$ GHz) only reaches 1250.

We have changed the excitation site by shifting the dielectric waveguide from the equator to the pole of the hemisphere (while retaining as much as possible the waveguide–resonator coupling coefficient) and measured the relative amplitude A of the resonance as a function of the distance h from the base plane. As can be seen from the data presented in Fig. 2, the efficiency of excitation of the two electromagnetic field components behaves differently in response to displacement of the exciting waveguide. Indeed, the efficiency of resonance excitation at 37.55 GHz remains almost constant up to $h \sim 10$ mm and, then, drops to zero as h is increased from 10 to 16 mm. At the same time, the efficiency of excitation at 37.45 GHz passes through a minimum (being almost zero at $h = 6$ mm), then exhibits a broad maximum as h is varied from 8 to 14 mm, and eventually vanishes at $h = 19$ mm.

Apparently, in the former case we are dealing with an H-type WG mode, which is characterized by a single

field variation with respect to the polar coordinate θ and exhibits a maximum at $\theta = \pi/2$. In the latter case, we observe an H-type resonance with two variations with respect to θ, for which one maximum of the field occurs at $\theta \neq \pi/2$ [7]. Based on these data, it was possible to make the next step toward further rarefaction of the spectrum of the hemispherical dielectric resonator. When the dielectric waveguide exciting the resonance was placed at a point with $h = 6$ mm, we obtained the spectrum of oscillations with a single resonance line in each series (Fig. 1e).

Conclusions. The results of our experimental investigations showed that, by changing the way of excitation of the H-type WG modes in a hemispherical dielectric resonator, it is possible to influence the resonance spectrum. In particular, the spectrum can be rarefied so that the resonance frequencies will be spaced by almost 1 GHz. The obtained set of resonance frequencies of the H-type WG modes excited in a hemispherical dielectric resonator by means of distributed coupling to a dielectric waveguide can have the same density as that of the set of E-type modes excited in the same resonator. These results open a way to utilize the H-type WG modes excited in a hemispherical dielectric resonator, in particular, for the measurement of the complex permittivity of solids and liquids with finite losses.

REFERENCES

1. D. P. Tsarapkin, Radiotekhnika, No. 2, 28 (2002).
2. X. H. Jiao, P. Guillon, L. C. Bermudeg, and P. Auxemery, IEEE Trans. Microwave Theory Tech. **35**, 1169 (1987).
3. V. F. Vzyatyshev, O. I. Gudkov, V. S. Dobromyslov, and V. N. Egorov, Élektron. Tekh., Ser. Élektron. SVCh, No. 5, 27 (1982).
4. J. Krupka, K. Derzakowski, A. Abramovich, *et al.*, IEEE Trans. Microwave Theory Tech. **47**, 752 (1999).
5. S. N. Khar'kovskiĭ, A. E. Kogut, and V. A. Solodovnik, Pis'ma Zh. Tekh. Fiz. **21** (18), 38 (1995) [Tech. Phys. Lett. **21**, 741 (1995)].
6. G. V. Golubnichaya, A. Ya. Kirichenko, A. E. Kogut, *et al.*, Dokl. NAN Ukr. **11**, 80 (2004).
7. Yu. V. Prokopenko, T. A. Smirnova, and Yu. F. Filippov, Zh. Tekh. Fiz. **74** (4), 82 (2004) [Tech. Phys. **49**, 459 (2004)].

Translated by P. Pozdeev

Mechanisms of Grain-Boundary Diffusion in Two-Dimensional Metals

R. Yu. Rakitin, G. M. Poletaev, M. S. Aksenov, and M. D. Starostenkov

Altai State Technical University, Barnaul, Russia

e-mail: genphys@agtu.secna.ru

Received February 17, 2005

Abstract—The mechanisms of diffusion via grain boundaries in two-dimensional metals have been studied by method of molecular dynamics. It is established that the diffusion can proceed by two mechanisms, which results in deviations from the Arrhenius law. The first mechanism is related to the formation of chains of atomic displacements between two dislocation cores along the boundary (for high-angle boundaries, between the regions of contraction and extension); the second mechanism consists in a cyclic exchange of atomic sites near the same dislocation core (for high-angle boundaries, near the defect region). © *2005 Pleiades Publishing, Inc.*

Grain boundaries in metals form regions of high diffusion permeability and are characterized by the grain-boundary diffusion coefficient D_{gr}, which is much higher than the bulk diffusion coefficient D for the same metal. It was established [1–3] that the D_{gr}/D ratio depends on the mutual orientation of grains: this ratio decreases for the boundaries with a greater density of coinciding sites, that is, with a lower density of structural defects (vacancies, interstitial atoms, dislocations) [1, 4]. In the study of grain-boundary diffusion, it is expedient to use the methods of computer simulation.

This Letter presents the results of molecular dynamics simulations used for establishing the mechanisms of diffusion via grain boundaries in two-dimensional (2D) metals (Ni, Cu, and Al). The 2D model was selected because it admits the use of special means for visualization of the trajectories of displaced atoms in the course of diffusion.

The atomic packaging in the 2D dimensional metals studied corresponded to the (111) plane of a bcc lattice. The interatomic interactions were described in terms of the central pairwise Morse potential. The potential parameters were determined based on the values of sublimation energies, bulk compression modulus, and lattice parameters. The atomic motions on the molecular dynamics model were described using the differential Newton equations, which were recalculated at a 10^{-14}-s time step. The range of the potential action was restricted to 8 Å. The temperature of the calculation cell was set via the initial atomic velocities. The grain boundary was created by means of mutual rotation and subsequent conjugation of two crystalline blocks. The obtained configurations of the calculation cell were used as starting structures in the main experiments.

The calculation cell in the numerical experiments contained from 8000 to 10000 atoms. In order to avoid the migration of the grain boundaries outside the calculation cell, the cell boundaries were subject to rigid boundary conditions. In calculations of the diffusion coefficient, the experiment was conducted for 300 ps (3×10^4 iterations) at a constant temperature. The error of determination of the diffusion coefficient in such experiments usually did not exceed several percents. Upon termination of the experiment, the calculation cell was cooled to 0 K, the atomic displacements (relative to the initial positions) were analyzed, and the diffusion coefficient was calculated. The grain boundary width was conditionally taken equal to 5 Å.

First, we have studied the temperature dependence of the grain-boundary diffusion coefficient D_{gr}. In these simulations, the temperature was varied from the initial value, at which the diffusion could be observed by means of molecular dynamics, up to the melting temperature (T_m). Figure 1 shows the plots of $\ln D_{gr} = f(T^{-1})$ for 2D cells of Ni and Al with a grain misorientation angle of $\Theta = 16°$. As can be seen from these data, the behavior of the grain-boundary diffusion coefficient in the metals studied deviates from the Arrhenius law: the plots exhibit bending points at a temperature on the order of $0.7T_m$.

Analogous plots obtained for some other misorientation angles revealed a shift in the bending point. Indeed, the bending point was observed at $0.6T_m$ for a smaller angle ($\Theta = 12°$) and shifted toward higher temperatures ($>0.8T_m$) for a greater angle ($\Theta = 19°$). Upon

a further increase in the misorientation angle, the plots of $\ln D_{gr} = f(T^{-1})$ became linear. The appearance of the bending point on the $\ln D_{gr} = f(T^{-1})$ plots can be explained by assuming that the grain-boundary diffusion in the 2D metals studied proceeds by at least two different mechanisms, whose contributions to the overall diffusion process significantly change at $T \sim 0.7T_m$.

Using the obtained data (Fig. 1), we have calculated the activation energy for the diffusion at various temperatures via grain boundaries with a misorientation angle of $\Theta = 16°$. For $T < 0.7T_m$, these calculations yielded 0.26 eV (Ni), 0.23 eV (Cu), and 0.09 eV (Al); for $\Theta = 16°$. For $T > 0.7T_m$, we obtained 0.87 eV (Ni), 0.43 eV (Cu), and 0.4 eV (Al). For comparison, the activation energies for the diffusion via vacancies in pure 2D metals with the same interatomic potentials are 2.09 eV (Ni), 1.56 eV (Cu), and 1.17 eV (Al).
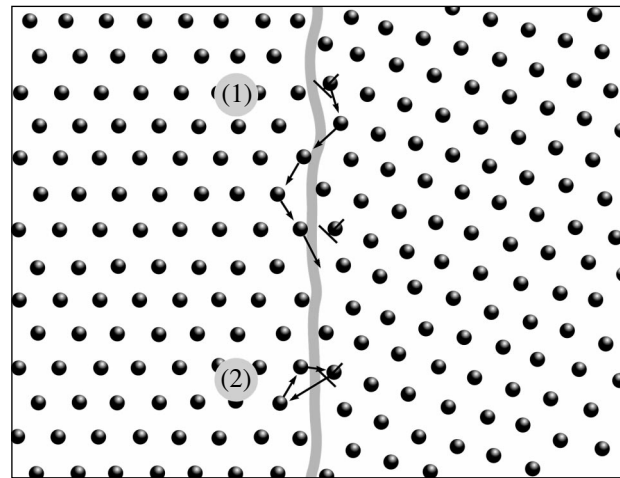
The mechanism of grain-boundary diffusion in the 2D metals was studied with the aid of an atomic displacement trajectory imager. The results of our molecular dynamics simulations showed that an important role in the process of diffusion via grain boundaries is played by an excess volume in the cores of grain-boundary dislocations and by fluctuations in the positions of dislocation cores. The rate of the grain-boundary diffusion in the 2D metals studied increased with the density of the grain-boundary defects.

At $T < 0.7T_m$, the grain-boundary diffusion over low-angle boundaries proceeds predominantly by a mechanism related to the formation of chains of displaced atoms from one dislocation core to another along the boundaries, whereby the interacting dislocations are climbing in the opposite directions. A typical example of diffusion by this mechanism is shown in Fig. 2 (case 1). In the computer experiments, we also frequently observed reverse chains of atomic displacements by which atoms returned to their initial positions. In such cases, higher stability corresponded to the displacement via closed trajectories appearing upon the filling of a vacancy (formed in the primary chain of displacements) by an atom not belonging to that chain.

For high-angle boundaries, the mechanism of diffusion was essentially the same, but the notion about grain-boundary dislocations becomes senseless and should be replaced by the concept of interactions in the pairs of point defects: grain-boundary vacancies and interstitial atoms. The thermal motions of such atoms exhibited chains of displacements (analogous to those observed for low-angle boundaries) between the regions of contraction (interstitial atom) and extension (vacancy).
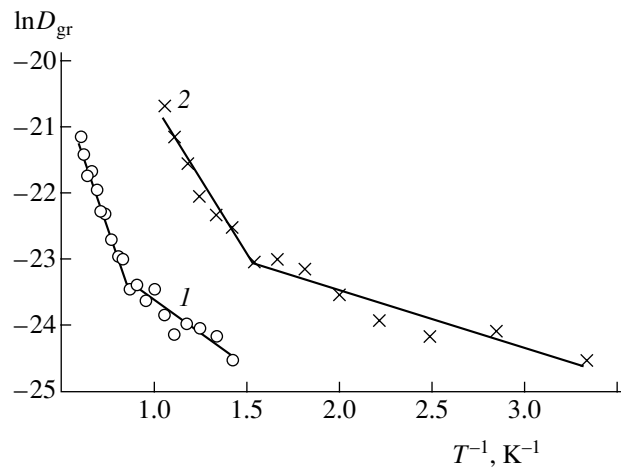
Fig. 1. Plots of $\ln D_{gr}$ versus T^{-1} for 2D cells of (*1*) Ni and (*2*) Al with a grain misorientation angle of $\Theta = 16°$. Solid lines show the linear Arrhenius approximations.

Fig. 2. A schematic diagram illustrating two possible mechanisms of grain-boundary diffusion in 2D metals ($\Theta = 16°$): (1) dislocations climbing via chains of atomic displacements along the grain boundary; (2) cyclic exchange of atomic sites via vacancies. Arrows indicate the atomic displacements on the 1:1 scale; the gray curve indicates the grain boundary.

At temperatures $T > 0.7T_m$, we observed grain-boundary diffusion by a different mechanism, which was analogous to that described previously [5]. This mechanism, consisting in a cyclic exchange of atomic sites near the same dislocation core, is illustrated in Fig. 2 (case 2). In the course of thermal oscillations of atoms, the voids formed at the dislocation cores in the case of large deviations may behave as vacancies. In such moments, the probability that an adjacent atom would occupy such a vacancy increases. The mechanism of cyclic exchange via vacancies (Fig. 2) may also involve more than three atoms, but in all cases this

cyclic process is activated near defect regions at the boundaries. The results of our molecular dynamics simulations showed that this mechanism is most probable at high temperatures and low densities of grain-boundary dislocations.

REFERENCES

1. H. Gleiter and B. Chalmers, *High-Angle Grain Boundaries* (Pergamon Press, Oxford, 1972; Mir, Moscow, 1975).

2. S. Z. Bokshtein, E. V. Bolberova, S. T. Kishkin, *et al.*, Fiz. Met. Metalloved. **58**, 189 (1984).

3. A. N. Aleshin, B. S. Bokshtein, and L. S. Shvindlerman, Poverkhnost, No. 6, 1 (1982).

4. O. A. Kaĭbyshev and R. Z. Valiev, *Grain Boundaries and Properties of Metals* (Metallurgiya, Moscow, 1987) [in Russian].

5. G. M. Poletaev and M. D. Starostenkov, Pis'ma Zh. Tekh. Fiz. **29** (11), 30 (2003) [Tech. Phys. Lett. **29**, 454 (2003)].

Translated by P. Pozdeev

The Nature of the Movement
of a Suspended Piezoelectric Oscillator along a String

V. A. Aleksandrov and G. M. Mikheev*

Institute of Applied Mechanics, Ural Division, Russian Academy of Sciences, Izhevsk, Udmurtia, Russia
* e-mail: gmmikheev@udmnet.ru
Received February 16, 2005

Abstract—A piezoelectric oscillator, suspended with an elastic rod on a string, moves along this string due to the simultaneous excitation of the longitudinal and transverse oscillations in a rod possessing a residual curvature. Devices comprising a piezoelectric oscillator and a beam waveguide have been created and studied. Such systems are prototypes of piezoelectric motors of a new type capable of performing reversible two-way motion. © 2005 Pleiades Publishing, Inc.

Previously, we reported [1] on the phenomenon of vibrational transportation of a suspended piezoelectric oscillator (piezoelement) along a string as a result of the excitation of this oscillator in the range of sound and ultrasound frequencies. The piezoelement was suspended on a string with the aid of a thin metal rod (bracket). By changing the excitation frequency, it was possible to control the velocity and direction of this motion. The observed movements of a suspended piezoelement along the string were explained in terms of the wave transportation related to oscillations generated in the string. However, recently we have established [2] that the movement of a suspended piezoelement ceases as a result of the transverse resonance oscillations of the string and proceeds only at the sites where such oscillations are absent. In this context, it was of interest to elucidate the nature of the observed phenomena.

Experimental arrangement. The experiments were performed using a specially designed device comprising a rod (beam waveguide) with a piezoelectric oscillator on one end and two miniature piezoelectric sensors (piezotransducers) soldered at the other end. The latter transducers were oriented in mutually perpendicular directions so as to monitor the longitudinal and bending vibrations of the rod.

The experiments were performed according to three schemes, in which the device described above was the main element. In the first scheme, (Fig. 1a) the device was hung with the second bent end (bearing the piezotransducers) on a horizontal string. In the second scheme (Fig. 1b), the device was arranged vertically and rigidly fastened to a support, so that the oscillator was at the top and the bent end, carrying a copper ring, was at the bottom. Finally, the device carrying a ring could be arranged horizontally, as depicted in the third scheme (Fig.1c). The response signals from the miniature piezotransducers were detected, amplified, and fed

to a double-beam oscilloscope. In order to provide for an increase in the amplitude of oscillations, the oscillator was made of two commercial piezoelements of the ZP-4 type. The oscillator was excited by a sinusoidal voltage with an amplitude of 25 V supplied via flexible leads from an audiofrequency oscillator.

In the above device, the beam waveguide was made of a piece of elastic copper wire with a diameter of $d =$
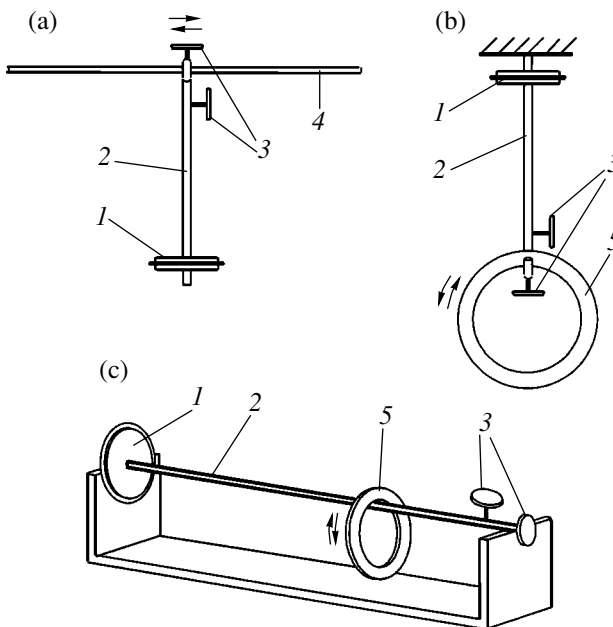
Fig. 1. Schematic diagram showing a device comprising a straight rod (beam waveguide) with a piezoelement (oscillator) on one end (a) moving along a string, (b) inducing the rotation of a ring hanging on the bent free end, and (c) inducing the rotation of a ring suspended on the horizontal rod: (*1*) piezoelement; (*2*) metal rod; (*3*) piezotransducers; (*4*) string; (*5*) rings.
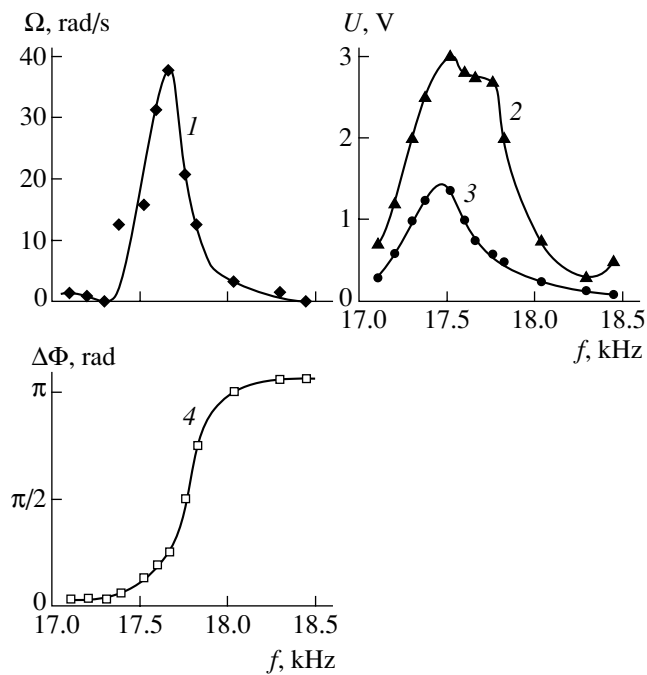
Fig. 2. Plots of the (*1*) ring rotation speed, (*2, 3*) response signal amplitudes U from the piezotransducers monitoring the stretching and bending oscillations, respectively, and (*4*) phase difference $\Delta\Phi$ between the stretching and bending oscillations in the rod versus frequency f of the sinusoidal driving signal.

0.62 mm, a length of $L = 100$ mm, and the following physical characteristics: density, $\rho = 7.72 \times 10^3$ kg/m^3; Young's modulus, $E = 223 \times 10^9$ Pa; shear modulus, $\mu = 87 \times 10^9$ Pa; Poisson ratio, $\sigma = 0.28$. A copper ring for the scheme in Fig. 1b had a thickness of 0.5 mm and inner and outer diameters of 16 and 22 mm, respectively. In the scheme of Fig. 1c, the ring was 0.5 mm thick and had inner and outer diameters of 7 and 11 mm, respectively.

Using the schemes depicted in Figs. 1a–1c, it was possible to study the excitation and movement of the device along the string and the rotation of copper rings on the bent end of the rod and on the horizontal rod, respectively.

Results and discussion. The results of preliminary experiments showed that the motion of the oscillating piezoelement suspended on the string with the aid of the elastic rod is independent of the string characteristics (material, length, tension) but significantly depends on the frequency of oscillations. The experiments according to the schemes presented in Fig. 1 revealed a sharp increase in the amplitudes U of the response signals of piezotransducers at certain frequencies f_i of the sinusoidal driving signal, which was indicative of the resonance excitation of longitudinal (stretching) and transverse (bending) oscillations in the rod. This was accompanied by the motion of the device along the string or by the rotation of suspended rings. Variation of

the frequency f of the driving generator (and, hence, of the driven oscillator) in the vicinity of f_i values led to significant nonmonotonic changes in the velocity V of the device motion along the string and in the speed of rotation Ω of the rings (Fig. 2, curve *1*). By tuning the drive frequency f, it was possible to reach the local maxima of $V = V_{max}$ and $\Omega = \Omega_{max}$, which increased with the f_i values. The directions of transportation and rotation could be also changed by selecting an appropriate resonance frequency f_i. It should be noted that the frequencies of the response signals from piezotransducers were always the same and equal to the frequency of the driving electric signal applied to the oscillator.

The measured signals were superimposed on the noise generated as a result of the friction accompanying the motion of the device along the string and the rotation of the rings. Measurements of the response signals from the piezotransducers for a device removed from the string and bearing no rings gave pure sinusoidal signals. Thus, it was possible to compare the response amplitudes U (Fig. 2, curves *2* and *3*) and to determine the phase difference $\Delta\Phi$ (Fig. 2, curve *4*) of the stretching and bending oscillations in the rod excited in the vicinity of any of the resonance frequencies f_i. As can be seen from Fig. 2, the maximum speed of ring rotation corresponds to a phase difference of $\pi/4$ between stretching and bending oscillations in the rod.

Our investigation showed that the suspended piezoelement moved along the string at the same frequencies of the driving generator as those inducing the rotation of a suspended ring. The experiments with a horizontal device (Fig. 1c) revealed certain positions on the rod with the corresponding coordinates x_n ($n = 0, 1, 2, \ldots$) where the ring did not rotate. For a given resonance frequency f_i, the spacing $\Delta x_n = x_{n+1} - x_n$ between such points was independent of the number n. As f_i increases, the Δx_n value decreases. It was also established that, at certain resonance frequencies, the ring positioned in different regions of the rod rotates in opposite directions.

The whole body of experimental data presented above shows that the transportation of a suspended piezoelement along the string and the rotation of a ring on the rod is related to mutually perpendicular stretching and bending oscillations simultaneously excited by the piezoelement in the rod. As is well known, rods can simultaneously feature stretching, twisting, and bending oscillations in the form of elastic waves. However, the stretching and twisting waves in straight rods have rather high velocities and can be excited only at relatively high frequencies. The bending waves propagate at much lower velocities and can be excited at lower frequencies [3]. In addition, any straight rod in practice has a certain residual curvature [4]. For this reason, any such rod with one free end acquires an additional longitudinal toughness, whereby it straightens on stretching and bends on contraction. Thus, the excitation of longitudinal oscillations at certain frequencies must

lead to the simultaneous excitation of bending oscillations at the same frequency, in agreement with what was observed in our experiment. The stretching and bending oscillations in the rod are mutually perpendicular and, depending on the excitation frequency, may have different phases in various regions (Fig. 2). As a result, the free end of the rod moves along an elliptical trajectory, the parameters of which depend on the amplitudes and phases of the stretching and bending modes.

If the free end of the rod is suspended on a string (Fig. 1a), the longitudinal oscillations of the rod are perpendicular to the string, whereas the transverse oscillations are performed along the string. When the free end moves upward, the static friction force decreases (because of a lower reaction of the support); on the contrary, the downward motion of the free end increases the support reaction and, hence, the static friction force. Thus, the static friction force varies together with the longitudinal oscillations. In combination with the rod bending in the directions along the string, these variations induce the motion of the suspended rod along the string as a result of the mechanical rectification of oscillations [5]. As can be readily seen, the direction of this motion depends on the phase difference between the stretching and bending oscillations in the rod, while the velocity of this motion is proportional to the frequency of oscillations and increases with their amplitude.

An analogous behavior is observed in the experiments with a ring hanging on the free bent end of the rod (Fig. 1b). The only difference is that the static friction force in this case increases when the free end of the rod moves upward, and this force decreases when the rod end moves downward. By the same token, the direction of ring rotation depends on the sign of the phase difference $\Delta\Phi$ between the stretching and bending oscillations in the rod, while the rotation velocity reaches a maximum for $\Delta\Phi = \pm\pi/4$, is proportional to the driving frequency, and depends on the amplitudes of both mutually perpendicular oscillation modes, also in agreement with experiment (Fig. 2).

Finally, the rotation of a ring on the horizontal rod (Fig. 1c) can also be explained in a similar way. Here, a certain difference consists in that the motion of the ring is induced by the bending oscillations of the rod having both horizontal and vertical components. The absence of rotation in certain regions of the rod is indicative of the appearance of nodes of the standing transverse waves.

Conclusions. Transportation of an oscillating piezoelement with a suspending rod along the string is related to the simultaneous excitation of the mutually perpendicular longitudinal (stretching) and transverse (bending) oscillations in a rod possessing a residual curvature. The direction of motion depends on the sign of the phase difference between the two oscillation modes, while the maximum transportation velocity is reached at a phase difference of $\pm\pi/4$. Analogous factors account for the rotation of a ring suspended on the oscillating rod. The obtained results can be used for the development of piezoelectric motors of a new type capable of performing reversible two-way motion.

REFERENCES

1. V. A. Aleksandrov, Datchiki Sistemy, No. 6, 35 (2001).
2. V. A. Aleksandrov and G. M. Mikheev, Pis'ma Zh. Tekh. Fiz. **30** (13), 71 (2004) [Tech. Phys. Lett. **30**, 563 (2004)].
3. L. D. Landau and E. M. Lifshitz, *Course of Theoretical Physics,* Vol. 7: *Theory of Elasticity* (Nauka, Moscow, 1987; Pergamon, New York, 1986).
4. V. N. Chelomei, *Selected Works* (Mashinostroenie, Moscow, 1989) [in Russian].
5. V. V. Lavrinenko, I. A. Kartashev, and V. S. Vishnevskiĭ, *Piezoelectric Engines* (Énergiya, Moscow, 1980) [in Russian].

Translated by P. Pozdeev

Application of a Modified Collocation Method in the Theory of Antennae

S. I. Éminov

Novgorod State University, Novgorod, Russia
e-mail: tel@novsu.ac.ru; theorphy@novsu.ac.ru

Abstract—Collocation on a step basis, which is one of the most widely used methods in the theory of antennae, is insufficiently effective in solving excitation problems. A more effective modified method, which is based on analytical inversion of the main part of the hypersingular operator, is proposed. © *2005 Pleiades Publishing, Inc.*

Introduction. Analysis of modern trends in computational electrodynamics shows that many approaches to the theory of antennae use the method of collocation based on a step basis for solving problems involving integral equations. The wide use of this method is explained by the following factors: (i) simple and universal formalism; (ii) mathematical justification has been given for some equations [1]; and (iii) a generalized collocation procedure has been developed for the problems of diffraction on arbitrary curvilinear surfaces [2]. However, the possibilities of the classical collocation method in solving the problems of antenna excitation are rather limited, since the internal convergence of solutions is slow. This disadvantage is related to the fact that the primary field in such problems is localized in a small (relative to the characteristic antenna size) spatial region.

This Letter describes a modified variant of the collocation method, which provides for a high efficiency in solving excitation problems.

Description of the collocation method. The basic method will be formulated in application to a hypersingular integral equation of the following type:

$$(Au)(\tau) + (Nu)(\tau) = \nu(\tau), \quad -1 \le \tau \le 1, \quad (1)$$

where

$$(Au)(\tau) = \frac{1}{\pi}\frac{d}{d\tau}\int_{-1}^{1} u(t)\frac{\partial}{\partial t}\ln\frac{1}{|\tau - t|}dt,$$

$$(Nu)(\tau) = \int_{-1}^{1} N(\tau, t)u(t)dt.$$

Let us subdivide the interval [–1, 1] into n equal parts of length $h = \dfrac{2}{n}$, where n is an integer. Let us

denote the boundaries of the jth intervals by $a_j = -1 + (j-1)h$, $b_j = -1 + jh$, set the collocation points $\gamma_i = -1 + (i-1)h + \dfrac{h}{2}$ at the middle of each interval, and introduce the basis set functions

$$\varphi_j(\tau) = \begin{cases} 1, & \text{if} \quad \tau \in [-a_j, b_j] \\ 0, & \text{if} \quad \tau \notin [-a_j, b_j]. \end{cases} \quad (2)$$

Expanding an unknown function in the basis set,

$$u(\tau) = \sum_{j=1}^{n} c_j \varphi_j(\tau), \quad (3)$$

substituting this expansion into Eq. (1), and considering this equation at the collocation points (i.e., sequentially putting $\tau = \gamma_1, \gamma_2, \dots, \gamma_n$), we obtain a system of linear algebraic equations:

$$\sum_{j=1}^{n} c_j (A\varphi_j)(\gamma_i) + \sum_{j=1}^{n} c_j (N\varphi_j)(\gamma_i) = \nu(\gamma_i), \quad (4)$$
$$1 \le i \le n.$$

The matrix elements of the hypersingular operator A can be found analytically. Indeed, taking into account that

$$(A\varphi_j)(\tau) = \frac{1}{\pi}\frac{d}{d\tau}\int_{a_j}^{b_j} \frac{\partial}{\partial t}\ln\frac{1}{|\tau - t|}dt$$

$$= \frac{1}{\pi}\frac{d}{d\tau}\left(\ln\frac{1}{|\tau - b_j|} - \ln\frac{1}{|\tau - a_j|}\right) = \frac{1}{\pi}\left(\frac{1}{\tau - a_j} - \frac{1}{\tau - b_j}\right),$$

we obtain

$$(A\varphi_j)(\gamma_i) = \frac{1}{\pi}\left(\frac{1}{\gamma_i - a_j} - \frac{1}{\gamma_i - b_j}\right). \quad (5)$$

Determination of the matrix elements of the operator N reduces to the calculation of one-dimensional integrals

$$(N\varphi_j)(\gamma_i) = \int\limits_{a_j}^{b_j} N(\gamma_i, t)u(t)dt. $$

Thus, the essence of the collocation method consists in solving system of equations (4), determining the unknown coefficients c_j, and calculating the unknown function by formula (3).

Convergence of the collocation method. The convergence of the method described above will be considered in application to the equation of dipole antennae (see Appendix). The right-hand part of this equation can be written as

$$E^0(\tau) = \frac{U_0}{2T}\begin{cases} 1, & |\tau| \le \dfrac{T}{l} \\ 0, & |\tau| > \dfrac{T}{l}, \end{cases} \quad (6)$$

where $2T$ is the length of an interval in which the primary field is nonzero and $2l$ is the total antenna length.

The values of the input impedance defined by the formula

$$Z = \frac{U_0}{I(0)} \quad (7)$$

are presented in the tables for various numbers of the basis functions and different values of the ratio T/l. Table 1 presents the results of calculations performed using the conventional method for $T/l = 1$, that is, for the case when the primary field is uniformly distributed over the dipole length (diffraction problems). As can be seen, the collocation method exhibits good convergence in this case.

Table 2 presents data on the input impedance for the lower values of T/l. As this ratio decreases, the rate of convergence drops. For small T/l (excitation problems), the collocation method is practically inapplicable.

Table 1. The input impedance of a dipole calculated using the conventional collocation method for $T/l = 1$

N	$(kl) = \dfrac{\pi}{2}, \dfrac{l}{a} = 50, \dfrac{T}{l} = 1$		$(kl) = \dfrac{\pi}{4}, \dfrac{l}{a} = 50, \dfrac{T}{l} = 1$	
	ReZ	ImZ	ReZ	ImZ
10	125.99	140.23	36.086	−487.95
20	122.93	92.440	34.822	−598.166
40	121.44	84.672	34.309	−621.04
60	121.01	84.883	34.170	−623.20
80	120.81	84.772	34.105	−624.20
100	120.69	84.600	34.065	−624.19
200	120.46	83.939	33.987	−629.15
300	120.39	83.383	33.960	−630.51

Table 2. The input impedance of a dipole calculated using the conventional collocation method for $T/l = 0.05$ and 0.02

N	$(kl) = \dfrac{\pi}{2}, \dfrac{l}{a} = 50, \dfrac{T}{l} = 0.05$		$(kl) = \dfrac{\pi}{2}, \dfrac{l}{a} = 50, \dfrac{T}{l} = 0.02$	
	ReZ	ImZ	ReZ	ImZ
20	50.052	28.946		
40	98.086	49.799		
60	148.02	73.302	59.210	29.321
80	97.144	49.663	79.341	38.438
100	80.283	41.624	99.584	47.352
120	96.719	49.362	119.92	56.115
140	84.157	43.372	140.352	64.762

Modified collocation method. First, let us consider an equation containing only the hypersingular operator:

$$(Au_1)(\tau) = \frac{1}{\pi}\frac{d}{d\tau}\int\limits_{-1}^{1} u_1(t)\frac{\partial}{\partial t}\ln\frac{1}{|\tau - t|}dt = v(\tau), \quad (8)$$
$$-1 \le \tau \le 1.$$

A solution to this equation can be obtained in an analytical form [3]:

$$u_1(\tau) = \frac{2}{\pi}\int\limits_{-1}^{1} v(\tau) \quad (9)$$
$$\times\left(\frac{\ln 2}{2} + \ln\sin\frac{\theta(t) + \theta(\tau)}{2} - \frac{1}{2}\ln|\tau - t|\right)dt,$$

where $\theta(t) = \arccos(t)$.

Table 3. The input impedance of a dipole calculated using a proposed modified collocation method for $T/l = 0.05$ and 0.02

N	$(kl) = \dfrac{\pi}{2}$, $\dfrac{l}{a} = 50$, $\dfrac{T}{l} = 0.05$		$(kl) = \dfrac{\pi}{2}$, $\dfrac{l}{a} = 50$, $\dfrac{T}{l} = 0.02$	
	ReZ	ImZ	ReZ	ImZ
11	124.04	85.381	124.39	77.049
21	103.98	54.980	104.45	50.738
41	98.724	49.780	101.35	47.418
61	98.006	49.861	100.93	47.692
81	97.465	49.682	100.48	47.556
101	97.181	49.537	99.931	47.278

Now, let us seek a solution to Eq. (1) in the form of a sum:

$$u = u_1 + u_2.$$

Using expression (9), we obtain the following equation for determining the unknown function u_2:

$$(Au_2)(\tau) + (Nu_2)(\tau) = -(Nu_1)(\tau),$$
$$-1 \le \tau \le 1. \tag{10}$$

The right-hand part of this equation (in contrast to the right-hand part of Eq. (1)) can be expanded into a rapidly converging series, and, hence, Eq. (10) can be effectively solved using the conventional collocation method. The results of calculations presented in Table 3 confirm the good internal convergence of the proposed method.

The modified method is based on a numerical-analytical procedure. A solution is obtained in the form of a sum of two components, one of which is obtained analytically and the other, by using a numerical collocation technique. For this reason, the proposed method is highly effective and completely solves the problem of the calculation of dipoles and many other antennae, as well as the problem of diffraction in the case when the primary field sources are located near the surface of diffraction.

Appendix

Hypersingular equation of a dipole antenna. Consider a tubular cylindrical dipole with a length of $2l$ and a radius of a. Under the action of a primary electric field $E^0(z)$ (assumed to be axisymmetric), axial currents are induced in the ideally conducting surface. The density $j_z(z)$ of these surface currents obeys the following integrodifferential equation:

$$-\left(\frac{d^2}{dz^2} + k^2\right)\iint\limits_{S} j_z(z')\frac{\exp(-ikR)}{4\pi R}dS' = i\omega\varepsilon E_z^0(z), \tag{11}$$

where

$$R = \sqrt{(z - z')^2 + 2a^2[1 - \cos(\varphi - \varphi')]},$$
$$dS' = ad\varphi'dz'.$$

As can be readily shown, the integral in Eq. (11) is independent of the variable φ. Introducing the dimensionless variables defined as

$$z = l\tau, \quad z' = lt, \quad E_z^0(l\tau) = E^0(\tau),$$
$$I(\tau) = 2\pi a j_z(l\tau), \tag{12}$$

we can rewrite Eq. (11) in the following form:

$$-\frac{1}{4\pi}\left(\frac{d^2}{d\tau^2} + (kl)^2\right)\int\limits_{-1}^{1} B(\tau, t)I(t)dt = il\sqrt{\frac{\varepsilon}{\mu}}E^0(\tau), \tag{13}$$

where

$$B(\tau, t) = \frac{1}{2\pi}\int\limits_{0}^{2\pi} \frac{\exp(-i\tilde{R})}{\tilde{R}}d\psi$$

$$= \frac{1}{2\pi}\int\limits_{-\pi}^{\pi} \frac{\exp(-i\tilde{R})}{\tilde{R}}d\psi = \frac{1}{\pi}\int\limits_{0}^{\pi}\frac{\exp(-i\tilde{R})}{\tilde{R}}d\psi, \tag{14}$$

$$\tilde{R} = \sqrt{(kl)^2(\tau - t)^2 + 4(ka)^2\sin^2\frac{\psi}{2}}.$$

Now let us separate the logarithmic singularity in the kernel. This can be achieved by subtracting from and adding to the integrand in Eq. (14) a function possessing the same singularity but integrable in an analytical form:

$$B(\tau, t) = \frac{1}{\pi}\int\limits_{0}^{\pi}\left[\frac{\exp(-i\tilde{R})}{\tilde{R}} - \frac{1}{\sqrt{(kl)^2(\tau - t)^2 + (ka)^2\psi^2}}\right]d\psi$$

$$+ \frac{1}{\pi}\int\limits_{0}^{\pi}\frac{1}{\sqrt{(kl)^2(\tau - t)^2 + (ka)^2\psi^2}}d\psi.$$

Taking the second integral in the analytical form, we eventually obtain

$$B(\tau, t) = \frac{1}{\pi}\int\limits_{0}^{\pi}\left[\frac{\exp(-i\tilde{R})}{\tilde{R}} - \frac{1}{\sqrt{(kl)^2(\tau - t)^2 + (ka)^2\psi^2}}\right]d\psi$$

$$+ \frac{1}{\pi(ka)}\ln\left[\frac{\pi a}{l} + \sqrt{\left(\frac{\pi a}{l}\right)^2 + (\tau - t)^2}\right] + \frac{1}{\pi(ka)}\ln\frac{1}{|\tau - t|} \tag{15}$$

$$\equiv \frac{1}{\pi(ka)}\ln\frac{1}{|\tau - t|} + B_1(\tau, t).$$

Taking into account expression (15) and using Eq. (13), we obtain the final integrodifferential equations:

$$\beta(AI)(\tau) + (KI)(\tau) = il\sqrt{\frac{\varepsilon}{\mu}}E^0(\tau), \qquad (16)$$

where

$$\beta = \frac{1}{4\pi(ka)},$$

$$(AI)(\tau) = \frac{1}{\pi}\frac{d}{d\tau}\int_{-1}^{1} I(t)\frac{\partial}{\partial t}\frac{1}{|\tau - t|}dt,$$

$$(KI)(\tau)$$
$$= -\frac{(kl)^2}{4\pi}\int_{-1}^{1} B(\tau, t)I(t)dt - \frac{1}{4\pi}\frac{d^2}{d\tau^2}\int_{-1}^{1} B_1(\tau, t)I(t)dt.$$

REFERENCES

1. I. K. Lifanov, *Method of Singular Integral Equations and Numerical Experiment* (Yanus, Moscow, 1975) [in Russian].
2. E. V. Zakharov and Yu. V. Pimenov, *Numerical Analysis of Radio Wave Diffraction* (Radio i Svyaz', Moscow, 1982) [in Russian].
3. S. I. Éminov, Pis'ma Zh. Tekh. Fiz. **30** (22), 8 (2004) [Tech. Phys. Lett. **30**, 933 (2004)].

Translated by P. Pozdeev

Coherent Helical Structures in Swirl Flows

S. I. Shtork[a],*, C. E. Cala[b], E. C. Fernandes[b], and M. V. Heitor[b],**

[a] *Institute of Thermophysics, Siberian Division, Russian Academy of Sciences, Novosibirsk, 630090 Russia*
[b] *Laboratory of Thermofluids, Combustion, and Energy Systems, Center for Innovation,
Technology, and Policy Research, Technical University of Lisbon, 1049–001 Lisbon, Portugal*
*e-mail: * kuibin@itp.nsc.ru; ** mheitor@ist.uti.pt*
Received March 15, 2005

Abstract—A nonstationary flow with rotating helical filaments formed in the region of swirl flow breakdown has been studied using the method of phase averaging of the output signal of a laser Doppler velocimeter. Vortices in the measured flow field were separated using the λ_2 technique based on an analysis of the velocity gradient tensor. It is shown for the first time that precession of the central monopolar vortex is accompanied by the formation of a pair of secondary vortices with the opposite directions of circulation, which form a helical dipole structure. © 2005 Pleiades Publishing, Inc.

The investigations into swirl flows are important from the standpoint of practical applications, especially in view of widely used vortex combustors. On the other hand, swirl flows exhibit a rich variety of flow regimes and accompanying effects and, hence, are of considerable basic interest [1]. One of the most intriguing phenomena encountered in swirl flows is the vortex breakdown, which still remains incompletely clear.

This Letter presents the results of an experimental investigation of a flow structure formed upon breakdown of an intense swirl flow outgoing from a model vortex combustor. These conditions are characterized by the appearance of high-power regular flow oscillations caused by a precessing vortex core (PVC).

The experiments were carried out with an isothermal swirl flow outgoing from a cylindrical nozzle into unbounded space. The flow swirling was provided by an axisymmetric paddle vortexer. The working fluid was air at room temperature (20°C). Detailed flow velocity measurements were performed in a selected regime with a Reynolds number Re = dU/ν = 15000 (where d = 56 mm is the nozzle diameter, U is the average flow velocity in the nozzle, and ν is kinematic viscosity) and a swirl parameter of S = 1.0. These conditions correspond to the regime in a real combustor used in combustion experiments [2].

The flow velocity fields were studied using a standard single-component laser Doppler velocimeter (Dantec Co.) with phase averaging of the output signal. The pressure sensor positioned at the nozzle output generated a base signal following the phase of oscillations. The phase averaging was performed over points in the r–z plane of the (r, z, θ) cylindrical coordinate system. A periodic pulsation of the flow velocity at the points of measurement was related to the rotation of a nonaxisymmetric flow field. Accordingly, the phase angle of pulsation was used as the spatial angle θ (the

complete cycle of oscillations corresponded to the flow rotation by 360°), which made possible restoration of the phase-averaged three-dimensional flow structure inside a cylindrical region.

Vortices in the measured flow field were separated using an approach proposed Jeong and Hussain [3]. This approach proceeds from a necessary and sufficient condition for recognizing the vortex core with allowance for the principle of minimum pressure, while excluding the effects of viscosity and nonstationary flow. The proposed method, called the λ_2 technique, is based on the search for conjugated flow regions with negative values of λ_2, the second eigenvalue of the axisymmetric tensor $\mathbf{S}^2 + \mathbf{\Omega}^2$, where $\mathbf{S}$ and $\mathbf{\Omega}$ denote the symmetric and antisymmetric parts, respectively, of the velocity gradient tensor $\nabla\mathbf{V}$, and $\mathbf{V}$ is the flow velocity vector field. Since the λ_2 value is calculated in terms of the velocity derivatives, this technique is applicable to the moving vortexlike objects.

Figure 1a shows the typical phase-averaged flow structure behind the combustor nozzle as imaged by the of zero-λ_2 isosurface bounding the vortex flow regions (rotating in the swirling direction at a rate of 75.5 Hz). Two large entangled helical vortices embedded one into another are referred to as the recirculation vortex (RV) and the outer vortex (OV). The OV determines mixing of the gas flow at the outer boundary, while the RV forms a paraxial region of the reverse flow (recirculation zone) ensuring stabilization of the flame. The vortices in Fig. 1a represent secondary structures appearing as a result of the swirl flow breakdown upon leaving the nozzle. The main PVC formed inside the nozzle is hidden in this image, but it can distinguished in both transverse and longitudinal sections presented in Figs. 1b and 1c together with the vector fields. As can be seen, the longitudinal section crosses the secondary vortices almost at a right angle and the main PVC,
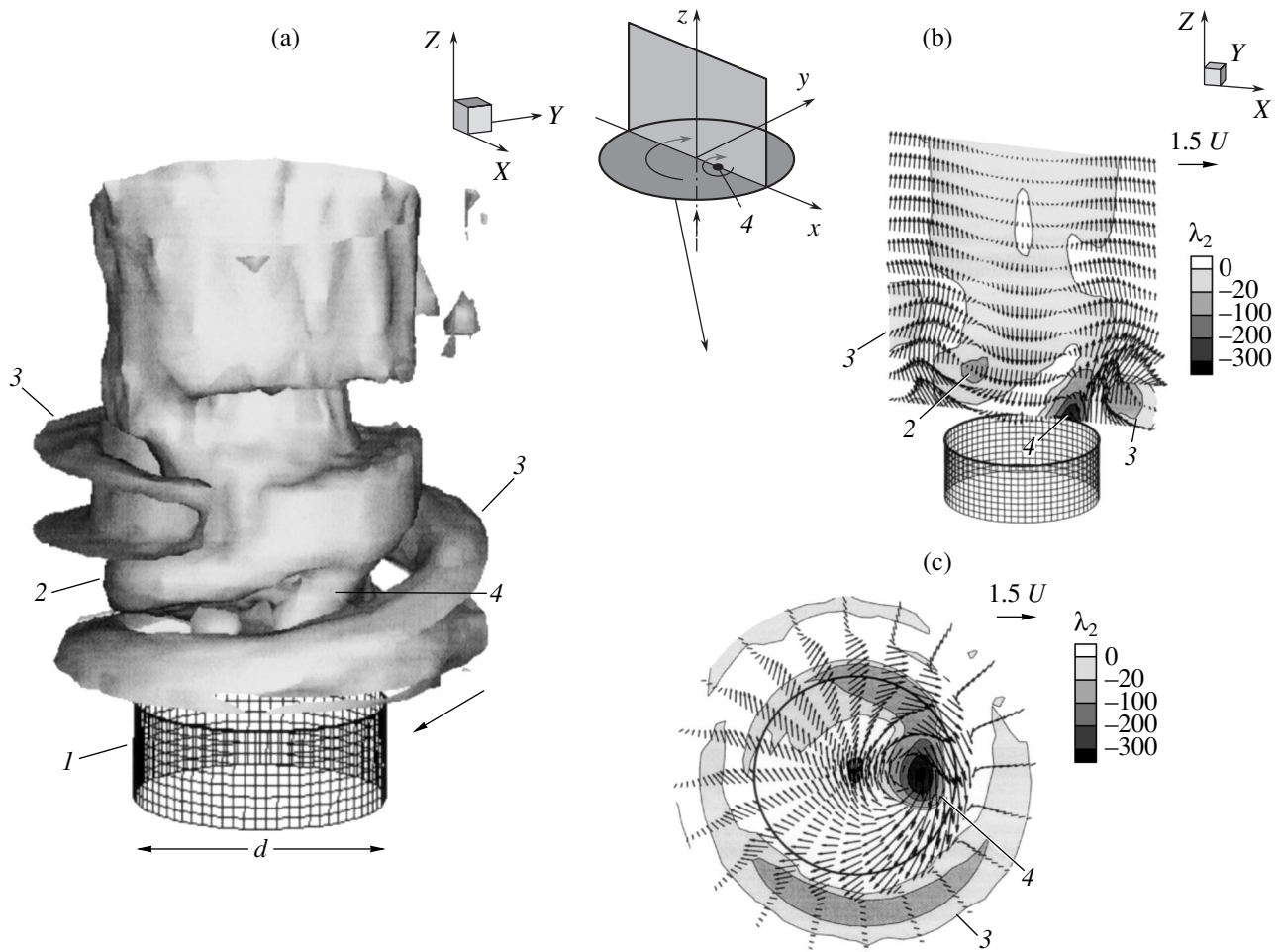
Fig. 1. The typical structure of a swirl flow behind the nozzle edge (air flowing from bottom to top) revealed by (a) the $\lambda_2 = 0$ iso-surface imaging the boundaries of vortices and (b, c) the velocity fields and λ_2 isolines in the vertical (longitudinal) and horizontal (transverse) sections, respectively (λ_2 levels are expressed in $(d/U)^{-2}$ units): (1) nozzle output; (2) recirculation vortex (RV); (3) outer vortex (OV); (4) precessing vortex core (PVC). Bent arrows indicate the directions of flow rotation.

along the axis. Immediately at the nozzle output, the PVC intensity is several times that of the secondary vortices. This can be judged from the corresponding λ_2 values (lower negative values correspond to a more pronounced pressure minimum at the vortex core).

Figure 2 shows the reconstructed axes of all three vortices formed in the flow field under consideration. The arrows indicate the vortex signs determined using the velocity vectors. As can be seen from this vortex configuration. All the helices are left-handed, that is, their directions are opposite to that of the flow rotation. For the inner RV and the PVC, this is a necessary condition of conjugation with a paraxial region of the reverse flow [4]. In turn, the OV geometry is apparently determined by the RV and the PVC configurations. The interaction between the inner secondary vortex and the PVC results in absorption of the latter upon a preliminary significant decrease in intensity. Thus, the PVC exists over a distance less than $(0.5–0.6)d$ from the noz-

zle edge, whereas the secondary vortices can be traced up to a distance on the order of $1.5d$.

A very interesting feature of the swirl flow morphology is that the secondary helical vortices having the opposite directions (signs) of circulation form a system with parallel local vortex tubes. This configuration exhibits a clear dipole character, much like that of the structures recently theoretically studied in [5]. In the general case, a dipole consisting of two point vortices in a plane possesses a linear momentum, which accounts for its propagation in space. The direction of propagation is determined by the signs of the vortices: in the configuration depicted in Fig. 2, the dipole moment is directed downstream. This effect probably accounts for the fact that the secondary vortices (RV and OV) forming the dipole can travel a longer distance from the nozzle edge than does the monopolar PVC. Note that this dipole structure clearly differs from the
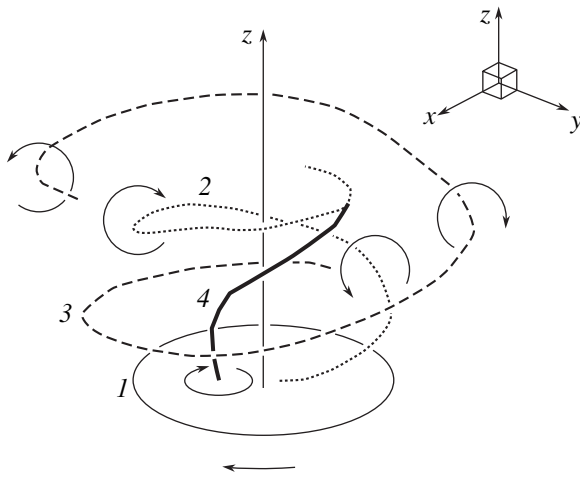
Fig. 2. The reconstructed axes of three large-scale vortices revealed in the flow field. Notation is the same as in Fig. 1.

previously discovered double-helix structure formed by a couple of right-handed vortices [6].

A physical mechanism responsible for the formation of internal and external secondary vortices is analogous to that demonstrated by the results of numerical simulation of a swirl flow breakdown [1], according to which it is a cone shape of the flow in the region of breakdown that leads to the formation of internal and external shear layers with azimuthal vorticity of the opposite signs. Then, an instability is developed that leads to bending of these layers with the formation of large-scale vortices circulating in opposite directions. Subsequent evolution of these vortices into a dipole structure reflects the basic ability of vortex tubes to exhibit antiparallel self-orientation, which was confirmed, in particular, by the recent numerical calculations of isotropic turbulence [7].

It should be noted that helical vortexlike structures of the dipole type, representing two conjugated counter-circulating helical filaments inducing the rotation of surrounding fluid in the opposite directions, were never reported previously. Such structures offer a convenient object for experimental verification of the helical dipole models developed in recent years [5]. A practical significance of the obtained results consists in that secondary vortices play an important role in the dynamics of a swirl flow in a combustor, contributing to the intensification of flow mixing, stabilizing the burning process, and favoring a decrease in the torch length.

REFERENCES

1. W. Kollmann, A. S. H. Ooi, M. S. Chong, and J. Soria, J. Turbulence **2** (005) (2001).

2. P. M. Anacleto, E. C. Fernandes, M. V. Heitor, and S. I. Shtork, Combust. Sci. Technol. **175**, 1369 (2003).

3. J. Jeong and F. Hussain, J. Fluid Mech. **285**, 69 (1995).

4. S. V. Alekseenko, P. A. Kuibin, V. L. Okulov, and S. I. Shtork, J. Fluid Mech. **382**, 195 (1999).

5. V. L. Okulov and Ya. Fukumoto, Dokl. Ross. Akad. Nauk **399**, 56 (2004) [Dokl. Phys. **49**, 662 (2004)].

6. S. V. Alekseenko and S. I. Shtork, Pis'ma Zh. Éksp. Teor. Fiz. **59**, 746 (1994) [JETP Lett. **59**, 775 (1994)].

7. S. Goto and S. Kida, Fluid Dyn. Res. **33**, 403 (2003).

Translated by P. Pozdeev

Analysis of the Melting Thermograms of Thin Refractory Metal Plates Heated by Laser Radiation with Harmonically Modulated Intensity

L. G. D'yachkov*, A. V. Kostanovskiy, and M. E. Kostanovskaya

Institute for High Energy Densities, Associated Institute for High Temperatures, Russian Academy of Sciences, Moscow, Russia

* e-mail: dyachk@mail.ru

Received March 25, 2005

Abstract—The results of experimental and theoretical investigations show the possibility of identifying the solid–liquid phase transition in a refractory metal plate heated by laser radiation with harmonically modulated intensity. Thermograms measured in a single-phase region of a heated sample surface display a harmonic component with a constant amplitude and frequency, which exhibits degeneracy in a two-phase state when the melting takes place. At temperatures in the vicinity of the melting point T_m, the thermograms exhibit lower ($T < T_m$) and upper ($T > T_m$) half-waves of variable amplitudes, with intermediate short intervals corresponding to $T = T_m$. The time periods featuring the lower and upper half-waves are separated by a longer interval corresponding to a two-phase state ($T = T_m$). The results of analytical calculations qualitatively agree with experimental data. © 2005 Pleiades Publishing, Inc.

When a thin metal plate is heated by laser radiation with harmonically modulated intensity, the sample temperature in a single-phase state below the melting point ($T < T_m$) also acquires a harmonic component. However, the shape of the thermogram exhibits a qualitative change when the sample is heated to the melting temperature (Fig. 1). The process of melting under such conditions has practically not been studied. The aim of this investigation was to analyze the problem theoretically and apply the theory to interpretation of the obtained experimental data.

Experiment. A thin refractory metal plate was heated by radiation of a continuous YAG:Nd^{3+} laser (LTN-102 type) operating at a wavelength of 1.06 μm with an output power of 250 W. The laser beam was normally incident on the sample surface and focused into a spot with a diameter of 1.5 mm. The heat flux monitored using a laser power meter showed that the power density in the laser spot was on the order of 10^7 W/m^2 and had a harmonic component at a frequency of 50 Hz. The sample temperature in the spot was measured by a fast-response micropyrometer (~10^{-5} s) operating at 0.65 μm and probing a spot with a diameter of 0.3 mm. The pyrometer was incorporated into a computer-controlled system of data acquisition and processing based on a Velleman PCS500 storage oscilloscope and calibrated in the temperature range from 1000 to 3000 K with respect to a blackbody model [1] using a reference optical pyrometer.

The sample, made of a tantalum (99.9% Ta) foil with a thickness of $H = 80$ μm, was heated by laser radiation in high-purity argon at a pressure of ~1.5×10^5 Pa. The time required for heating the foil to a temperature close to the melting point (T_m) of tantalum was ~0.4 s. The results of the sample temperature measurements in the course of laser-induced heating have the form of thermograms [2]. Figure 1 shows a typical experimental curve.
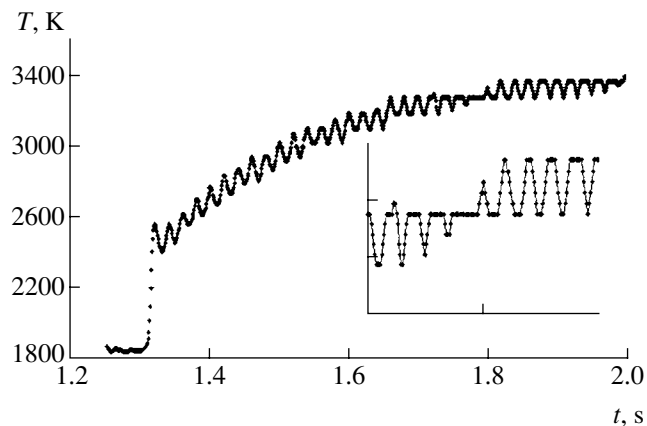
Fig. 1. The typical experimental thermogram of a 80-μm-thick pure tantalum foil heated by laser radiation with harmonically modulated intensity. The inset shows the region of a two-phase state on a greater scale (see the text for explanations).

Theory. In a single-phase state at $T < T_m$, the process of heating of a thin plate is described by the equation of heat conduction,

$$\frac{\partial T}{\partial t} = a\frac{\partial^2 T}{\partial x^2}, \tag{1}$$

with boundary conditions of the second kind on both surfaces of the plate,

$$\left.\frac{\partial T}{\partial x}\right|_{x=0} = -\frac{q_L(t) - q_r(T)}{\lambda}, \quad \left.\frac{\partial T}{\partial x}\right|_{x=H} = -\frac{q_r(T)}{\lambda}. \tag{2}$$

Here, $a = \lambda/c_p\gamma$ is the thermal diffusivity, λ is the thermal conductivity, c_p is the heat capacity at constant pressure, γ is the sample density, $q_L(t) = q_0 + q_a\cos(\omega t)$ is the intensity of laser radiation absorbed by the sample front ($x = 0$) surface, $q_r(T) = \varepsilon\sigma T^4$ is the intensity of thermal radiation from the heated ($x = 0$) and rear ($x = H$) sample surfaces, ε is the sample emissivity, and σ is the Stefan–Boltzmann constant. The shape of the initial condition $T(x, 0)$ for a thin metal plate is insignificant. This initial temperature profile can be obtained, for example, by solving an additional problem with neglect of q_r and a constant initial condition.

Let us represent the sample temperature $T(x, t)$ as the sum of a slowly varying component $\bar{T}$ and an oscillating component with amplitude T_a:

$$T = \bar{T} + T_a\sin(\omega t + \psi), \tag{3}$$

where ψ is a certain phase. Assuming the oscillation amplitude T_a to be small compared to $\bar{T}$, we obtain in the linear approximation $q_r = q_{r0} + q_{ra}\sin(\omega t + \psi)$, where $q_{r0} = \varepsilon\sigma\bar{T}^4$ and $q_{ra} = 4\varepsilon\sigma\bar{T}^3 T_a$. In order to find a relation between sample temperature (3) and the thermal flux of laser radiation at $\bar{T} \approx T_m$, let us assume that q_{r0} and q_{ra} are independent of the time. In this approximation, the problem can be solved using the method of an integral Fourier transform (see, e.g., [3]). The final expressions are rather lengthy, but, under the assumption that

$$t \geq 0.5H^2/a, \quad Hq_0/2\lambda \leq \bar{T}, \quad H^2\omega/a \ll 1, \tag{4}$$

they simplify to

$$\bar{T} = T_0 + \frac{a}{\lambda H}\left[(q_0 - 2q_{r0})t - 2\frac{q_{ra}}{\omega}\cos\psi\right],$$

$$T_a = \frac{aq_a}{\lambda H\omega\sqrt{1 + \tan^2\psi}}, \quad \tan\psi = \frac{8\varepsilon\sigma\bar{T}^3 a}{\lambda H\omega},$$

where T_0 is the temperature at which the thermal radiation is "switched on" (the process time is measured beginning with this moment). The physical meaning of the first condition in (4) consists in determining the time for which a regular regime is established, whereby the averaged (over oscillations) temperature profile in the sample cross section is formed (this profile subsequently shifts up on the temperature scale without changing in shape). The two other conditions allow this profile to be ignored: the former, for $T = \bar{T}$, and the latter, for the harmonic component. In this case, the aforementioned profile (as well as the initial condition) is insignificant for a thin plate (while being necessary for formulating these conditions).

Let the melting temperature T_m be achieved at a certain moment of time t_m on the irradiated sample surface: $T(0, t_m) = T_m$. Beginning with this moment, the plate exhibits both heating and melting, but the deposited laser energy is mostly spent on melting. Using conditions (4), one can significantly simplify the solution of the problem in the two-phase region, where heat conduction equation (1) is written for each phase. The first condition in (2) is the boundary condition to be used with Eq. (1) for the liquid phase, whereas the second condition in (2) refers to the solid phase. These conditions have to be supplemented by a condition on the moving phase boundary $x = \xi$ (Stefan's problem):

$$\lambda_s\left.\frac{\partial T_s}{\partial x}\right|_{x=\xi} - \lambda_l\left.\frac{\partial T_l}{\partial x}\right|_{x=\xi} = \rho_m\gamma\frac{d\xi}{dt},$$

where ρ_m is the latent heat of melting (subscripts "l" and "s" refer to the liquid and solid phases, respectively). For the sake of simplicity, let us neglect the difference between the metal densities in the solid and liquid states and ignore the change in the plate thickness upon melting. The initial condition corresponds to the sample temperature profile in the cross section, which is obtained for a single-phase region. For a thin plate obeying conditions (4), we assume that $T_s = T_l = T_m$ throughout the plate and ignore the energy spent for heating. Then, the velocity of propagation of the interphase boundary is described by a simple equation:

$$\rho_m\gamma d\xi/dt = q_L - 2q_r(T_m),$$

which yields

$$\xi(t) = \frac{1}{\rho_m\gamma}\Bigg\{[q_0 - 2q_r(T_m)](t - t_m)$$

$$+ \frac{q_a}{\omega}[\sin(\omega t) - \sin(\omega t_m)]\Bigg\}, \tag{5}$$

$$t_m < t < t_1.$$

Since the position of the interphase boundary (melting front) oscillates, it can return to the sample surface at a certain moment of time t_1 such that $\xi(t_1) = 0$. From this moment on, the sample again occurs in the single-phase state at a temperature $T_s \leq T_m$, which varies as described by the solution obtained above, but with a different initial condition: $T_s(t_1) = T_m$. As a result, we obtain

$$T_s(t) = T_m + \frac{a_s}{\lambda_s H}[q_0 - 2q_{r0}(\bar{T})](t - t_1)$$

$$+ T_a[\sin(\omega t + \psi) - \sin(\omega t_1 + \psi)],$$

$$t_1 < t < t_2.$$

At a certain moment of time $t = t_2$, the melting temperature is reached again and the interphase boundary moves according to Eq. (5), where t_m has to be replaced by t_2, and so on. As a result, a two-phase state observed in the time intervals $t_i < t < t_{i+1}$, where i is even, alternates with a single-phase (solid) state in the time intervals $t_i < t < t_{i+1}$, where i is odd. In the thermograms, the former intervals correspond to short segments of the constant temperature $T = T_m$, while the latter intervals correspond to the lower temperature half-waves. This alternation takes place until the averaged (over oscillations) position of the melting front will penetrate to a depth exceeding the amplitude of its oscillations. This results in a longer period of the two-phase state, which terminates when the melting front reaches the rear surface of the plate ($\xi = H$).

Beginning with this moment, the single-phase (liquid) state alternates with the two-phase state until the plate is completely melted at a certain moment of time t_M. This event can be followed by a further heating of the plate unless liquid metal flows out of the spot of laser focusing. The results of approximate calculations of the sample temperature according to the simplified analytical model with the parameters corresponding to the conditions of our experiments are presented in Fig. 2. As can be seen, the calculated curve qualitatively agrees with the experimental thermogram.

Thus, the entire melting process observed in the time interval $t_m < t < t_M$ can be subdivided into three regions. In the first region, the two-phase state alternates with the solid state; in the second region, the metal in the laser spot occurs only in the two-phase state; and in the third region, the two-phase state alternates with the liquid state. The observed quantitative discrepancy (the second region in the calculated curve is significantly more lengthy than in the experimental thermogram) is related to the fact that the theoretical model ignored thermal losses for the heat conduction in the lateral directions (according to estimates, these
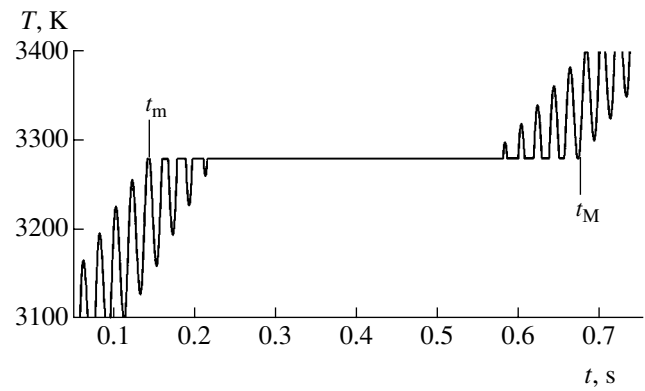

Fig. 2. The calculated time variation of the temperature of a 80-μm-thick pure tantalum foil heated by laser radiation with harmonically modulated intensity.

losses are rather significant, but they still do not change the obtained qualitative pattern).

It is possible to show that, as the phase ψ increases, the first of the three regions considered above becomes shorter, whereas the third region is extended. Under the condition that

$$\frac{2}{\pi}\sin(\psi/2) \geq \frac{q_0 - 2q_{r0}(\bar{T})}{q_a},$$

the third region theoretically (with neglect of the possibility that the melt flows out of the laser spot) can be delayed to infinity ($t_M \longrightarrow \infty$). Since ψ depends on the frequency of the laser intensity modulation, this process can be controlled. This possibility can be useful for the identification and investigation of phase transitions with low latent heats.

Conclusions. The fine structure observed in the vicinity of the melting point in the thermogram of a thin plate heated by laser radiation with a harmonically modulated intensity was theoretically described. At temperatures in the vicinity of the melting point T_m, the thermograms exhibit lower ($T < T_m$) and upper ($T > T_m$) half-waves of variable amplitudes, with intermediate short intervals corresponding to $T = T_m$. The time periods featuring the lower and upper half-waves are separated by a longer interval corresponding to a two-phase state ($T = T_m$), in which the harmonic component is completely degenerate.

The results of analytical calculations qualitatively agree with the shape of experimental thermograms in the two-phase state. This allows the method of sample heating by laser radiation with harmonically modulated intensity to be used for the identification of phase transitions with melting.

It is shown that, by changing the parameters of modulation of the intensity of the incident heat flux (laser radiation), for example, by changing the modulation frequency, it is possible to control the duration of melting of a thin metal plate.

REFERENCES

1. A. V. Kostanovskiǐ, L. B. Nefedkina, and M. E. Kostanovskaya, Teplofiz. Vys. Temp. **35**, 122 (1997).

2. A. V. Kostanovskiǐ, M. G. Zeodinov, M. E. Kostanovskaya, and D. V. Presnyakov, Pribory **23** (5), 132 (2002).

3. A. V. Lykov, *Theory of Heat Conduction* (Vysshaya Shkola, Moscow, 1967) [in Russian].

Translated by P. Pozdeev

Creating Liquid Droplets in Gas Bubbles by Means of Light Beam Controlled Capillary Convection

N. A. Ivanova* and B. A. Bezuglyĭ

Tyumen State University, Tyumen, Russia
* e-mail: nivanova@utmn.ru
Received February 24, 2005

Abstract—A new approach to obtaining liquid droplets for microfluidic devices is proposed. According to this method, a droplet with a volume of several tens of nanoliters is formed under the action of a light beam upon a film of wetting liquid surrounding an air bubble, which occurred within a thin layer of this liquid confined between two plates. The kinetics of growth of liquid droplets in air bubbles of various dimensions is studied, and the characteristic droplet size is estimated. © 2005 Pleiades Publishing, Inc.

Dosing microamounts of liquids in the form of droplets, which may contain samples of biological substances and chemical compounds, is an important operation in biochemical and microfluidic devices [1]. Investigations in this field are mainly concentrated on the elucidation of mechanisms of liquid droplet formation under the action of pressure gradients, in particular, under conditions of controlled gas injection via hydrophobic holes in the wall of a microchannel carrying a pumped liquid [2, 3] or under the action of capillary forces controlled by electric fields [4].

This Letter describes a new approach to dosing extremely small volumes of liquids and concentrating compounds in the obtained droplets. The proposed approach is based on the phenomenon of solutocapillary (SC) convection controlled by thermal action of a light beam [5]. The SC convection is observed in thin layers of multicomponent liquids absorbing light, containing a low-volatile tensoactive compound (TAC), and obeying the condition $|\sigma_T|\nabla T < \sigma_C \nabla C$, where $\sigma_T < 0$ is the temperature coefficients of surface tension, $\sigma_C > 0$ is the concentration coefficients of surface tension, ∇T is the temperature gradient, and ∇C is the concentration gradient.

The microfluidic device was modeled by an assembled optical cell of the Hele–Shaw type with a gap width of $h = 10.0 \pm 0.1$ or 50.0 ± 0.5 μm. The gap was filled with a working medium, representing a saturated iodine solution in 96% ethyl alcohol (20°C), with water playing the role of a TAC. The gas (air) bubbles in the cell were created using a method described previously [6], so that a wetting liquid film with a thickness of $\delta \ll h$ was retained between the cell wall and the bubble surface. The bubble is necessary for two reasons: (i) the presence of a free interface makes it possible to use the SC forces for inducing a liquid flow and (ii) the gas prevents the dispersion of reactants from a droplet to the surrounding solution [7].

The experiments were performed in a setup described in [6]. The light beam from a mercury lamp was focused into a spot with a diameter of $d = 0.6 \pm 0.1$ mm and a power of $P \cong 100$ mW on the surface of the absorbing liquid film under the bubble in the experimental optical cell (Fig. 1a). Heating of the liquid film is accompanied by evaporation of the volatile component at a volume rate of $Q_e \propto P_a/\rho L_e$, where P_a is the absorbed power, ρ is the liquid density, and L_e is the latent heat of vaporization. As a result, the TAC concentration in the heated region of the liquid film increases and a radial TAC concentration gradient ∇C appears, which gives rise to a surface tension gradient $\nabla\sigma = \sigma_C\nabla C$ on the film surface. This creates a centripetal SC liquid flow at a rate of Q_f toward the beam spot center,
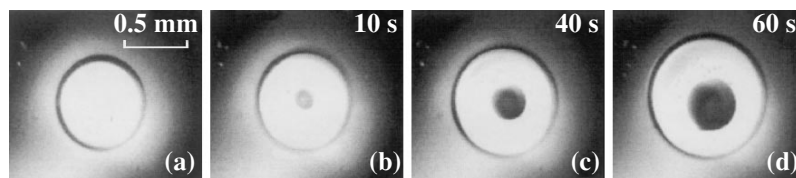
Fig. 1. Microphotographs (top view) showing the appearance and growth of a liquid droplet in a gas bubble with the initial diameter $D_0 \cong 0.7$ mm, situated in a cell with $h \cong 50$ μm filled with a saturated iodine solution in ethanol. The left shot shows the light beam switched on at $t = 0$ and presents the spatial scale.

D_d, mm
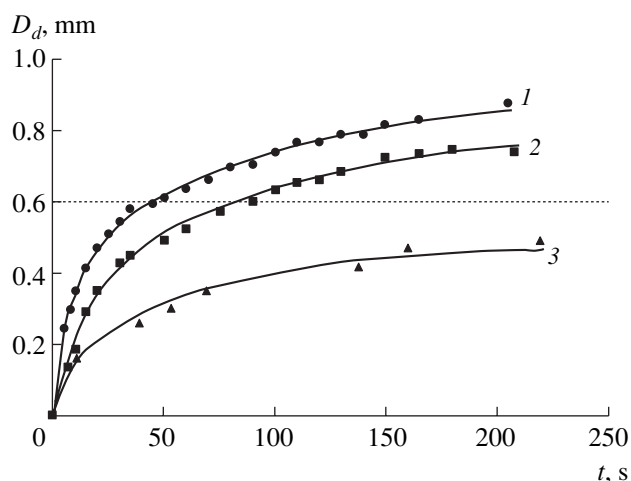
Fig. 2. Time variation of the visible diameter of a liquid droplet growing after the onset of irradiation in a gas bubble with the initial diameter $D_0 = 0.4$ (*1*), 0.6 (*2*), and >1 mm (*3*). The dashed line shows the focused light beam diameter.

which results in the formation of a liquid droplet [5], as depicted in Fig. 1b. In the course of irradiation, the supply (Q_f) of the surrounding liquid driven by $\nabla\sigma$, which is maintained due to evaporation (Q_e) of the volatile component from the droplet ($Q_e < Q_f$), provides for an increase in the droplet volume V_d and the TAC concentration in this droplet. This is manifested by visible growth in the droplet diameter (D_d), the bubble diameter (D_b), and the optical density of the droplet (Figs. 1b–1d).

If the working medium in the cell is a buffer solution containing biological cells (large molecules, etc.) with a characteristic size below δ, these inclusions will also be carried by the SC flow toward the beam spot center and, hence, accumulated in the growing droplet. To a rough approximation, the bubble can be considered as a cylinder of height h and its volume before irradiation can be estimated as $V_b(0) = \pi D_0^2 h/4$, where D_0 is the bubble diameter at $t = 0$. At an arbitrary moment of time, the volume of this bubble with a droplet inside is $V_b(t) = \pi D_b^2 h/4 = V_b(0) + V_d(t)$. Therefore, the droplet volume can be estimated using the formula $V_d(t) = \pi h(D_b^2 - D_0^2)/4$. According to this relation, the maximum possible droplet volumes, estimated for the cell thicknesses 10 and 50 μm and the bubble diameters $d/2 \leq D_0 \leq 2d$, do not exceed several tens of nanoliters for an irradiation time within $t = 1$–5 min. For example, the volumes of droplets evaluated using the micrographs in Figs. 1b and 1d are about 5 and 20 nl, respectively. These values correspond to the typical volumes of droplets used as microcontainers for reactants and microreactors in biochemical analysis [7, 8].

The droplet growth rate is determined by the response of a particular microfluidic system. In our sys-

tem, this rate (at a constant beam power P and layer thickness h) depends on D_0 and, hence, on h_0. Figure 2 shows the plots of $D_d(t)$ for the droplets growing in the bubbles with various initial diameters D_0. The rapid droplet growth in a small bubble ($D_0 \leq d$) is related to the fact that the wetting film under this bubble is thicker, while the solution boundary is closer than in the case of $D_0 > d$, which provides for a better supply of liquid to the growing drop. In bubbles with $D_0 = 0.4$–0.8 mm, a droplet appears at the center, rapidly (within $t \leq 1$ min) increases in diameter due to the supply of liquid from the periphery, and covers the entire beam projection area. Then, the droplet growth rate decreases so that its diameter increment for $t > 1$ min is less than 25% (Fig. 2, curves *1* and *2*). This is related to an increase in the rate of flow to the vapor phase ($Q_e \longrightarrow Q_f$) due to a growth in P_a and in the surface area from which the liquid is evaporated. In the bubbles with $D_0 > d$, the drop grows more slowly (because of overdrying of the thin film in the zone of irradiation) and reached a level of $D_d = d$ for a time exceeding 5 min (Fig. 2, curve *3*). Under conditions of prolonged irradiation, the droplet occurs in a stationary state ($D_d =$ const), which reflects a dynamic equilibrium between the vapor and liquid flows ($Q_e = Q_f$). This behavior was originally observed in large gas bubbles with $D_0 > 5$ mm [5].

The phenomenon of SC convection controlled by a light beam provides a contactless method for creating droplets of required volume with a controlled content of selected substances, thus offering a unique tool for manipulating liquid objects on a microscopic level.

REFERENCES

1. K. Jensen and A. Lee, Lab Chip **4**, 31 (2004).

2. T. Nisisako, T. Torii, and T. Higuchi, in *Proceedings of the Society of Instrument and Control Engineers (SICE) Conference, Osaka, 2002*, pp. 1262–1264.

3. K. Handique, B. Gogoi, M. Burns, and C. Mastrangelo, US Patent No. 6130098 (2000).

4. S. K. Cho, H. Moon, and C.-K. Kim, J. Microelectromech. Syst. **12**, 70 (2003).

5. B. A. Bezuglyĭ, Candidate's Dissertation (Moscow State University, Moscow, 1983).

6. B. A. Bezuglyĭ and N. A. Ivanova, Pis'ma Zh. Tekh. Fiz. **28** (20), 19 (2002) [Tech. Phys. Lett. **28**, 828 (2002)].

7. L. Snyder, J. Levine, R. Stroy, and A. Conetta, Anal. Chem. **48**, 942 (1976).

8. M. He, C. Sun, and D. Chiu, Anal. Chem. **76**, 1222 (2004).

Translated by P. Pozdeev

Electromechanical Properties
of Piezoelectric Ceramics–Polymer Composites
of the 0–3 Connectivity Type

V. V. Eremkin, A. E. Panich, and V. G. Smotrakov*

"Piezopribor" Research Design and Construction Bureau, Rostov State University, Rostov-on-Don, Russia
* *e-mail: smotr@ip.rsu.ru*
Received March 23, 2005

Abstract—Piezoelectric composites with 0–3 connectivity based on $Pb_{0.76}Ca_{0.24}(Co_{0.5}W_{0.5})_{0.05}Ti_{0.95}O_3$ ceramics and thermoplastic poly(vinilydene fluoride) copolymers have been obtained and characterized with respect to electromechanical properties. The hydrostatic piezoelectric voltage coefficient g_h and the figure of merit $g_h d_h$ have been determined as functions of the degree of composite filling with the ceramic powder for various polymer matrices and ceramic particle dimensions. © *2005 Pleiades Publishing, Inc.*

Piezoelectric ceramics–polymer composites of the 0–3 connectivity type, comprising a ceramic powder homogeneously dispersed in a polymer matrix, are the most widely used and relatively cheap commercial composite materials for hydroacoustic receivers. This application requires that a composite would possess the maximum possible product of the hydrostatic piezoelectric coefficients, $g_h d_h$, which is called the figure of merit. For this reason, the ceramic phase usually represents a $PbTiO_3$ based solid solution possessing highly anisotropic piezoelectric coefficients, $|d_{33}/d_{31}| \gg 1$, so that $d_h \approx d_{33}$ and $g_h \approx g_{33}$. Selection of the polymer is determined by the need for matching the permittivities of the ceramic material and the matrix so as to provide for effective polarization of the composite. This task is usually solved by using a polar dielectric polymer with a high permittivity.

We have prepared and studied a composite material based on $Pb_{0.76}Ca_{0.24}(Co_{0.5}W_{0.5})_{0.05}Ti_{0.95}O_3$ ceramics and thermoplastic fluorinated polymers of the F-2ME and F-62 commercial grades representing poly(vinilydene fluoride) copolymers (Plastpolymer company, St. Petersburg) [1]. The ceramic component has a permittivity of $\varepsilon_{33}^T/\varepsilon_0 = 200$ (which is a relatively low value for ferroelectric piezoceramic materials), a low loss tangent ($\tan\delta = 1.5\%$), a longitudinal piezoelectric coefficient of $d_{33} = 68$ pC/N, and an almost zero transverse coefficient d_{31}. The two polymers (F-2ME and F-62) possess close dielectric characteristics, including relatively high permittivities ($\varepsilon_r = 9$–10), small losses ($\tan\delta = 1.2$–2.0%), and high electric strength (21–25 kV/mm), but have significantly different elastic properties.

The initial ceramics with the base composition $Pb_{0.76}Ca_{0.24}(Co_{0.5}W_{0.5})_{0.05}Ti_{0.95}O_3$ and a 1 wt % MnO additive was obtained by the conventional two-stage solid state synthesis as described elsewhere [2]. Direct introduction of the synthesized ceramic powder (intended for sintering high-density ceramics) into a polymer matrix does not provide for obtaining a composite with high piezoelectric characteristics because the initial powder has a small particle size (~1 μm) and is not a single-phase material. Recently, we used four methods for an additional thermal treatment of the as-synthesized piezoceramic powder and studied the influence of technological factors on the crystal perfection, shape, and granulometric composition of obtained particles [3]. For this study, we selected piezoceramic fillers of two types: (i) a powder with an average particle size of ~5 μm, which was obtained by crushing and milling of porous ceramics, and (ii) a granulated powder with a maximum particle size of ~250 μm.

The samples of composite materials with a degree of the polymer matrix filling with the ceramic phase varying from 30 to 60 vol. % were prepared by molding. The mechanical mixture of a ceramic powder and a polymer was pressed into disks with a diameter of 15 mm and a height of 1 mm. For F-2ME matrix, the molding temperature was 550–590 K, the pressure was 60–90 MPa, and the time of keeping at the maximum temperature was 0.25 h. For F-62, the molding temperature was reduced to 520–540 K. Silver electrodes on the opposite edges of disks were obtained by deposition in vacuum. The samples were poled in a silicon oil bath by applying a 100–140 kV/cm electric field at a temperature of 363–393 K for a time of 0.5–2 h. The hydrostatic piezoelectric coefficients (g_h and d_h) and the figure of merit ($g_h d_h$) were calculated using data on the sample response to acoustic pressure. The measure-

g_h, 10^{-3} (V m)/N
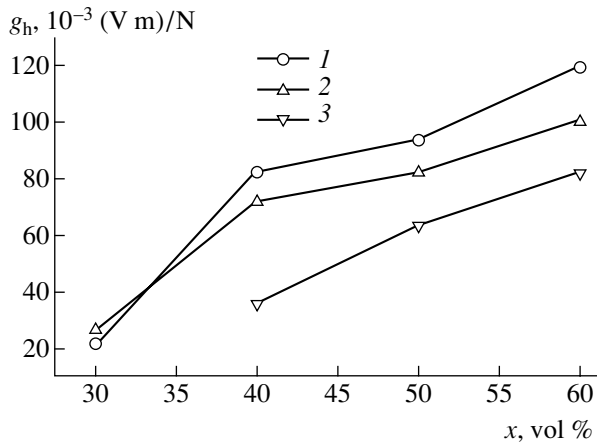
Fig. 1. Experimental plots of the hydrostatic piezoelectric voltage coefficient g_h and the figure of merit $g_h d_h$ versus the degree of composite filling with the ceramic powder for two polymer matrices and different average particle sizes: (*1*) F-62 copolymer and granulated ceramics; (*2*) F-2ME copolymer and granulated ceramics; (*3*) F-2ME copolymer and fine disperse powder.

$g_h d_h$, 10^{-15} m^2/N
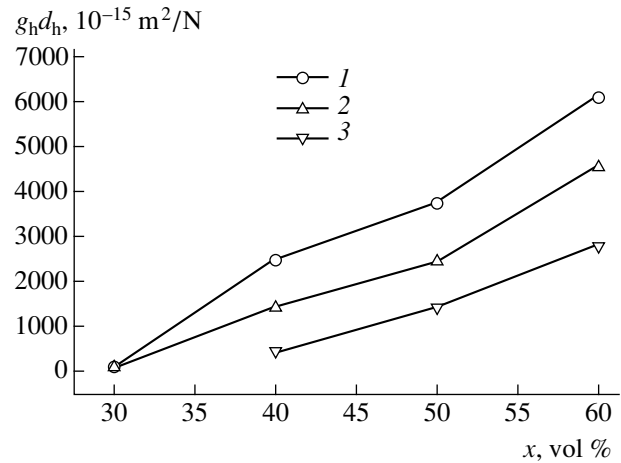
Fig. 2. Experimental plots of the figure of merit $g_h d_h$ as functions of the degree of composite filling with the ceramic powder for two polymer matrices and different average particle sizes: (*1*) F-62 copolymer and granulated ceramics; (*2*) F-2ME copolymer and granulated ceramics; (*3*) F-2ME copolymer and fine disperse powder.

ments were performed at a frequency of 125 Hz, using a Pascal-3Ts device with a small-volume air chamber.

Figures 1 and 2 show the experimental plots of the hydrostatic piezoelectric voltage coefficient g_h and the figure of merit $g_h d_h$ as functions of the degree of composite filling with the ceramic powder for the two polymer matrices and different average particle sizes. As can be seen, the maximum g_h values and figures of merit were obtained for the F-62 polymer matrix with a granulated filler: $g_h = 119.1 \times 10^{-3}$ (V m)/N and $g_h d_h = 6074 \times 10^{-15}$ m^2/N at the maximum degree of filling (60%). For the F-2ME matrix filled with a ceramic powder to the same degree, the corresponding values were 100.4×10^{-3} (V m)/N and $g_h d_h = 4588 \times 10^{-15}$ m^2/N, respectively. The obtained parameters are comparable with those of the best available commercial materials of the 0–3 piezoelectric ceramics–polymer composite type [4, 5].

The large values of piezoelectric coefficients observed for the composites based on the F-62 copolymer can be explained by the high elastic toughness of this matrix. The obtained results confirmed the known tendency of the piezoelectric coefficients to increase with the average particle size of the ceramic filler [5–8]. This trend can be related both to a higher crystal perfec-

tion of the granulated ceramic material and to a lower specific area of polymer–ceramics interfaces (i.e., a lower screening action of charges accumulated at such boundaries).

REFERENCES

1. http://plastpolymer.h1.ru/tpfp.htm.
2. V. G. Smotrakov, V. V. Eremkin, V. A. Doroshenko, *et al.*, Neorg. Mater. **30**, 241 (1994).
3. V. G. Smotrakov, V. V. Eremkin, A. E. Panich, *et al.*, Neorg. Mater. **40**, 890 (2004).
4. K. Han, A. Safari, and R. E. Riman, J. Am. Ceram. Soc. **74**, 1699 (1991).
5. C. Gui, R. H. Baughman, Z. Iqbal, *et al.*, Sens. Actuators A **65**, 76 (1998).
6. J. Mendiola, B. Jimenez, C. Alemany, and E. Maurer, Ferroelectrics **39**, 1201 (1981).
7. R. P. Tandon, N. Narayana Swami, and N. C. Soni, Ferroelectrics **156**, 61 (1994).
8. G. Rujijanagul, S. Boonyakul, and T. Tunkasiri, J. Mater. Sci. Lett. **20**, 1943 (2001).

Translated by P. Pozdeev

Carbon Nanotubes: A New Type of Emitter in the Terahertz Range

O. V. Kibis[a],* and M. E. Portnoi[b]

[a] Novosibirsk State Technical University, Novosibirsk, 630092 Russia
[b] School of Physics, University of Exeter, Exeter EX4 4QL, United Kingdom
* e-mail: Oleg.Kibis@nstu.ru
Received April 6, 2005

Abstract—It is theoretically demonstrated that the electric-field-induced heating of the electron gas in carbon nanotubes can lead to population inversion in the electron subbands, which results in the generation of electromagnetic waves in the terahertz range by hot electrons. This phenomenon can be used for the creation of radiators of a new type, based on carbon nanotubes, for the terahertz frequency range. © 2005 Pleiades Publishing, Inc.

Carbon nanotubes (CNTs) are cylindrical molecules with nanometer diameter and micron length [1]. This unusual combination of transverse and longitudinal dimensions accounts for the unique electronic properties of CNTs and makes them promising materials, in particular, for the creation of novel nanoelectronic devices. These prospects explain the considerable activity of researchers in investigations of the properties of CNTs in the past decade. Below, we will consider for the first time some features of the energy spectrum of CNTs under the conditions of energy pumping via the electric-field-induced heating of the electron gas, which can be used for the creation of radiators operating in the terahertz frequency range.

The electron states in CNTs can be classified in terms of two quantum numbers: (i) an integer angular momentum l, which characterizes the rotation of the electron about the nanotube axis, and (ii) a continuous electron wavenumber k, which characterizes the translational motion of the electron along the nanotube axis. In these terms, the energy spectrum of electrons in a CNT of arbitrary crystallographic structure (n, m) $(m \neq 0)$ is described by the equation [2]

$$\varepsilon_l(k) = \pm\gamma_0\left[1 + 4\cos\left(\frac{k_s a}{2}\right)\cos\left(\frac{2n+m}{2m}k_s a - \frac{2\pi l}{m}\right) + 4\cos^2\left(\frac{k_s a}{2}\right)\right]^{1/2}, \quad (1)$$

where

$$k_s = \frac{\pi l}{a}\frac{2n+m}{n^2+m^2+nm} + k\frac{\sqrt{3}m}{2\sqrt{n^2+m^2+nm}},$$

$$l = 0, 1, 2, \ldots, \quad \frac{2(n^2+m^2+nm)}{d_R} - 1,$$

the signs ± refer to two branches of the electron energy spectrum (corresponding to the conduction and valence bands), $\gamma_0 \approx 3$ eV is the overlap integral between the π orbitals of the nearest neighbor carbon atoms in the graphene sheet, $a = \sqrt{3} \times a_{c-c} = 2.46$ Å, $a_{c-c} = 1.42$ Å is the interatomic distance in graphene, and the number d_R is the greatest common divisor of two integers $(2n + m)$ and $(2m + n)$. Here, (n, m) is the pair of integers defining the CNT crystallographic type according to the conventional notation [1, 2].

According to Eq. (1), the electron energy spectrum of a CNT comprises a set of subbands $\varepsilon_l(k)$ with different angular momenta l. Equation (1) also shows that there are certain wavenumbers k where there are intersections between the electron subbands with l values differing by unity, for which dipole electron transitions accompanied by the radiation of electromagnetic waves are allowed. It is important that this crossing offers a possibility to provide conditions for the generation of electromagnetic radiation by heating the electron gas in a longitudinal electric field oriented along the CNT axis. Let us consider this situation in more detail in a particular case of CNTs with a crystallographic structure of the (n, n) type.

The (n, n) CNTs having the so-called armchair configuration [1] always exhibit electric conductivity of the metallic type. Putting $m = n$ in Eq. (1), we obtain the following expression for the electron energy spectrum in the (n, n) CNT:

$$\varepsilon_l(k) = \pm\gamma_0\left[1 + 4\cos\left(\frac{\pi l}{n}\right)\cos\left(\frac{ka}{2}\right) + 4\cos^2\left(\frac{ka}{2}\right)\right]^{1/2}, \quad (2)$$

where $l = 0, 1, 2, \ldots, 2n - 1$. An analysis of this expression shows that the ground electron state in the conduction band of the (n, n) CNT corresponds to a subband with $l = n$. Thus, the phenomenon of interest can be ana-
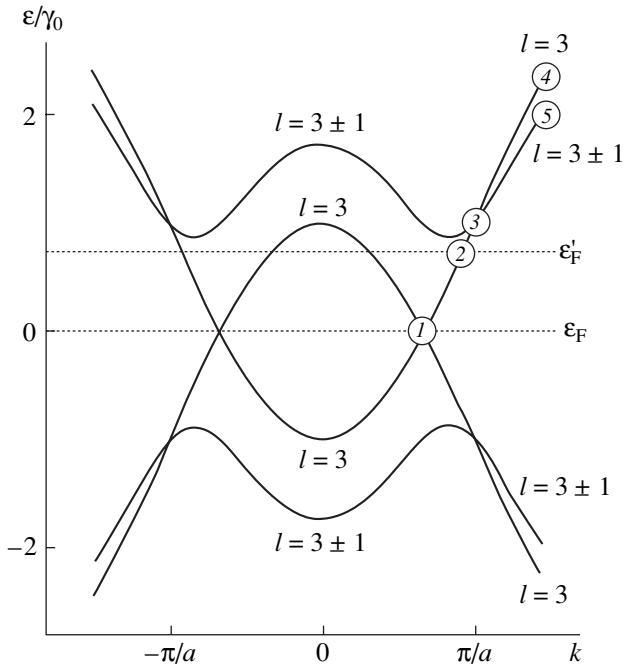
A fragment of the electron energy spectrum of a (3, 3) CNT (see the text for explanations).

lyzed by restricting our consideration to the subbands with $l = n$ and $l = n \pm 1$.

The energy spectrum of these subbands is presented in the figure, which shows a scheme of the expanded Brillouin zone for the particular (3, 3) CNT. Let an electric field be applied along the CNT axis. Under the action of this field, the energy of an electron which is initially on the Fermi level ε_F (state 1 in the subband with $l = 3$) will increase, and the electron will move in the k space. Since the field oriented along the CNT axis cannot change the angular momentum l of the electron, this motion proceeds along the branch with $l = 3$ via the chain of states $1 \longrightarrow 2 \longrightarrow 3 \longrightarrow 4$, where state 3 corresponds to the intersection of subband $l = 3$ and the degenerate subbands with $l = 2$ and $l = 4$ (denoted in the figure by $l = 3 \pm 1$). The electron passing via state 3 creates the inverse population: high-energy state 4 in the subband $l = 3$ is occupied, while the low-energy state 5 in the subband $l = 3 \pm 1$ is vacant. Apparently, this inversion leads to the generation of electromagnetic waves corresponding to optical transitions from state 4 to state 5.

The position of the Fermi level in nanotubes can be varied within broad limits, for example, by applying a transverse electric field (gate field in carbon-nanotube field-effect transistors [3]) or by injecting charge carriers from specially selected metal contacts into CNTs [4]. Upon increasing the Fermi energy from ε_F to a level

(ε_F', see figure) sufficiently close to the energy of state 3, it is possible to observe the effect described above even for very (arbitrarily) low-heating longitudinal electric fields. In this context, it should be noted that heating of the electron gas is much more readily provided in CNTs than in conventional semiconductor structures because the electron mean free path for elastic scattering in CNTs is very large and reaches about one micron even at room temperature [5, 6].

The main factor hindering the electron gas heating in CNTs is inelastic scattering, which is accompanied by the emission of high-energy (~0.2 eV) phonons [5, 6]. Therefore, in order to ensure the optimum conditions for the observation of the effects described above, it is necessary to increase the Fermi energy by one of the possible means [3, 4] so that the energy difference between the point of intersection of the subbands (state 3) and the electron energy on the modified Fermi level ε_F' (state 2) would be smaller than the characteristic phonon energy (0.2 eV). This characteristic energy also limits the maximum energy of a photon emitted upon the optical transition from state 4 to state 5. The photon energy of $\hbar\nu = 0.2$ eV corresponds to an electromagnetic wave frequency of about 50 THz. This implies that the phenomenon under consideration can lead to the radiation of electromagnetic waves in a broad range up to terahertz frequencies. This is an important circumstance from the standpoint of possible technical applications, because the development of terahertz radiators is among the most important tasks in modern applied physics [7].

REFERENCES

1. R. Saito, G. Dresselhaus, and M. S. Dresselhaus, *Physical Properties of Carbon Nanotubes* (Imperial College Press, London, 1998).
2. O. V. Kibis, D. G. W. Parfitt, and M. E. Portnoi, Phys. Rev. B **71**, 035411 (2005).
3. J. Appenzeller, J. Knoch, V. Derycke, *et al.*, Phys. Rev. Lett. **89**, 126801 (2002).
4. J. A. Misewich, R. Martel, Ph. Avouris, *et al.*, Science **300**, 783 (2003).
5. J.-Y. Park, S. Rosenblatt, Y. Yaish, *et al.*, Nano Lett. **4**, 517 (2004).
6. A. Javey, J. Guo, M. Paulsson, *et al.*, Phys. Rev. Lett. **92**, 106804 (2004).
7. G. Davies and E. Linfield, Phys. World **17** (4), 37 (2004).

Translated by P. Pozdeev

Electric-Field-Induced Shift of the Magnetic Resonance Line in Ferrite–Piezoelectric Composites

O. V. Antonenkov[a], M. I. Bichurin[a], D. A. Filippov[a],*

V. M. Petrov[a], and G. Srinivasan[b]

[a] *Novgorod State University, Velikiĭ Novgorod, Russia*
[b] *Physics Department, Oakland University, Rochester, Michigan 48309, USA*
* e-mail: fdma@novsu.ac.ru
Received March 23, 2005

Abstract—The electric-field-induced shift of the magnetic resonance line in ferrite–piezoelectric composites has been studied by experimental and theoretical methods. Expressions for the resonance line shift as a function of the field strength and structural parameters are obtained. The shift depends linearly on the field strength and increases with the content of a piezoelectric component in the composite. The results of calculations for a lithium ferrite spinel–lead zirconate titanate composite are in good agreement with the experimental data obtained for this material. © 2005 Pleiades Publishing, Inc.

Composite materials, comprising mechanical mixtures of magnetic and piezoelectric components prepared using the standard ceramic technology, exhibit a magnetoelectric (ME) effect, whereby a polarization appears in a sample under the action of a magnetic field and, vice versa, magnetization appears upon the application of an electric field. In single crystal ME materials, this phenomenon is primarily related to the spin–orbit interaction, while other contributions are relatively small. In contrast, the nature of the ME effect in composites is primarily due to a mechanical interaction between the ferrite and piezoelectric components. Since this phenomenon is manifested neither in the ferrite nor in the piezoelectric phase separately, the ME effect observed in composites is treated as secondary.

Application of an electric field to a material featuring the ME effect gives rise to mechanical stresses in the piezoelectric phase, which are transferred to the magnetic phase and which induce, via magnetostriction, a change in the magnetic moment that leads to a shift in the magnetic resonance line. Single crystal materials are characterized by low values of the ME coefficients. This circumstance hinders use of the ME effect in technological applications. Therefore, it is expedient to seek and study new composite materials based on piezoelectric and magnetostrictive components, in which the ME effect is much more pronounced.

Model and basic equations. As a model system (Fig. 1), we consider a bilayer ferrite–piezoelectric composite material in the form of a disk of radius R, comprising a ferrite layer of cubic ($m3m$) symmetry in mechanical contact with a piezoelectric layer of ∞m symmetry relative to the polarization axis. The thickness of the magnetic (^mh) and piezoelectric (^ph) layers (and, hence, the total disk thickness) are assumed to be much smaller than the disk radius: ^mh, $^ph \ll R$. The external surfaces of both layers bear metal electrodes of a negligibly small thickness. Let the piezoelectric be polarized along the normal to the planes of contacts (i.e., in the direction parallel to the Z axis in Fig. 1). We assume that the polarization direction coincides with the [111] of the magnetostrictive phase and consider the longitudinal ME effect, whereby both constant (bias) and alternating magnetic fields are oriented in the polarization direction.

We also assume that the disk edge faces are free, so that the normal components of the mechanical stress tensor on these surfaces are zero. For a thin disk, the
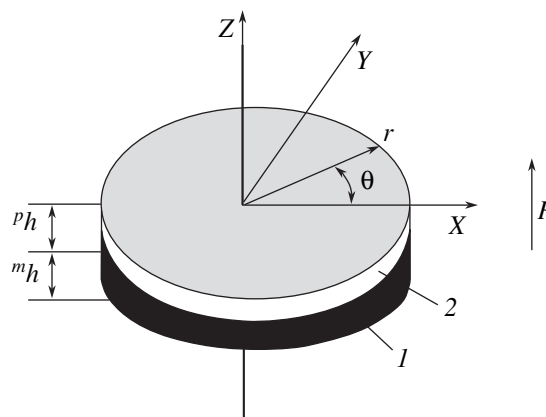
Fig. 1. Schematic diagram of the composite structure consisting of (*1*) ferromagnetic and (*2*) piezoelectric layers (see the text for explanations).
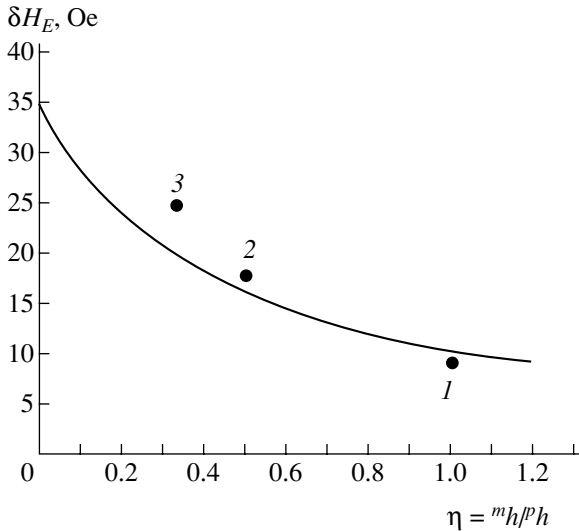
Fig. 2. A plot of the shift of the magnetic resonance line versus the relative thickness ^ph of PZT layers in a composite comprising 16 layers of lithium ferrite spinel ($Li_{0.4}Zn_{0.2}Fe_{2.4}O_4$) with $^mh = 38$ μm and fifteen PZT layers of variable thickness. The electric field strength was 22 kV/cm. Solid lines show the results of theoretical calculations; points represent the experimental data.

stress tensor component T_3 can be considered approximately equal to zero not only on the surface but in the entire disk volume as well. Since the top and bottom faces of the disk are equipotential surfaces, only the z projection of the electric field strength vector is nonzero.

Under the above assumptions, equations for the strain tensor ^mS_i in the magnetic layer and for the strain tensor ^pS_i in the piezoelectric layer can be written as

$$
\begin{aligned}
^mS_1 &= s_{11}{}^mT_1 + s_{12}{}^mT_2, \\
^mS_2 &= s_{12}{}^mT_1 + s_{22}{}^mT_2, \\
^pS_1 &= s_{11}{}^pT_1 + s_{12}{}^pT_2 + d_{31}E_3, \\
^pS_2 &= s_{12}{}^pT_1 + s_{22}{}^pT_2 + d_{31}E_3,
\end{aligned}
\tag{1}
$$

where $^ms_{ij}$ and $^ps_{ij}$ are the components of the compliance tensors of the magnetic and piezoelectric phases, respectively; d_{ij} are the piezoelectric coefficients; and E_3 is the z projection of the electric field vector.

Taking into account the symmetry of the problem and passing to a cylindrical coordinate system using well-known relations [1], we obtain the following equation for the radial displacements in the disk:

$$
\frac{\partial^2 u_r}{\partial r^2} + \frac{1}{r}\frac{\partial u_r}{\partial r} - \frac{u_r}{r^2} = 0.
\tag{2}
$$

The general solution of Eq. (2) has the following form:

$$
u_r = c_1 r + c_2/r,
\tag{3}
$$

where c_1 and c_2 are the integration constants determined from the boundary conditions. At $r = 0$ (disk center), the displacement is zero and $^mu(r) = {}^pu(r) = 0$. For the free side surface of the disk ($r = R$), the condition of equilibrium yields $^mT_{rr}{}^mh + {}^pT_{rr}{}^ph = 0$. At the ferrite–piezoelectric phase boundary, we have $^mS_{rr} = k{}^pS_{rr}$, where $k = 0$–1 is a coefficient taking into account the nonideal character of the mechanical contact at the interface in the general case.

Substituting the c_1 and c_2 values determined from the boundary conditions into formula (3) and expressing components of the stress tensor through components of the strain tensor, we eventually obtain the following relations:

$$
\begin{aligned}
^mT_{rr} &= \frac{k}{^ms_{11}(1 - {}^m\nu) + k\eta{}^ps_{11}(1 - {}^p\nu)}d_{31}E_3, \\
^mT_{\theta\theta} &= \frac{k}{^ms_{11}(1 - {}^m\nu) + k\eta{}^ps_{11}(1 - {}^p\nu)}d_{31}E_3,
\end{aligned}
\tag{4}
$$

where $^m\nu = -{}^ms_{12}/{}^ms_{11}$ and $^p\nu = -{}^ps_{12}/{}^ps_{11}$ are Poisson's coefficient for the magnetic and piezoelectric phases, respectively, and $\eta = {}^mh/{}^ph$ is the ratio of thicknesses of the ferromagnetic and piezoelectric layers.

Mechanical stresses lead to a change in the magnetization of the ferrite phase, which is manifested by a shift of the magnetic resonance line. Let us consider the case when the magnetic field is applied in the (111) plane and parallel to the [011] direction. Then, the electric-field-induced shift of the magnetic resonance line is given by the expression

$$
\begin{aligned}
\delta H_E &= \frac{(^mT_{rr} + {}^mT_{\theta\theta})\lambda_{100}}{4M_0} \\
&= \frac{1}{2M_0}\frac{k\lambda_{100}}{^ms_{11}(1 - {}^m\nu) + k\eta{}^ps_{11}(1 - {}^p\nu)}d_{31}E_3,
\end{aligned}
\tag{5}
$$

where M_0 is the saturation magnetization and λ_{100} is the magnetostriction constant.

Experiment. The ME effect was experimentally investigated at 9.3 GHz by a resonance technique with double magnetic modulation. The samples of various ferrite–piezoelectric composites had the form of disks with a diameter of 3–5 mm and a total thickness of 0.25–0.5 mm. The samples had different numbers and thicknesses of alternating magnetic and piezoelectric layers. The sample response was excited by applying rectangular voltage pulses with an amplitude of 5 kV.

Figure 2 shows a plot of the shift of the magnetic resonance line versus the relative thickness of PZT layers in a composite comprising 16 layers of lithium ferrite spinel $Li_{0.4}Zn_{0.2}Fe_{2.4}O_4$ (LFO) with $^mh = 38$ μm and fifteen layers of lead zirconate titanate (PZT) of variable thickness ^ph. The shift was also calculated using formula (3) with the following parameters [2]. For LFO: $^ms_{11} = 6.84 \times 10^{-12}$ m²/N, $^ms_{12} = -2.46 \times 10^{-12}$ m²/N, $4\pi M_0 = 3600$ G; for PZT: $^ps_{11} = 15.3 \times 10^{-12}$ m²/N, $^ps_{12} = -5 \times 10^{-12}$ m²/N, $^pd_{31} = -175 \times 10^{-12}$ m/V; for LFO–PZT: $\lambda_{100} = 23 \times 10^{-6}$. As can be seen, the calculated curve well agrees with the experimental data.

According to formula (5), the resonance line shift is linear with respect to the field strength and grows with increasing percentage content of piezoelectric phase (PZT) in the composite, that is, with decreasing $\eta = {}^mh/{}^ph$. The obtained results show that, in order to obtain the most pronounced ME effect, it is necessary to use a piezoelectric component with a maximum possible piezoelectric coefficient and a magnetostrictive component with a small saturation magnetization and a high magnetostriction.

REFERENCES

1. W. P. Mazon, Phys. Rev. **74**, 1134 (1948).

2. M. I. Bichurin, V. M. Petrov, Yu. V. Kiliba, *et al.*, Phys. Rev. B **66**, 134404 (2002).

Translated by P. Pozdeev

Calculation of the Parameters of Polymolecular Complexes-Precursors in the Process of Associate Formation

N. M. Blashenkov and G. Ya. Lavrent'ev

Ioffe Physicotechnical Institute, Russian Academy of Sciences, St. Petersburg, 194021 Russia
Received February 1, 2005

Abstract—The parameters of a polymolecular complex $(M + H)^+$ responsible for the formation of $M + H$ associates, where M is a molecule (e.g., ethylamine or diethylamine) and H is a hydrogen atom, have been calculated using experimental temperature dependences of the ion currents of associated ions $(M + H)^+$, assuming that these ions are formed according to the surface ionization mechanism. The parameters of the calculation include the number N of molecules in the complex under consideration, the activation energy for the surface dissociation of this complex, and the number of the effective degrees of freedom in the complex. © 2005 Pleiades Publishing, Inc.

Mechanisms responsible for the fragmentation of initial molecules or their associates (in the case of monomolecular reactions) via the stage of polymolecular complex formation are taken into consideration when the number b of the effective degrees of freedom in the complex (determined from the dome-shaped temperature dependences of the desorbed ion currents) is significantly greater than the total number s of the degrees of freedom of the given molecule [1]. Physically, a situation in which the number of the effective degrees of freedom exceeds s is realized due to the numerous bonds of said polymolecular complex, which are involved in the association process.

Previously, a general approach to the description of the monomolecular decay of a fragment of the polymolecular complex $M_N = M_1 + \ldots M^N$ was developed and an expression for the rate constant of the decay of this polymolecular complex in the gas phase was obtained [1]:

$$k_N = \frac{\kappa T Q^*_{1,2,\ldots,N}}{h Q_A^N} e^{-\frac{E}{\kappa T}}$$

$$= \frac{g^* \dfrac{\kappa T}{h} \left(\dfrac{2\pi\mu^*\kappa T}{h^3}\right)^{3/2} \dfrac{8\pi^2 (8\pi^3 I_x^* I_y^* I_z^*)^{1/2}(\kappa T)^{3/2}}{\sigma^* h^3} \prod\limits_{i=1}^{3Nn-7}\left[1 - \exp\left(-\dfrac{h\nu_i^*}{\kappa T}\right)\right]^{-1}}{g_A^N \left(\dfrac{2\pi m_A \kappa T}{h^3}\right)^{\frac{3}{2}N} \left[\dfrac{8\pi^2(8\pi^3 I_x I_y I_z)^{1/2}(\kappa T)^{3/2}}{\sigma_A h^3}\right]^N \left[\prod\limits_{i=1}^{3n-6}\left[1-\exp\left(-\dfrac{h\nu_i}{\kappa T}\right)\right]^{-1}\right]^N} e^{-\frac{E_N}{\kappa T}}. \tag{1}$$

Here, m_A is the mass of the given molecule M; $\mu^* = m_A$ is the reduced mass; N is the number of molecules M in the complex M_N; n is the number of atoms in the molecule M; I_x^*, I_y^*, I_z^*, I_x, I_y, and I_z are the principal moments of inertias of the activated complex (*) and the component molecules, respectively; Q^* and Q_A are the partition functions; σ^* and σ_A are the symmetry factors; ν^* and ν_i are the oscillation frequencies; g^* and g_A are the electron multiplicities; and E_N is the activation energy for the decay of the complex.

In the context of this study, it is most interesting to study the decay of such complexes on the surface. The number of the degrees of freedom of complexes and molecules adsorbed on the surface is lower than the analogous number in the gas phase. Indeed, rotation of the complex on the surface is hindered, and two (of the three) translational degrees of freedom are retained.

Separate molecules, which combine so as to form a complex, also possess two translational degrees of freedom and can rotate around the adsorption bond. Retaining in Eq. (1) only dimensional factors corresponding to the existing degrees of freedom of the molecules and the complex on the surface, we obtain

$$k_N = \frac{\kappa T Q_{1,2,\ldots,N}^*}{h Q_A^N} e^{-\frac{E}{\kappa T}}$$

$$= \frac{g^* \dfrac{\kappa T}{h} \left(\dfrac{2\pi\mu^*\kappa T}{h^2} \right)^{3Nn-7} \displaystyle\prod_{i=1}^{} \left[1 - \exp\left(-\dfrac{h\nu_i^*}{\kappa T} \right) \right]^{-1}}{g_A^N \left(\dfrac{2\pi m_A \kappa T}{h^2} \right)^N \left[\dfrac{16\pi^2 I_z^{1/2}(\kappa T)^{1/2}}{\sigma_A h} \right]^N \left[\displaystyle\prod_{i=1}^{3n-6} \left[1 - \exp\left(-\dfrac{h\nu_i}{\kappa T} \right) \right]^{-1} \right]^N} e^{-\frac{E_N}{\kappa T}}.$$

Separating the multipliers dependent on the temperature from the temperature-independent ones and denoting the latter by G, we can rewrite the last equation in the following form:

$$k_N = G \frac{\kappa T^2}{(\kappa T)^{\frac{3N}{2}}} \frac{\displaystyle\prod_{i=1}^{3Nn-7} \left[1 - \exp\left(-\dfrac{h\nu^*}{\kappa T} \right) \right]^{-1}}{\left(\displaystyle\prod_{i=1}^{3n-6} \left[1 - \exp\left(-\dfrac{h\nu_i}{\kappa T} \right) \right]^{-1} \right)^N} e^{-\frac{E_N}{\kappa T}}.$$

The temperature dependence of k_N is mostly determined by the second term. In order to obtain a qualitative result for the region of relatively low temperatures, where $h\nu^* \gg \kappa T$ and $h\nu_i \gg \kappa T$, we can omit the ratio of vibrational components because $1 - \exp(-h\nu/\kappa T) \approx 1$. Then, the expression for k_N simplifies to

$$k_N \approx G\left(\frac{1}{\kappa T} \right)^{\frac{3N-4}{2}} e^{-\frac{E_N}{\kappa T}}.$$

Now let us consider the monomolecular decay of a separate fragment of the polymolecular complex. Such decay for a single molecule is described using the rate constant k_0 expressed as [2]

$$k_0 \approx A\left(\frac{E}{\kappa T} \right)^b e^{-\frac{E}{\kappa T}},$$

where E is the activation energy for the decay of the fragment and b is the number of the effective degrees of freedom.

It can be shown that, during the monomolecular decay of a separate fragment of the polymolecular complex, the temperature dependence of the rate constant k_0 of the monomolecular reaction is enhanced because of the temperature dependence of k_N. The physical meaning of this statement consists in that a polymolecular complex accumulates a considerable energy on its numerous bonds, which can be statistically redistributed so as to concentrate in a separate fragment. This event can lead to the decay of the polymolecular complex (k_N) and to the monomolecular decay of the given separate fragment (k_0). Since the primary stage is related to processes in the polymolecular complex, the corresponding reaction rate constant (with its temperature dependence) will enter as a base into the power function of the preexponential term of the rate constant k_0 of the monomolecular reaction. Eventually, the rate constant of the monomolecular decay of a separate fragment in the polymolecular complex will be expressed as

$$k_0^N \approx C\left[\left(\frac{1}{\kappa t} \right)^{\frac{3N-4}{2}} e^{-\frac{E_N}{\kappa T}} \right]^b e^{-\frac{E}{\kappa T}}.$$

As can be seen from this expression, each effective degree of freedom involves a certain probability of decay of the entire complex with the energy accumulated on its numerous bonds.

During the surface ionization (SI) of polyatomic molecules, the measured current j_i is determined by the effective flow g_i of radicals [5] and by the SI coefficient β_i for these radicals: $j_i = eg_i\beta_i$. This effective flow can also be described in terms of the surface concentration of particles n and the monomolecular rate constant k_0: $g_i = k_0 n$. The surface concentration of particles is conveniently expressed via the particle flow to the surface using the well-known formula of the kinetic theory of the ideal gas: $g = n_g \sqrt{(\kappa T_g/2\pi m)}$, where n_g and T_g are the gas phase parameters. In a stationary regime, the surface concentration of particles attains a certain value n such that the outgoing flow is equal to the incoming flow g. In this case, the current of ions of

Intensity, a.u.
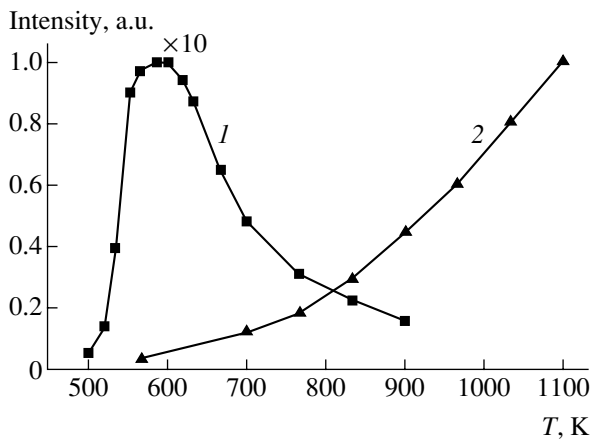
Fig. 1. The temperature dependence of the ion current for (*1*) associated ions $(M + H)^+$ and (*2*) dissociated ions $(M - H)^+$ of ethylamine.

Intensity, a.u.
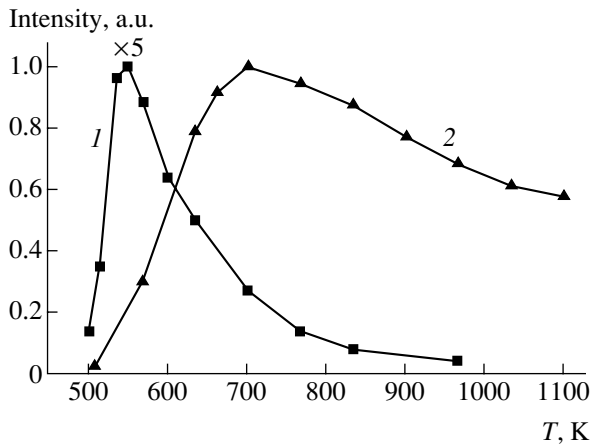
Fig. 2. The temperature dependence of the ion current for (*1*) associated ions $(M + H)^+$ and (*2*) dissociated ions $(M - H)^+$ of diethylamine.

the products of monomolecular decay of a single molecule in the case of $\beta_i = \alpha_i \ll 1$ can be expressed (omitting the subscript "i") as

$$ j = ek_0 n\beta = egB\left(\frac{E}{\kappa T}\right)^b \exp\frac{\Pi - E}{\kappa T}, \qquad (2) $$

where $\Pi = e(\varphi + \sqrt{eF - V})$ is the SI term [3], α is the SI degree, $e\varphi$ is the surface work function, eV is the ionization potential of the radical, and F is the electric field strength at the emitter surface. The case of $\alpha \ll 1$ is realized provided that $-\Pi \gg \kappa T$. Formula (2) describes the SI of dissociated ions $(M-H)^+$, for example, the ions of diethylamine and other polyatomic molecules [3, 4].

Proceeding with the description of the decay of a fragment of the heterogeneous polymolecular com-

plex, we obtain

$$ j_N = ek_0^N n\beta \cong egD\left[\left(\frac{1}{\kappa T}\right)^{(3N-4)/2} e^{-\frac{E_N}{\kappa T}}\right]^b \exp\frac{\Pi - E}{\kappa T} $$

$$ = egD\left(\frac{1}{\kappa T}\right)^{(3N-4)b/2} \exp\frac{\Pi - E - bE_N}{\kappa T}. $$

By analogy with the case of the monomolecular decay of a single molecule, expressions for determining the quantities $b^* = b(3N - 4)/2$, which is analogous to the b value in Eq. (2), and V from the experimental values of T_m (the temperature position of the maximum of the dome-shaped curve) and T_1 (the temperature of the bending point) on the $j_N(T, F)$ curve can be obtained using the condition of zero values of the first and second derivatives of $j_N(T, F)$ with respect to $1/\kappa T$ [3]:

$$ b^*\kappa T_m = eV + bE_N + E - e\varphi - e\sqrt{(eF)}, \qquad (3) $$

$$ b^* = (T_m/T_1 - 1)^{-2} = b(3N - 4)/2. \qquad (4) $$

The values of φ and F can also be determined from experimental data. In this case, the b value is in fact a fitting parameter, since it is calculated using an empirical rule. According to this rule, b amounts to 1/5 to 1/3 of the total number of the degrees of freedom s of the particle under consideration [2]. Then, the N value can be determined to within $\pm(10-15)\%$. Unfortunately, the values of E, E_N, and V are not determined independently. In the order of magnitude, the E value is comparable with the activation energy determined previously for the M–H surface dissociation reaction [3]. Once the ionization potential for the particle is known, the E_N value can be calculated using Eq. (3). If this potential is unknown, the parameters of the polymolecular complex (E_N, V) can be determined only to within $\sim20\%$, since the ionization potentials for substances belonging to certain classes usually spread within $\pm(1.5-2)$ eV.

Let us consider the temperature dependence of the current of associated ions $(M + H)^+$ of ethylamine on tungsten presented in Fig. 1 [5]. Determining the T_1 and T_m values from the experimental temperature dependence, we use formula (4) to obtain $b^* = 118$ and, hence, $b^*\kappa T_m = 5.85$ eV. The number of atoms in the molecule of ethylamine $C_2H_5NH_2$ is $n = 10$, which yields $s = 24$ and $b = 6-8$. The ionization potential for ethylamine is 7.8 eV, and the surface work function of oxidized tungsten is 6.5–6.8 eV. Proceeding from these data and using formula (3), we can determine E_N, whose average value amounts to ~0.65 eV. Then, according to formula (4), the N value for the polymolecular complex in the system under consideration is $N = 13 \pm 1$.

Now let us consider the temperature dependence of the current of associated ions $(M + H)^+$ of diethylamine

on tungsten presented in Fig. 2 [5]. Here, we obtain $b* = 217$ and $b*\kappa T_m = 10.85$ eV. The number of atoms in the molecule of diethylamine $(C_2H_5)_2NH$ is $n = 16$, which yields $s = 42$ and $b = 13–18$. Since $b*$ is very large, we assumed that the number of the effective degrees of freedom for this molecule exceeds that established according to the empirical rule and used the extreme value of $s/3 = 14$. The ionization potential for diethylamine is $eV = 7.2$ eV, and the work function of oxidized tungsten surface is 6.5–6.8 eV. Proceeding from these data and using formula (3) and (4), we obtain on the average $E_N = 0.8$ eV and $N = 14 \pm 2$. Here, the error is determined by the scatter of the parameter b.

It is interesting to note that, despite a considerable difference between the $b*$ values for the SI of $(M + H)$ associates of ethylamine and diethylamine, the numbers of molecules forming a polymolecular complex for these two molecules virtually coincide and are equal to the factor of hexagonal close packing $(6n + 1) = N$ for $n = 2$.

It should also be recalled that, as was demonstrated in [6], the process of fragment separation during the monomolecular decay of a polymolecular complex proceeds according to a second-order reaction. The reaction order experimentally determined for the associated ions in [7] was also equal to two, whereas the process of dissociated ion formation follows the first reaction order.

REFERENCES

1. G. Ya. Lavrent'ev, Zh. Tekh. Fiz. **71** (10), 120 (2001) [Tech. Phys. **46**, 1322 (2001)].

2. V. N. Kondrat'ev and E. E. Nikitin, *Kinetics and Mechanism of Vapor-Phase Reactions* (Nauka, Moscow, 1974) [in Russian].

3. É. Ya. Zandberg and N. I. Ionov, *Surface Ionization* (Nauka, Moscow, 1969; Israel Program for Scientific Translations, Jerusalem, 1971).

4. N. M. Blashenkov, N. I. Ionov, and G. Ya. Lavrent'ev, Teor. Éksp. Khim. **24**, 62 (1988).

5. U. Kh. Rasulev, Doctoral Dissertation (Leningrad, 1979).

6. G. Ya. Lavrent'ev, Pis'ma Zh. Tekh. Fiz. **27** (10), 52 (2001) [Tech. Phys. Lett. **27**, 419 (2001)].

7. E. Ya. Zandberg and U. Kh. Rasulev, Dokl. Akad. Nauk SSSR **187**, 777 (1969) [Sov. Phys. Dokl. **14**, 769 (1969)].

Translated by P. Pozdeev

The Effect of Fluctuations on a Single-Contact Interferometer: Quantum Considerations

I. N. Askerzade

Institute of Physics, National Academy of Sciences of Azerbaijan, Baku, Azerbaijan
Department of Physics, Ankara University, 06100 Tangodan, Ankara, Turkey
e-mail: solstphs@physics.ab.az; iasker@science.ankara.edu.tr
Received February 28, 2005

Abstract—The effect of quantum fluctuations on a single-contact interferometer is considered. An expression for the "fluctuational" inductance, above which the superconducting current is effectively suppressed by quantum fluctuations, is obtained. © *2005 Pleiades Publishing, Inc.*

In recent years, much attention has been devoted to the quantum effects in microscopic Josephson junctions [1–3]. One example is offered by the single-contact interferometer, which is used as a highly sensitive magnetic flux sensor in dc SQUIDs and has a number of other important applications [4]. On the other hand, the single-contact interferometer represents a macroscopic system with two quantum states and, hence, can be used for constructing a quantum computer [5]. The influence of small thermal fluctuations on single-contact interferometers was previously considered in [6]. The suppression of quantum interference by intense thermal fluctuations was studied in [7–9].

The potential energy of a single-contact interferometer can be expressed as

$$U(\phi) = U_S + U_L = E_J\left(1 - \cos\phi + \frac{(\phi - \phi_e)^2}{2l}\right), \quad (1)$$

where $E_J = \hbar I_C/2e$ is the Josephson energy, $l = 2\pi I_c L/\Phi_0$ is the normalized inductance of the ring, $\phi = 2\pi\Phi/\Phi_0$ is the Josephson phase, and $\phi_e = 2\pi\Phi_e/\Phi_0$ is the phase related to the external magnetic flux Φ_e. In Eq. (1), the first term is related to the Josephson current and the second, to the magnetic energy stored in the inductance of the superconducting ring.

Calculations of the average value of the Josephson "interference" term in Eq. (1) yielded [7]

$$U_S = -E_J \cos\langle\phi\rangle \exp\left(-\frac{L}{L_F}\right), \quad (2)$$

where L_F is the so-called "fluctuational" inductance defined as

$$L_F = \left(\frac{\Phi_0}{2\pi}\right)^2 \frac{1}{kT}. \quad (3)$$

For $L > L_F$, the interference is sharply suppressed by thermal fluctuations. This fact imposes limitations on the ring size in a superconducting interferometer.

Formulas (2) and (3) show that, in contrast to single Josephson junctions, in which the Josephson effect is suppressed at $\gamma = E_J/kT \approx 1$ (see [4]), suppression of the interference in a single-contact interferometer with $l \ll 1$ takes place for $\gamma \sim l^{-1} \gg 1$. At low temperatures, an important role belongs to quantum fluctuations. This study was aimed at determining the influence of such quantum fluctuations on the operation of a single-contact interferometer.

As is well known, the state of a single-contact interferometer is described by the following equation [4]:

$$\phi + l\sin\phi = \phi_e. \quad (4)$$

Manifestations of the quantum effects make the Josephson phase ϕ a quantum variable $\hat{\phi}$. In the $\hat{\phi}$ representation, the electric charge Q acquires the form of $\hat{Q} = -2ei\frac{\partial}{\partial\phi}$. The operation of a single-contact interferometer in the quantum regime should be considered in terms of the following Hamiltonian:

$$\hat{H} = \frac{\hat{Q}^2}{2C} + E_J\left(1 - \cos\phi + \frac{(\phi - \phi_e)^2}{2l}\right). \quad (5)$$

Low-inductance interferometer ($l \ll 1$). In this case, the Josephson potential $1 - \cos\phi$ serves as a perturbation for the zero-order Schrödinger equation

$$\left\{\frac{\hat{Q}^2}{2C} + E_J\frac{\phi^2}{2l}\right\}\Psi = E_n\Psi, \quad (6a)$$

where E_n are the eigenvalues of the quantum-mechanical oscillator

$$E_n = \hbar\omega\left(n + \frac{1}{2}\right); \quad \omega^2 = \frac{1}{LC}. \qquad (6b)$$

Calculations within the framework of the first-order perturbation theory yield the following correction to the energy spectrum:

$$\Delta E_n = E_J\left\{1 - \cos\phi_e \exp\left(-\frac{\pi^2\hbar\omega L}{\Phi_0^2}\right)L_n\left(\frac{2\pi^2\hbar\omega L}{\Phi_0^2}\right)\right\}, \quad (7)$$

where L_n are the Laguerre polynomials. The matrix element of the superconducting current in the ground state ($n = 0$, $L_0 = 1$) is given by the formula

$$\langle 0|I_c\sin\phi|0\rangle = -\frac{2\pi E_J}{\Phi_0}\sin\phi_e \exp\left(-\frac{\pi^2\hbar\omega L}{\Phi_0^2}\right). \qquad (8)$$

According to this relation, the superconducting current is suppressed by quantum fluctuations for

$$L > L_F = \left(\frac{\Phi_0}{\pi}\right)^2\left(\frac{1}{\hbar\omega}\right).$$

High-inductance interferometer ($l \gg 1$). In this case, the quadratic term in the Hamiltonian (5) can be ignored (given a sufficiently slow variation of the external magnetic field). This implies that the high-inductance interferometer is analogous to a single Josephson junction [10]:

$$\left\{\frac{\hat{Q}^2}{2C} + E_J\left(1 - \cos\phi - \frac{\phi_e^2}{2l}\right)\right\}\Psi = E_n\Psi. \qquad (9)$$

This equation is equivalent to the Mathieu equation with a certain shift in the spectrum: $E_J\phi_e^2/2l$. In the ground state, the eigenvalue is

$$\frac{E_0}{E_Q} = \frac{E_J}{E_Q}\left(1 + \frac{\phi_e^2}{2l} - \frac{1}{4}\frac{E_J}{E_Q}\right). \qquad (10)$$

Taking into account asymptotic expressions for the Mathieu functions [11], we can calculate the matrix

element of the superconducting current for a large inductance as

$$\langle 0|I_c\sin\phi|0\rangle = \frac{l\Phi_e}{L(l+1)} \approx \frac{\Phi_e}{L}. \qquad (11)$$

This implies that all the phase drops on the inductance of the superconducting ring and the average current is proportional to the external flux. The above formulas are also useful in evaluating the quantum limit of the energy sensitivity of high-frequency SQUIDs.

In summary, a theory of quantum fluctuations in a single-contact interferometer has been developed. In a low-inductance interferometer, the superconducting current is sharply suppressed by quantum fluctuations when the inductance exceeds a certain "fluctuational" threshold. An expression for this "fluctuational" inductance is obtained by replacing the thermal energy kT with $\hbar\omega$ in formula (3). In the case of a high inductance of the interferometer ring, the interference is always suppressed and this scheme behaves like a single microscopic Josephson junction.

REFERENCES

1. *Quantum Mesoscopic Phenomena and Mesoscopic Devices in Microelectronics,* Ed. by I. O. Kulik and R. Ellialtioglu (Kluwer, Dordrecht, 2000).
2. L. S. Kuzmin, Yu. Pashkin, D. S. Golubov, and A. D. Zaikin, Phys. Rev. B **54**, 10074 (1996).
3. I. N. Askerzade, Zh. Tekh. Fiz. **73** (4), 140 (2003) [Tech. Phys. **48**, 519 (2003)].
4. K. K. Likharev, *Dynamics of Josephson Junctions and Circuits* (Nauka, Moscow, 1985; Gordon and Breach, New York, 1986).
5. T. Orlando, J. E. Mooji, L. Tian, *et al.*, Phys. Rev. B **60**, 15398 (1999).
6. I. N. Askerzade, Zh. Tekh. Fiz. **71** (12), 88 (2001) [Tech. Phys. **46**, 1575 (2001)].
7. V. A. Khlus and I. O. Kulik, Zh. Tekh. Fiz. **45** (4), 449 (1975) [Sov. Phys. Tech. Phys. **20**, 283 (1975)].
8. P. W. Anderson, in *Lectures on Many-Body Problems,* Ed. by E. R. Caianiello (1962), p. 113.
9. P. V. Elyutin and V. D. Krivchenkov, *Quantum Mechanics* (Nauka, Moscow, 1976) [in Russian].
10. K. K. Likharev and A. B. Zorin, J. Low Temp. Phys. **62**, 345 (1986).
11. M. Abramovitz and I. A. Stegun, *Handbook of Mathematical Functions* (Dover, New York, 1971).

Translated by P. Pozdeev

Pneumatic-Driven Piston Acceleration in a Barrel

S. V. Bulovich* and R. L. Petrov

St. Petersburg State Technical University, St. Petersburg, 195251 Russia
* e-mail: bulovich@ista-pneumatics.ru
Received March 25, 2005

Abstract—The regime of pneumatic acceleration of a piston in a barrel up to a transonic velocity has been studied. The results are obtained by numerical solution of a system of nonstationary equations for a narrow channel, which have been integrated to within the second order of accuracy with respect to temporal and spatial variables. Quantitative estimates are obtained for the influence of various factors on the piston velocity, including wave processes, friction, heat exchange, and pressure in front of the moving piston. Some aspects of the formation of a nonstationary turbulent boundary layer at the barrel wall behind the piston are considered. © 2005 Pleiades Publishing, Inc.

The phenomenon of the acceleration of a body under the action of excess pressure has numerous practical applications. For certain reasons, the use of explosives for creating a high excess pressure is not always possible. An alternative solution is offered by a pneumatic ballistic system, which comprises a high-pressure chamber (receiver), a lock device (a diaphragm or a high-speed valve), and a barrel. The system parameters are selected proceeding from the desired final velocity U of a body with mass M and diameter D. In order to provide for the required velocity, it is necessary to choose the appropriate barrel length L, high-pressure chamber volume V, gas composition, and the initial gas pressure P^0 and temperature T^0 in the receiver. This corresponds to the well-known formulation of an inner problem (Lagrange problem) [1].

The simplest means of calculating the motion of a body in a barrel is to use the quasi-stationary approach, which ignores the wave phenomena in the system. However, these phenomena must be taken into account for velocities that are comparable with the velocity of sound. It is also desirable to make allowance for the friction and heat exchange at the barrel walls.

Data on the friction and heat exchange at the walls of a gun barrel in the case of the explosion of a powder charge were presented in [2], but the values of velocities were not reported. A solution was obtained within the framework of a narrow channel model formulated in a nonconservative form. The use of such a mathematical model is justified in the case of extended barrels.

In this study, the problem of the description of the gas flow and piston motion in a barrel has been solved for a pneumatic ballistic system. We have considered a completely conservative system of equations and considerably simplified the algorithm of solution.

The turbulent regime of gas flow in the barrel was modeled within the framework of a two-layer algebraic model of turbulence. The gas flow characteristics in the inner region of a boundary layer were described using the first Prandtl hypothesis with the van Drist damping factor in the vicinity of the barrel wall. In the outer region of the boundary layer, the gas flow was described using the trace-like Klauser model, while the region of intermittency at the external surface of the boundary layer was described in terms of the Klebanov function. A detailed description of the turbulence model and its practical applications can be found in [3].

The current state of the gasdynamic variables in the receiver was described within the framework of a quasi-stationary model. The gas yield from the high-pressure chamber to the barrel was determined according to the theory of characteristics, proceeding from the values of gasdynamic functions in the receiver and at the barrel input edge.

The gas action on the piston was determined as the difference of pressures at the front and rear edges. The pressure behind the piston was determined by solving the problem on a gas flow in the barrel. The pressure in front of the piston was calculated as the pressure in a simple compression wave [4].

The system of difference equations was numerically integrated using a predictor–corrector scheme to within the second order of accuracy with respect to temporal and spatial variables [5]. Discretization of the calculation region was provided by a mobile lattice following the piston moving in the barrel. In the course of problem solution in the transverse direction, the lattice remained two-dimensional. In the radial direction, we used a nonuniform lattice that provided an adequate resolution for the structure of a nonstationary turbulent boundary layer.

The calculations were performed for the following set of parameters: piston mass, $M = 0.2$ kg; barrel diameter, $D = 0.04$ m; high-pressure chamber volume, $V = 1.5 \times 10^{-3}$ m³; initial gas pressure in the receiver, $P^0 = 7.0$ MPa; initial gas temperature, $T^0 = 300.0$ K. The bar-
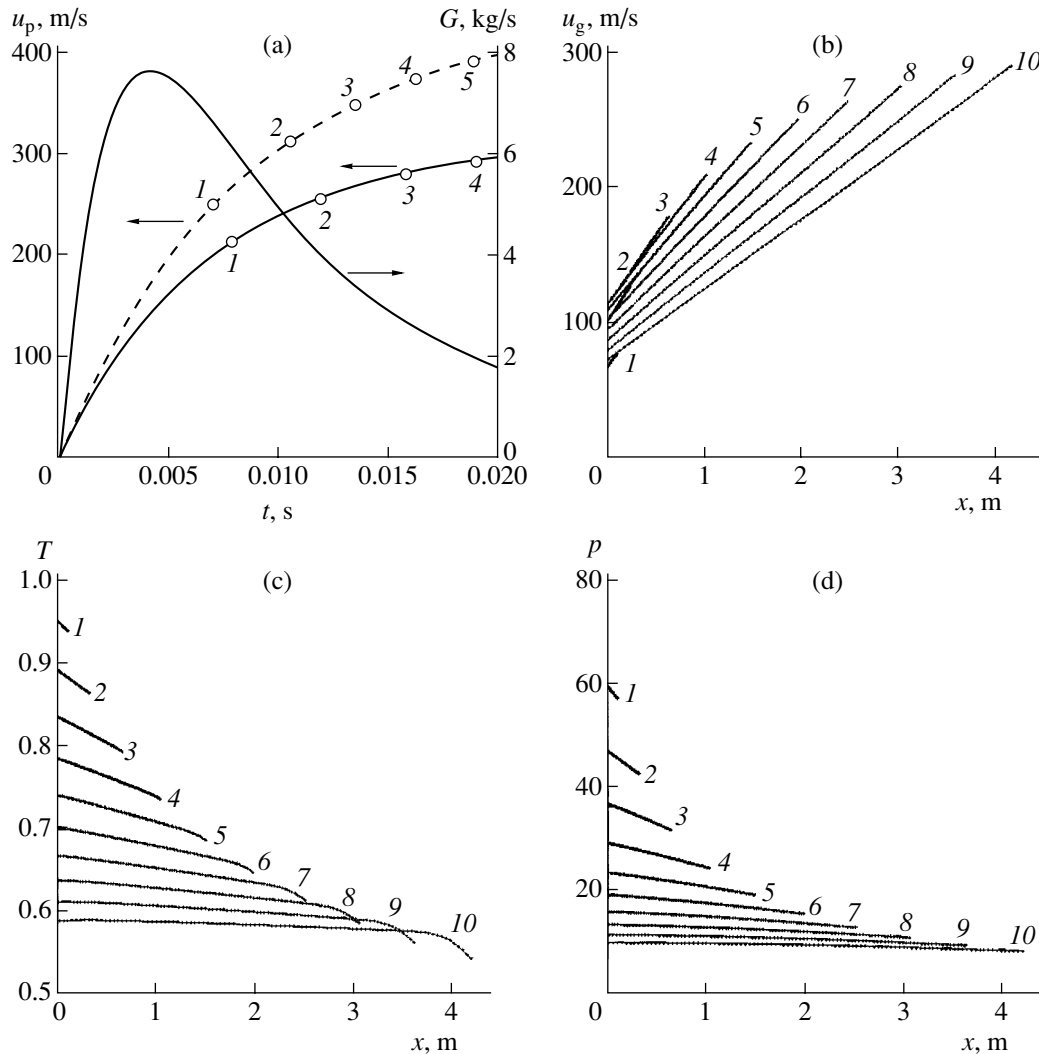
Fig. 1. (a) Time variation of the piston velocity u_p and the rate of gas outflow from the receiver and (b–d) longitudinal profiles of the gas velocity u_g (averaged over the channel cross section), gas temperature T (normalized to the initial value), and gas pressure p (normalized to the initial gas pressure in the barrel) in the barrel, respectively.

rel wall temperature was assumed to be constant and equal to the initial temperature. The working gas was air. The calculation was performed on a 100×90 lattice.

The results of numerical calculations are illustrated in Fig. 1. Figure 1a shows the time variation of the piston velocity and the rate of gas outflow from the receiver. For comparison, the dashed curve shows the piston velocity in the case of a quasi-stationary acceleration with neglect of the kinetic energy of the gas. Figures at the curves indicate the distance (in meters) traveled by the piston in the barrel. Figures 1b–1d show the longitudinal profiles of the gas velocity, temperature, and pressure averaged over the barrel cross section (the gas pressure and temperature are normalized to the initial values). Here, the figures at the curves indicate the time (multiple of 2 ms).

As can be seen, there are two regions featuring gas expansion, albeit with different intensities. The first region of high-rate expansion is that immediately adjacent to the accelerated body. Here, the accelerated motion of the piston in the barrel leads to the generation of gas rarefaction waves. The interaction between these rarefaction waves results in the development of a longitudinal pressure gradient in the barrel, which reduces the efficiency of action of the current receiver pressure on the piston. The longitudinal pressure gradient leads to an increase in the gas flow velocity along the barrel (Fig. 1b). The second region, in which the gas exhibits a less intense expansion, is the high-pressure chamber where the gas pressure and temperature decrease as a result of the gas yield from receiver to barrel. Subsequent expansion of the gas in the barrel can result (as in our case) in the appearance of a maximum on the curve of the rate of gas outflow from the high-pressure cham-
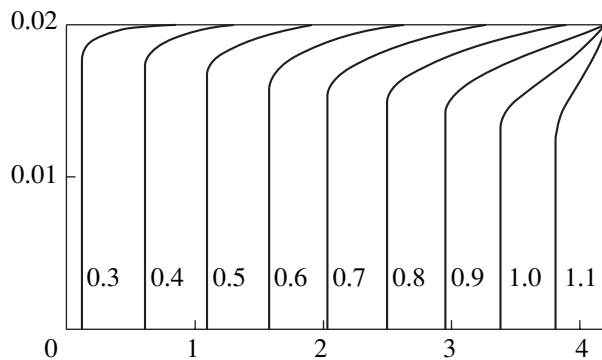
Fig. 2. The typical gas flow structure in the barrel, as represented by the constant-*M*-level lines at the moment of time $t = 20$ ms after the piston acceleration start (the transverse direction corresponds to the radial coordinate).

ber despite the increasing piston velocity. Another factor influencing the gas transmission capacity of the channel is a boundary layer formed at the barrel wall.

In a long barrel, both the temperature and dynamic boundary layers can form at the barrel wall. The boundary layers of the gas remain nonstationary, which is caused both by a change in the linear scale of the problem (related to the piston motion along the barrel) and by variation of the gasdynamic functions at the external surface of the boundary layer. The existence of a developed boundary layer reduces the gas transmission capacity of the barrel. For the selected parameters, the presence of a boundary layer results in the formation of a transonic flow at the core, featuring a transition across the sound line ($M = 1$). As a result, the gas flow in the barrel acquires properties that resemble the flow in the Laval nozzle. A significant difference consists in that

the line with $M = 1$ shifts downstream behind the piston. The typical gas flow structure in the barrel, as represented by the constant-*M*-level lines at the moment of time $t = 20$ ms after the piston acceleration start, is shown in Fig. 2 (where the transverse direction corresponds to the radial coordinate).

The results of our calculations revealed the following peculiarity of the gas flow in the barrel. The model velocity slightly exceeds the velocity of sound. The effects of the wave processes, as well as of the friction and heat exchange at the barrel walls, are manifested in a decrease in this velocity. For example, in a 3-m-long barrel, the deviation reaches 20%, and this effect grows with increasing piston velocity.

REFERENCES

1. N. A. Zlatin, A. P. Krasil'shchikov, G. I. Mishin, and N. N. Popov, *Ballistic Installations and Their Application in Experimental Research* (Nauka, Moscow, 1974) [in Russian].

2. A. M. Bubenchikov, A. V. Komarovskiĭ, and S. N. Kharlamov, *Mathematical Models of Flow and Heat Exchange in the Inner Problems of Viscous Gas Dynamics* (Tomsk State University, Tomsk, 1993) [in Russian].

3. Yu. V. Lapin and M. Kh. Strelets, *Internal Gas Mixture Flows* (Nauka, Moscow, 1989) [in Russian].

4. L. G. Loitsyanskiy and R. H. Nunn, *Fluid and Gas Mechanics*, 6th ed. (Nauka, Moscow, 1987; Begell, New York, 1995).

5. S. V. Bulovich, in *Proceedings of the Scientific-Practical Conference and School-Seminar on High Innovation Technologies* (St. Petersburg State Technical University, St. Petersburg, 2004), pp. 188–207.

Translated by P. Pozdeev

Photoacoustic Thermoelastic Effect Near Vickers Indentations in Nanocrystalline Nickel

K. L. Muratikov, A. L. Glazov, and V. I. Nikolaev

Ioffe Physicotechnical Institute, Russian Academy of Sciences, St. Petersburg, 194021 Russia
Received April 7, 2005

Abstract—The character of the photoacoustic (PA) signal variations in the vicinity of Vickers indentation zones in nanocrystalline nickel has been studied. PA images revealing the response signal features inside and outside these zones have been obtained. The character of the PA signal variation is compared to that predicted by the existing model relating the PA response to stress-induced changes in the thermoelastic coupling coefficient of the material. It is shown that the existing model adequately describes the observed character of internal stress variations near the indentations sites only in the absence of additional stresses related to the sample preparation technology. © 2005 Pleiades Publishing, Inc.

In recent years, the photoacoustic (PA) thermoelastic effect in stressed materials has received much attention [1–5]. Important results related to features of the PA response have been obtained, especially in stressed brittle materials. In particular, the PA signal behavior at the ends of radial cracks formed near Vickers indentations in nitride ceramics was studied in [4, 6, 7] and analogous investigations for Al_2O_3–SiC–TiC composite ceramics were performed in [8, 9]. The obtained data revealed substantial anomalies in the PA signal behavior at the ends of radial cracks, which were related to features in the concentration of internal stresses in these regions. We have also studied the influence of external mechanical stresses on the PA images of indentation zones in composite ceramics [8, 9]. The experimental results confirmed that a theoretical model of the PA effect developed previously [10] provides a good description of the PA signal behavior in response to both normal and tangential stresses.

Much less attention has been devoted to the investigation of the PA effect in stressed metals. The ability of PA imaging to reflect the stressed state of aluminum was pointed out in [1], and some results concerning the influence of residual stresses in the PA effect in titanium were obtained in [11]. Unfortunately, no systematic investigations have been performed thus far and the prospects for using the PA method for imaging mechanical stresses in metals remain unclear.

In this context, the main aim of this study was to consider the PA effect in metals featuring internal stresses. The experimental investigations were carried out on the samples of nanocrystalline nickel (99.9% Ni) obtained by means of equichannel angular pressing according to a technology described in [12]. According to the results of electron-microscopic investigations, the grain size in the obtained samples did not exceed 200 nm. The internal stresses in the samples were cre-

ated by means of Vickers microindentation, which is the most reliable and reproducible method for introducing plastic strain and internal stresses in various materials [13].

The experiments were performed on a sample with dimensions $4.8 \times 3.2 \times 2.9$ mm. One surface of the sample was polished and indented according to Vickers under a load of 49 N, using different orientations of the indentor relative to the sample surface. The PA measurements were performed using a piezotransducer with a resonance frequency of about 140 kHz, which was fastened on the rear side of the sample. The exciting laser radiation was focused in a spot with a diameter of about 1 μm. The PA image was formed by moving the sample along two coordinate axes at a 2.5 μm step.

Figure 1 presents the typical PA image of a region of the sample surface in the vicinity of a Vickers indentation site. As can be seen, the PA signal exhibits rather strong changes inside the zone of indentor action on the material, whereas the signal variations outside this zone are much less pronounced. In this study, attention was mostly focused on the character of PA signal variation outside the indentation zone.

Since the PA response variations outside the indentation zone are rather small, the observed signal behavior can be described in terms of a theory developed in [14], where general expressions for PA signal changes reflecting the effect of elastic strain or internal stresses on the thermoelastic coupling coefficient of an inhomogeneous object were obtained using the perturbation theory. According to the results obtained in [14], the PA signal ΔV_1 can be expressed as

$$\Delta V_1 = C_1 \frac{1 + \sigma}{\pi E} \frac{1}{z^3} \int d^3 r' \gamma_1(r') \Delta T^{(0)}(r'), \qquad (1)$$

where C_1 is a coefficient dependent on the piezotransducer parameters, σ is the Poisson ratio, E is Young's
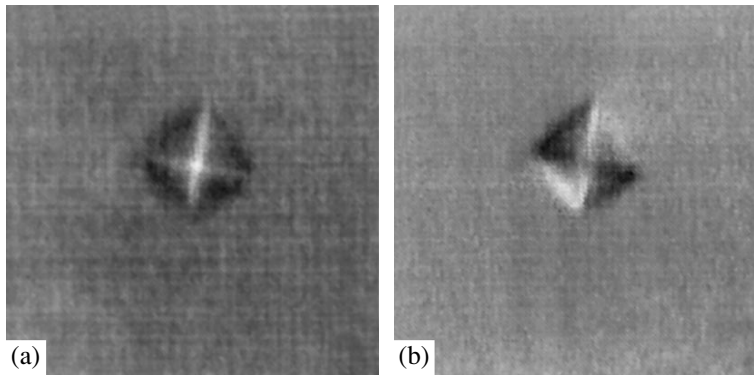
Fig. 1. The typical photoacoustic images obtained in the (a) signal amplitude mode and (b) signal phase mode in the vicinity of a Vickers indentation on the surface of nanocrystalline nickel (indentor load, 49 N; imaged area size, 1 × 1 mm; excitation laser radiation modulated at 142 kHz).

modulus, z is the sample thickness, γ_1 is the change in the thermoelastic coupling coefficient caused by elastic strain or internal stresses, and $\Delta T^{(0)}$ is the temperature field created in the sample under the action of exciting laser radiation.

Expression (1) can be used for determining the effect of internal stresses developed near the indentation sites in nanocrystalline nickel on the PA signal behavior. In solving this task, it is necessary to take into account the following circumstances. First, the results obtained previously [8, 9] showed that changes in the thermoelastic coupling coefficient caused by the internal stresses at the sample surface can be considered as proportional to a sum of the internal stress tensor components, $\sigma_{xx} + \sigma_{yy}$ (where x and y are the coordinate axes in the sample surface plane). Second, in determining the PA signal behavior outside the indentation zone in the first approximation, this zone can be considered as spherically symmetric [15], so that the $\sigma_{xx} + \sigma_{yy}$ is proportional to the radial stress tensor component σ_r. According to a model developed in [15], the σ_r value outside the indentation zone varies as

$$\sigma_r = -\frac{\sigma_r^{(0)} r_0^2}{r^2}, \qquad (2)$$

where r_0 is the indentation zone radius and $\sigma_r^{(0)}$ is the stress at the indentation zone boundary.

Figure 2 shows the PA signal intensity profile along a horizontal line passing through the center of the Vickers indentation. It should be noted that the profiles measured in other directions have similar shapes. The PA image presented in Fig. 1 was obtained using the exciting radiation modulated by a piezotransducer at a frequency of 142 kHz. Under these conditions, the thermal wavelength in the sample is significantly smaller than the characteristic scale of internal stress variations. Then, according to relation (1), the PA signal changes must reflect the character of variation of the induced

internal stresses. As can be seen from Fig. 2, the average PA signal behavior well agrees with the character of internal stress variation at the indentation site, despite certain local inhomogeneities present in the sample of nanocrystalline nickel.

It is necessary to make the following important remark concerning the data presented in Figs. 1 and 2, which is related to a special choice of the Vickers indentation with a symmetric structure of the PA image. A rather large number of PA images from various indentations in nanocrystalline nickel did not obey this condition. Such images exhibited a rather strongly pronounced asymmetry in the PA signal variation inside the indentation zone. This behavior can be explained by the simultaneous action of internal stresses induced by
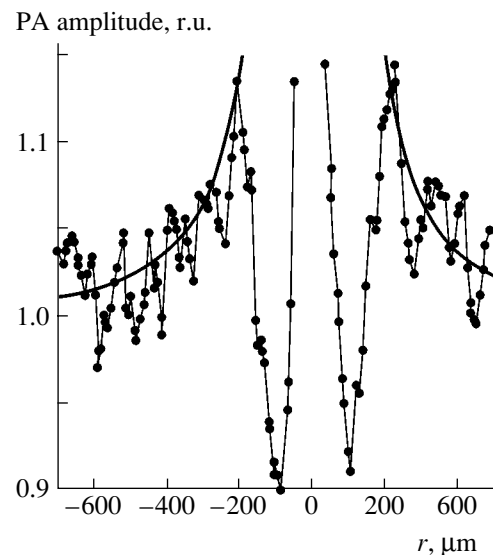
Fig. 2. The photoacoustic signal intensity profiles along a line passing through the center of a Vickers indentation on the surface of nanocrystalline nickel. Points represent the experimental data; the solid curve shows the results of theoretical calculations in terms of the $1/r^2$ law.

the indentor and the residual internal stresses developed in the material in the course of sample preparation.

The possible presence of additional internal stresses related to the sample preparation technology was not taken into account in the theoretical model developed in [15]. The law of the internal stress variation expressed by Eq. (2) refers only to the indentation process. However, real samples feature additional internal stresses developed in the course of preparation. For this reason, the internal stress variation near the indentation site in the general case can deviate from the behavior predicted by relation (2). Under these conditions, the proposed model of the PA response formation needs to be refined. The validity of these considerations is confirmed by the results of our previous investigations of the PA effect in the vicinity of indentation sites in ceramics. It was established [8, 9] that the external mechanical stresses applied along the sample surface could significantly modify the structure of the PA images of the Vickers indentation sites in ceramics. In particular, the additional stresses may significantly alter the character of the PA images of such indentations, distorting the initially symmetric patterns and rendering them asymmetric. Unfortunately, direct allowance for such additional internal stresses related to the material processing or sample preparation technology cannot be performed within the framework of the existing model [15]. This situation requires special analysis, which will be performed in subsequent investigations.

REFERENCES

1. M. Kasai and T. Sawada, *Photoacoustic and Photothermal Phenomena II, Springer Series in Optical Sciences* (Springer-Verlag, Berlin, 1990), Vol. 62, pp. 33–36.

2. J. H. Cantrell, M. Qian, M. V. Ravichandran, and K. W. Knowles, Appl. Phys. Lett. **57**, 1870 (1990).

3. R. M. Burbelo and M. K. Zhabitenko, *Progress in Natural Science* (Taylor & Francis, London, 1996), Vol. 6, pp. 720–723.

4. K. L. Muratikov, A. L. Glazov, D. N. Rose, and J. E. Dumar, Pis'ma Zh. Tekh. Fiz. **23** (5), 44 (1997) [Tech. Phys. Lett. **23**, 188 (1997)].

5. F. Jiang, S. Kojima, B. Zhang, and Q. Yin, Jpn. J. Appl. Phys., Part 1 **37**, 3128 (1998).

6. K. L. Muratikov and A. L. Glazov, Zh. Tekh. Fiz. **70** (8), 69 (2000) [Tech. Phys. **45**, 1025 (2000)].

7. K. L. Muratikov, A. L. Glazov, D. N. Rose, and J. E. Dumar, J. Appl. Phys. **88**, 2948 (2000).

8. K. L. Muratikov, A. L. Glazov, D. N. Rose, and J. E. Dumar, High Temp. High Press. **34**, 585 (2002).

9. K. L. Muratikov and A. L. Glazov, Zh. Tekh. Fiz. **73** (8), 90 (2003) [Tech. Phys. **48**, 1028 (2003)].

10. K. L. Muratikov, Zh. Tekh. Fiz. **69** (7), 59 (1999) [Tech. Phys. **44**, 792 (1999)].

11. R. M. Burbelo and M. K. Zhabitenko, Ukr. J. Phys. **49**, 191 (2004).

12. V. M. Segal, V. I. Reznikov, A. E. Drobyshevskiĭ, and V. I. Kopylov, Izv. Akad. Nauk SSSR, Met., No. 1, 115 (1981).

13. R. F. Cook and G. M. Pharr, J. Am. Ceram. Soc. **73**, 787 (1990).

14. K. L. Muratikov, Pis'ma Zh. Tekh. Fiz. **30** (22), 58 (2004) [Tech. Phys. Lett. **30**, 956 (2004)].

15. E. H. Yoffe, Phil. Mag. A **46**, 617 (1982).

Translated by P. Pozdeev

Using Open Atmospheric Electric Discharge for Water Purification from Surface Contamination with Oil Products

Yu. A. Barinov, V. B. Kaplan, and S. M. Shkol'nik*

Ioffe Physicotechnical Institute, Russian Academy of Sciences, St. Petersburg, 194021 Russia
* e-mail: shkolnik@mail.ioffe.ru
Received April 17, 2005

Abstract—The characteristics of open atmospheric dc discharge between a liquid nonmetal cathode (tap water layer) and a metal anode have been studied. The effect of discharge on a layer of oil products (diesel fuel, lubricant oils) contaminating the liquid cathode surface was determined. The discharge current–voltage characteristics and the dependence of the cathode current density on the discharge current I were measured in the interval $20\ \text{mA} \leq I \leq 300\ \text{mA}$ for the discharge gap width varied within $h = 2\text{–}10$ mm. For $h \geq 4$ mm and $I \geq 120$ mA, the cathode current density and the interelectrode voltage are independent of the discharge current, which is characteristic of the normal glow discharge. Under the action of discharge, oil products in the contamination layer on the liquid cathode surface are partly decomposed and partly converted, after which the conversion products can be readily removed from the surface by mechanical methods. The efficiency of contaminant removal can reach 98%. Analysis of the conversion products showed that they are composed of polymer chains with variable length and structure involving oxygen-containing groups. © *2005 Pleiades Publishing, Inc.*

Introduction. Methods for the purification and disinfection of gas and liquid flows by means of electric discharges of various types have been extensively developed in recent years. From this standpoint, it is especially interesting to consider discharges in which the role of electrodes (one or both) is played by a weakly conducting fluid (e.g., aqueous solutions, electrolytes, technical and tap water) [1]. On the one hand, such discharges can be used for the generation of strongly nonequilibrium plasma with a high density of chemically active radicals at elevated pressures (up to atmospheric pressure and above). On the other hand, the flows of energy and chemically active particles to electrodes may influence the state of the electrode liquid and stimulate various physicochemical processes in this liquid.

Previously, we studied the electric discharge between two streams of tap water in air at atmospheric pressure. It was established that, at a discharge current density of $j \sim 5 \times 10^{-1}\ \text{A/cm}^2$, conditions in the discharge column led to the generation of plasma with a heavy particle temperature of $T \approx 0.15\text{–}0.17$ eV, an average electron energy of $T_e \approx 0.35\text{–}0.4$ eV, a charged particle density of $n \sim 10^{12}\ \text{cm}^{-3}$, and a high concentration of chemically active radicals ($N_{\text{NO}} \sim 10^{16}\text{–}10^{17}\ \text{cm}^{-3}$, $N_{\text{OH}} \sim 10^{16}\text{–}10^{17}\ \text{cm}^{-3}$, $N_{\text{O}} \sim 10^{14}\text{–}10^{15}\ \text{cm}^{-3}$, etc.) [2, 3]. In addition, the discharge column (especially the near-electrode regions) emitted UV radiation with a power density of $\sim 10\ \text{mW/cm}^3$ in a 235–300 nm wavelength range [4].

In this study, we have measured the main electrical characteristics of the dc discharge between a liquid cathode (tap water layer) and a metal anode in air at atmospheric pressure. It is established that such discharges can be used for the purification of the electrode medium (water) from a surface contamination layer consisting of oil products.

Experimental. The open atmospheric discharge was initiated in air with the aid of an auxiliary electrode and power supplied via a 5-kΩ ballast resistor from a dc current source, which provided an output voltage of 0–3.5 kV with pulsation amplitude below 1 V. The cathode was a layer of tap water in a cylinder with a diameter of ~70 mm and a large metal electrode on the bottom, which was connected to the negative lead of the dc current source. The water layer thickness above the electrode was ~10 mm. The water surface was covered with a model contamination layer by applying a certain amount (1 ml) of an oil product (diesel fuel, spindle oil, or MS-20 grade machine oil). The anode was a water-cooled 3-mm-diameter molybdenum rod with a rounded end. The interelectrode gap (i.e., the distance from the liquid cathode surface to the metal electrode end) could be varied within $h = 2\text{–}10$ mm.

In the course of experiments, we measured the discharge current and voltage and photographed discharge with the aid of a Canon A85 camera at an exposure time of 1/200 s. Taking into account our previous results [4], which showed that the emission from discharge between water streams was predominantly concentrated within the violet and UV spectral ranges, we have

compared the images made with and without a yellow optical filter #11.

After termination of the experiments with discharge, the residual oil products and their conversion products were mechanically (with the aid of a wire loop) removed from the liquid electrode (water) surface and analyzed. The electrode water was analyzed at a laboratory of the North Plant Safety Department, and the oil conversion products were analyzed at the Laboratory of Physicochemical Analytical Methods of the GPECh Institute (both laboratories are certified by the State Committee of Standards).

Results and discussion. The experiments showed that the discharge was contracted on the anode and diffuse on the cathode. The cathode spot diameter D, as determined by the size of the glow region, was the same on the photographs made with and without the optical filter. At a minimum interelectrode gap ($h = 2$ mm), an increase in the discharge current above $I \sim 150$ mA led to a splitting of the channel (and the electrode spots) into two parts. At $I > 250$ mA, the two parts merged together again and the discharge became diffuse on both anode and cathode. For greater interelectrode distances ($h = 4$–10 mm), the anode spot was contracted in the entire range of discharge currents used ($I \leq 300$ mA).

The dependence of the cathode spot diameter D on the discharge current I at $h = 2$ mm and $I \leq 150$ mA is well described by a square root curve. For $h = 4$ mm and above, this law is obeyed only for $I \geq 120$ mA. Accordingly, the current density j_c on the cathode in a short discharge is independent of the total discharge current at $I \leq 150$ mA. In contrast, for $h = 4$ mm and above, we have $j_c = $ const for $I > 120$ mA, while at lower currents j_c depends on I in a nonmonotonic manner (Fig. 1).

The discharge voltage U consists of the voltage drops in the liquid cathode and in the air gap. Figure 2 shows the current–voltage characteristics of discharge with a rod metal anode. For a long discharge ($h \geq 4$ mm) and small discharge currents, the discharge voltage weakly varies with the current, while for $I > 120$ mA (i.e., in the region where $j_c = $ const) the voltage remains unchanged ($U = $ const). In a short discharge, the voltage exhibits monotonic growth in the interval 20 mA $\leq I \leq$ 150 mA (where $j_c = $ const). The behavior, whereby the current density and voltage are independent of the total discharge current, is characteristic of the normal glow discharge. We may suggest that the anomalous (in this respect) behavior observed in the case of a short discharge is related to the fact that, under such conditions, the interelectrode gap ($h = 2$ mm) is comparable to the length l_c of a cathode layer. Indeed, the latter value for a discharge with liquid (water) cathode at atmospheric pressure is $l_c \approx 1.5$–2 mm [2].

It was established that the application of a layer of oil products (in the amount indicated above) on the water surface did not change the electrical characteris-
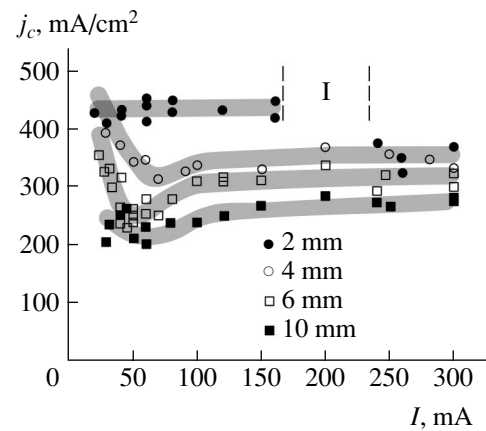

Fig. 1. Plots of the cathode spot current density versus total discharge current for various interelectrode gap widths. Region I corresponds to unstable discharge.
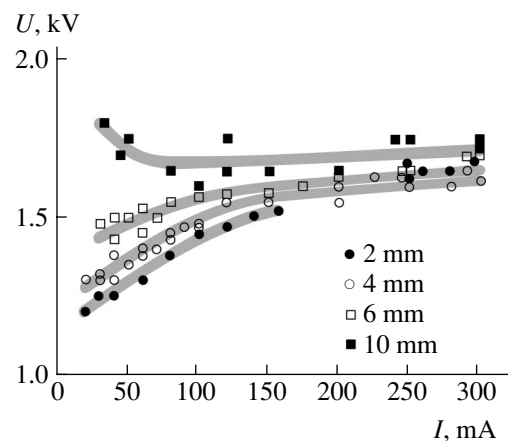

Fig. 2. Discharge current–voltage characteristics measured for various interelectrode gap widths.

tics of the discharge. The action of discharge on the layer of contaminations on the liquid cathode (water) surface was studied in a regime of discharge with $I \approx 150$ mA and $h = 4$–5 mm. The discharge-induced heating of the surface layer of liquid (which took place within the first several dozen seconds after switching the discharge on) led to the appearance of visible convective flows, whereby the oily film was drawn into the cathode spot and a certain product (appearing as a loose converging trace of a brown color) was drawn out of the spot. This conversion product was surrounded by the residual oil products and formed a conglomerate representing a substance with a rather high surface tension, which could be effectively removed from water by mechanical means (e.g., with the aid of a wire loop).

The time required for the treatment of surface contaminations depends on the required degree of purification. Under the conditions indicated above, the main fraction of contaminations was converted within $t \sim 10$ min. According to the results of analyses, the treatment for $t \sim 25$–30 min removed up to 98% of the surface contaminant.

Under the action of discharge, the diesel fuel was predominantly burned out, while the lubricant oils were converted approximately by half. Accordingly, the mass of the collected and dried conglomerate amounted in the former case to 4–5% and, in the latter, to 45–50% of the initial contaminant weight.

For the removal of lubricant oil contaminations with an efficiency of ~70–80%, the specific electric energy consumption was about 4×10^{-2} (kW h)/ml, while the energy spent for the removal of diesel fuel was much lower. Water purification up to ~98% required a specific energy consumption on the order of 10^{-1} (kW h)/ml. The results of some preliminary experiments showed that this energy characteristic of the process can be reduced by means of the optimization of the process, for example, by the mechanical stirring of the surface layer of liquid, using a moving electrode, etc.

For an analysis of the conversion products as such, the separated conglomerate was dried and washed with solvents to remove the residual oil products. The conversion products have proved to be poorly soluble in common solvents. We tried hexane, acetone, ethanol, methylene chloride, and DMSO (at room temperature, upon heating to 40°C, and with additional ultrasonic treatment). The most effective solvent was acetone.

The obtained acetone solutions of the conversion products were analyzed by gas chromatography (GC) and high-performance liquid chromatography (HPLC). In addition, the filtrates were studied by IR absorption spectroscopy.

The results of analyses showed that the action of discharge on the diesel fuel and lubricant oils probably leads to the formation of products with long polymer chains. The partial solubility of the conversion products is indicative of their broad distribution with respect to chain length and structures. The polymer chains probably involve oxygen-containing groups, which can be related either to oxygen liberation in the surface layer of water as a result of the cathode liquid hydrolysis, or to the supply of oxygen from atmosphere.

Conclusions. The results of our investigation of the open dc discharge between a liquid (tap water) cathode and a metal anode in air at atmospheric pressure showed that the discharge characteristics are close to those of the normal glow discharge. The discharge action on the contamination layer of oil products covering the liquid cathode surface leads to partial decomposition and partial conversion of the contaminant, after which the conversion products can be readily removed from the surface by mechanical methods.

REFERENCES

1. F. M. Gaǐsin and É. E. Son, in *Encyclopedia of Low-Temperature Plasma*, Ed. by V. E. Fortov (Nauka, Moscow, 2000), Vol. 2, pp. 241–246 [in Russian].

2. P. Andre, Yu. Barinov, G. Faure, *et al.*, J. Phys. D **34**, 3456 (2001).

3. P. Andre, J. Aubreton, Yu. Barinov, *et al.*, J. Phys. D **35**, 1846 (2002).

4. Yu. A. Barinov, V. B. Kaplan, and S. M. Shkol'nik, in *Proceedings of the All-Russia Scientific Conference on Low-Temperature Plasma, Petrozavodsk, 2004*, Vol. 1, pp. 198–202.

Translated by P. Pozdeev

Strain-Renormalized Energy Spectra of Electrons and Holes in InAs Quantum Dots in the InAs/GaAs Heterosystem

O. O. Dan'kiv and R. M. Peleshchak*

Drogobych State Pedagogical University, Drogobych, Ukraine
* e-mail: peleshchak@rambler.ru
Received April 19, 2005

Abstract—Analytical expressions describing the energy spectrum of electrons and holes are obtained for a quantum dot (QD) occurring in a self-consistent strain field created by an array of coherently stressed QDs. A method of taking into account the lattice mismatch at the QD–matrix interface is proposed that allows for the dependence of the mismatch parameter on the QD size and the matrix layer thickness. It is shown that the internal elastic strain arising at the QD–matrix interface influences the energy spectrum of electrons more significantly than the spectrum of holes. © 2005 Pleiades Publishing, Inc.

For evaluating and controlling the characteristics of semiconductor devices with quantum dots (QDs) and for developing new devices of this type, it is necessary to perform a thorough analysis of the energy spectrum of charge carriers in QDs [1–11]. It is known that the energy spectrum of electron and hole states is significantly influenced by the elastic strain in QDs.

In this study, the energy spectrum of charge carriers in a QD, renormalized as a result of straining of the heterostructure, has been theoretically analyzed within the framework of the effective stress potential model.

A model of the InAs/GaAs heterosystem with coherently strained spherically-symmetric QDs. In order to reduce the many-body problem to an analysis of the system with a single QD, we consider an approximation in which the energy of pair elastic interactions between N QDs is replaced by the energy of interaction of each QD with an averaged (effective) elastic stress field $\sigma_{\text{ef}}(N-1)$ of the other QDs.

Since the lattice parameter of InAs is greater than that of the GaAs matrix, the heteroepitaxial growth of InAs on GaAs within pseudomorphous growth limits is accompanied by the contraction of the InAs lattice and expansion of the GaAs lattice. For this reason, a spherical QD of radius R_0 can be modeled by an elastic dilatation microinclusion in the form of an elastic ball incorporated into a spherical cavity in the GaAs matrix with the initial volume smaller than the microinclusion volume ΔV. In order to incorporate this spherical microinclusion into the matrix, it necessary to contract the QD and to expand the GaAs matrix in radial directions.

Calculation of the electron and hole potential energy in a spherical QD with allowance for elastic straining of the InAs/GaAs heterosystem. Figure 1 presents a schematic diagram of the spherical InAs QD in the GaAs matrix and shows the electron and hole potential energies as functions of the radius r in this

heterosystem. The potential profiles are constructed without (dashed line) and with (solid line) allowance for the straining caused by the lattice mismatch and other differences in characteristics of the QD and matrix materials. As can be seen from Fig. 1, the character of the quantizing potential is determined by the profiles of the conduction band bottom and the valence band top in the InAs/GaAs heterostructure.
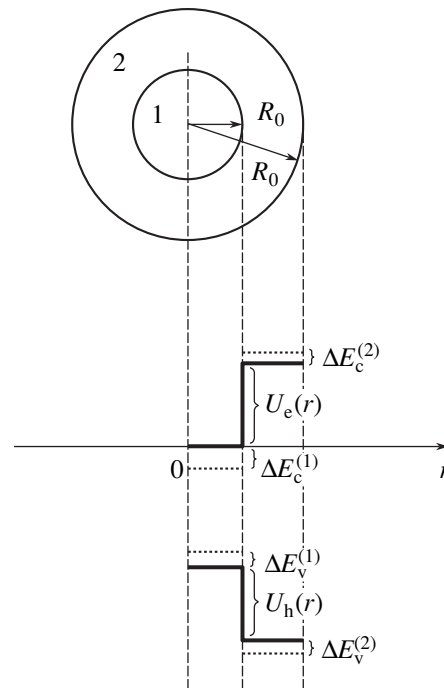
Fig. 1. Schematic diagram of a spherical InAs QD in the GaAs matrix and the electron and hole potential energies as functions of the radius r in the InAs/GaAs heterosystem. Indices (1) and (2) refer to InAs and GaAs, respectively.

The shifts of the edges of both allowed energy bands as a result of elastic straining can be expressed as [12]

$$\Delta E_c^{(i)} = a_c^{(i)} \varepsilon^{(i)}(R_0, R_1); \quad \Delta E_v^{(i)} = a_v^{(i)} \varepsilon^{(i)}(R_0, R_1),$$

where $\varepsilon^{(i)}(R_0, R_1) = \mathrm{Sp}\varepsilon^{(i)}$; $a_c^{(i)}$ and $a_v^{(i)}$ are the hydrostatic strain potential constants of the conduction and valence bands, respectively; and indices $i = 1, 2$ refers to the characteristics of InAs and GaAs, respectively.

The potential energies of electrons and holes in the strained InAs QD in the InAs/GaAs heterosystem depicted in Fig. 1 can be written as

$$U_e(r) = \begin{cases} U_e^{(1)}(r) \\ U_e^{(2)}(r) \end{cases} \tag{1}$$

$$= \begin{cases} 0, & 0 \le r \le R_0, \\ |\Delta U_c(0)| - a_c^{(1)}\varepsilon^{(1)} + a_c^{(2)}\varepsilon^{(2)}, & R_0 \le r \le R_1, \end{cases}$$

$$U_h(r) = \begin{cases} U_h^{(1)}(r) \\ U_h^{(2)}(r) \end{cases} \tag{2}$$

$$= \begin{cases} 0, & 0 \le r \le R_0, \\ |\Delta U_h(0)| - a_v^{(1)}\varepsilon^{(1)} + a_v^{(2)}\varepsilon^{(2)}, & R_0 \le r \le R_1, \end{cases}$$

where $\Delta U_c(0)$ and $\Delta U_h(0)$ are the depths of the potential wells for electrons and holes in the InAs QD in the unstrained InAs/GaAs heterosystem. According to these expressions, the potential energies of charge carriers with allowance for the strain-induced changes can be calculated using the strain tensor components, which depend on the QD radius R_0 and the strained matrix region radius R_1.

In order to determine the required strain tensor components, it is necessary to find the explicit form of radial atomic displacements $u_r^{(1)}$ and $u_r^{(2)}$ in the InAs QD and the surrounding GaAs matrix, respectively. These displacements are described by the equilibrium equation [13],

$$\nabla \mathrm{div}\mathbf{u} = 0 \tag{3}$$

with the following boundary conditions for the spherical QD:

$$\begin{cases} 4\pi R_0^2(u_r^{(2)}|_{r=R_0} - u_r^{(1)}|_{r=R_0}) = \Delta V, & \Delta V = 4\pi R_0^3 f, \\ \sigma_{rr}^{(1)}|_{r=R_0} = \sigma_{rr}^{(2)}|_{r=R_0} + P_L, & P_L = \dfrac{2\alpha}{R_0}, \\ \sigma_{rr}^{(2)}|_{r=R_1} = -\sigma_{ef}(N-1). \end{cases} \tag{4}$$

Here, the left-hand part of the first equation describes the difference ΔV of volumes of the InAs microinclusion and the cavity in the GaAs matrix, R_0 is the QD radius, R_1 is the sum of the QD radius and the GaAs layer thickness, P_L is the Laplace pressure, α is the InAs QD surface energy [14], and f is a parameter reflecting the difference between the lattice parameters (a_1, a_2) and the shear moduli (G_1, G_2) of the InAs nanoparticle and the GaAs nanolayer. In contrast to the approach adopted in [5, 10, 11], the mismatch parameter f in our model is considered as a function of the QD size and the surrounding matrix layer thickness and is expressed as

$$f = f_1 + f_2,$$

where f_1 and f_2 are the relative changes of the QD and matrix lattice parameters caused by the differences of their radial ($a_{rr}^{(i)}$) and angular ($a_{\theta\theta}^{(i)}$, $a_{\varphi\varphi}^{(i)}$) components from the values in the bulk InAs and GaAs.

The mechanical stresses $\sigma_{rr}^{(1)}$ and $\sigma_{rr}^{(2)}$ in InAs and GaAs, respectively, can be expressed as [15]

$$\sigma_{rr}^{(i)} = \frac{E_i}{(1+\nu_i)(1-2\nu_i)} \tag{5}$$
$$\times [(1+\nu_i)\varepsilon_{rr}^{(i)} + \nu_i(\varepsilon_{\varphi\varphi}^{(i)} + \varepsilon_{\Theta\Theta}^{(i)})],$$

where ν_i and E_i are the Poisson ratios and Young's moduli of the QD and matrix materials, which can be expressed in the conventional manner via their elastic constants [15].

For the spherical QD, a solution to Eq. (3) has the following form:

$$u_r^{(1)} = C_1 r + \frac{C_2}{r^2}, \quad 0 \le r \le R_0, \tag{6}$$

$$u_r^{(2)} = C_3 r + \frac{C_4}{r^2}, \quad R_0 \le r \le R_1, \tag{7}$$

where C_1–C_4 are constant parameters. Since the displacement at $r = 0$ must be finite, we put $C_2 = 0$. Once the field of atomic displacements is known, we determine the strain tensor components as
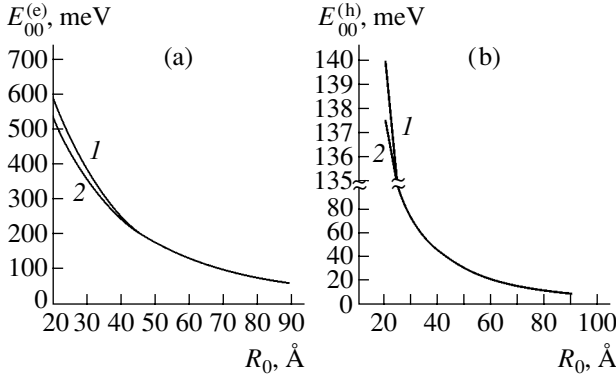
$$\varepsilon_{rr}^{(1)} = C_1, \tag{8}$$

$$\varepsilon_{\varphi\varphi}^{(1)} = \varepsilon_{\Theta\Theta}^{(1)} = C_1, \tag{9}$$

$$\varepsilon_{rr}^{(2)} = C_3 - \frac{2C_4}{r^3}, \tag{10}$$

$$\varepsilon_{\varphi\varphi}^{(2)} = \varepsilon_{\Theta\Theta}^{(2)} = C_3 + \frac{C_4}{r^3}, \tag{11}$$

Fig. 2. Plots of the (a) electron and (b) hole energies in the ground state E_{00} versus QD radius R_0 for the InAs/GaAs heterosystem with $R_1 = 500$ Å, calculated (*1*) without and (*2*) with allowance for the effects of straining.

Fig. 3. Plots of the (a) electron and (b) hole energies in the excited state E_{01} versus QD radius R_0 for the InAs/GaAs heterosystem with $R_1 = 500$ Å, calculated (*1*) without and (*2*) with allowance for the effects of straining.

where the coefficients C_1, C_3, and C_4 are determined from the boundary conditions (4) taking into account relations (5)–(11).

Energy spectra of electrons and holes in an InAs QD in the strained InAs/GaAs heterosystem. The energy spectrum of heavy holes in single crystal InAs is well described within rather broad limits ($E^{(hh)} < 0.4$ eV) using a quadratic approximation. The same approximation can be used to describe the electron energy spectrum, but in a somewhat narrower energy interval [16, 17].

The energy spectra are determined by solving the Schrödinger equation,

$$H_{e, h}\Psi_{e, h}(\mathbf{r}) = E^{(e, h)}\Psi_{e, h}(\mathbf{r}) \quad (12)$$

with the Hamiltonian

$$H_{e, h} = -\frac{\hbar^2}{2}\nabla\frac{1}{m^*_{e, h}(\mathbf{r})}\nabla + U_{e, h}(r, R_0), \quad (13)$$

where $m^*_{e(1, 2)}$ and $m^*_{h(1, 2)}$ are the effective masses of electrons and holes in the QD and in the matrix, respectively, which are assumed to be equal to the values known for the corresponding massive crystals.

A solution to the Schrödinger equation (12) in the spherical coordinate system is expressed as

$$\Psi_{nlm}(r, \Theta, \varphi) = R_{nl}(r)Y_{lm}(\Theta, \varphi), \quad (14)$$

where $Y_{lm}(\Theta, \varphi)$ are the Legendre spherical functions [18] and $R_{nl}(r)$ are the radial functions. The latter quantities

can be expressed in terms of the Bessel spherical functions as [18]

$$R_{1_{nl}}(r) = A j_l(k_{e, h}r) + B n_l(k_{e, h}r), \quad 0 \leq r \leq R_0, \quad (15)$$

$$R_{2_{nl}}(r) = C h_l^{(1)}(i\chi_{e, h}r) + D h_l^{(2)}(i\chi_{e, h}r), \quad R_0 \leq r \leq R_1, \quad (16)$$

where

$$k_{e, h}^2 = \frac{2m^*_{1_{e, h}}}{\hbar^2}E_{nl}^{(e, h)}, \quad \chi_{e, h}^{(2)} = \frac{2m^*_{2_{e, h}}}{\hbar^2}(U_{e, h}^{(2)}(r) - E_{nl}^{(e, h)}), \quad (17)$$

and $U_{e, h}(r)$ are the potential energies of electrons and holes given by formulas (1) and (2), respectively.

The spectrum of energies E_{nl} and the wavefunctions of electrons and holes in QDs of the InAs/GaAs heterosystem are determined from the conditions of continuity for the wavefunctions and the probability flux at the QD–matrix interface,

$$\begin{cases} R_1(r)|_{r = R_0} = R_2(r)|_{r = R_0}, \\ \dfrac{1}{m^*_{(e, h)1}}\dfrac{dR_1(r)}{dr}\bigg|_{r = R_0} = \dfrac{1}{m^*_{(e, h)2}}\dfrac{dR_2(r)}{dr}\bigg|_{r = R_0}, \end{cases} \quad (18)$$

together with the condition of regularity of the radial functions $R_{nl}(r)$ for $r \longrightarrow 0$ and $r \longrightarrow R_1$ and the normalization condition.

Numerical calculations and discussion of results. The energies of the ground and excited states of charge carriers in QDs were numerically calculated as func-

Table 1. Parameters of InAs and GaAs crystals

	a, Å	C_{11}, Mbar	C_{12}, Mbar	a_c, eV	a_v, eV	E_g, eV	m_e/m_0	m_h/m_0	α (110), N/m
InAs	6.08	0.833	0.453	–5.08	1	0.36	0.057	0.41	0.657
GaAs	5.65	1.223	0.571	–7.17	1.16	1.452	0.065	0.45	

Table 2. Effect of matrix straining on the energies of ground and excited electron and hole states in InAs QDs with $R_0 = 40$ Å ($R_1 = 500$ Å)

	$E_{00}^{(e)}$, meV	$E_{00}^{(h)}$, meV	$E_{01}^{(e)}$, meV	$E_{01}^{(h)}$, meV
With neglect of straining	250.31	44.58	496.41	90.84
With allowance for straining	238.69	44.23	467.71	90.09

tions of the QD size R_0 for a nanodimensional InAs/GaAs heterosystem with the parameters presented in Table 1 [14, 19, 20].

Figures 2 and 3 show the (a) electron and (b) hole energies in the ground and excited states plotted versus R_0 for InAs QDs in a GaAs matrix with $R_1 = 500$ Å. As can be seen, an increase in the QD size is accompanied by a monotonic decrease in the electron and hole energy levels, although the potential well depths for both electrons and holes vary in a nonmonotonic manner. As the QD radius increases from 40 to 50 Å (which corresponds to a decrease in the potential well depth by 1.4 and 0.3 meV for electrons and holes, respectively), the energies of electrons and holes decrease in the ground state E_{00} by 68.5 and 14.4 meV and in the excited state E_{01} by 126.5 and 29.3 meV, respectively.

The effect of straining on the energies of electrons and holes in the ground and excited states for InAs QD with $R_0 = 40$ Å in a GaAs matrix with $R_1 = 500$ Å is illustrated by the data in Table 2. As can be seen, the internal elastic strain leads to a decrease in the energy levels of both electrons and holes in InAs QDs in the heterosystem studied.

REFERENCES

1. N. N. Ledentsov, V. M. Ustinov, V. A. Shchukin, *et al.*, Fiz. Tekh. Poluprovodn. (St. Petersburg) **32**, 385 (1998) [Semiconductors **32**, 343 (1998)].
2. A. F. Tsatsul'nikov, B. V. Volovik, D. A. Bedarev, *et al.*, Fiz. Tekh. Poluprovodn. (St. Petersburg) **34**, 330 (2000) [Semiconductors **34**, 323 (2000)].
3. N. A. Maleev, A. E. Zhukov, A. R. Kovsh, *et al.*, Fiz. Tekh. Poluprovodn. (St. Petersburg) **34**, 612 (2000) [Semiconductors **34**, 594 (2000)].
4. V. G. Talalaev, B. V. Novikov, S. Yu. Verbin, *et al.*, Fiz. Tekh. Poluprovodn. (St. Petersburg) **34**, 467 (2000) [Semiconductors **34**, 453 (2000)].
5. V. V. Tishchenko, Y. S. Raptis, E. Anastassakis, and N. V. Bondar, Solid State Commun. **96**, 793 (1995).
6. S. Reimann and M. Manninen, Rev. Mod. Phys. **74**, 1283 (2002).
7. M. V. Tkach, A. M. Makhanets, and G. G. Zegrya, Fiz. Tekh. Poluprovodn. (St. Petersburg) **36**, 543 (2002) [Semiconductors **36**, 511 (2002)].
8. X. F. Wang and X. L. Lei, Phys. Rev. B **49**, 4780 (1994).
9. A. F. Tsatsul'nikov and A. Yu. Egorov, Fiz. Tekh. Poluprovodn. (St. Petersburg) **31**, 851 (1997) [Semiconductors **31**, 722 (1997)].
10. I. A. Ovid'ko and A. G. Sheinerman, Appl. Phys. A **74**, 273 (2002).
11. V. P. Evtikhiev, O. V. Konstantinov, A. V. Matveentsev, and A. E. Romanov, Fiz. Tekh. Poluprovodn. (St. Petersburg) **36**, 79 (2002) [Semiconductors **36**, 74 (2002)].
12. G. L. Bir and G. E. Pikus, *Symmetry and Strain-Induced Effects in Semiconductors* (Nauka, Moscow, 1972; Wiley, New York, 1974).
13. C. Teodosiu, *Elastic Models of Crystal Defects* (Springer-Verlag, Berlin).
14. E. Pehlke and N. Moll, mtrl-th/9607012.
15. L. D. Landau and E. M. Lifshitz, *Course of Theoretical Physics*, Vol. 7: *Theory of Elasticity* (Nauka, Moscow, 1987; Pergamon, New York, 1986).
16. *Landolt-Bornstein New Series III: Crystal and Solid State Physics*, Vol. 22a (Springer-Verlag, Berlin, 1987).
17. J. R. Chelikowsky and M. L. Cohen, Phys. Rev. B **14**, 556 (1976).
18. S. Flugge, *Practical Quantum Mechanics* (Springer-Verlag, Berlin, 1971; Mir, Moscow, 1974).
19. A. Oteish and R. J. Needs, Phys. Rev. B **45**, 1317 (1992).
20. Chris G. Van de Walle, Phys. Rev. B **39**, 1871 (1989).

Translated by P. Pozdeev

Symmetry Analysis of Relative Motions in a Double-Wall Carbon Nanotube

S. S. Savinskiĭ* and A. V. Belosludtsev

Udmurtian State University, Izhevsk, Udmurtia, Russia
*e-mail: savinsky@uni.udm.ru
Received March 18, 2005

Abstract—The binding energy of a double-wall carbon nanotube (DWNT) is theoretically studied as a function of the relative longitudinal shift and relative rotation of the component single-wall carbon nanotubes (SWNTs). It is shown that the binding energy is an oscillating function of the relative shift and rotation, with the oscillation period depending on the relations between symmetry elements of the SWNTs. The results of numerical calculations of the binding energy of DWNTs, performed in the approximation of weak van der Waals interlayer interaction, are presented. © 2005 Pleiades Publishing, Inc.

Carbon nanotubes possess a number of unique properties—such as variable bandgap width (dependent on the tube symmetry) and high strength—which make these objects promising materials for nanoelectronics and nanomechanics. Practical questions related to the use of nanotubes in diodes, transistors, atomic microscope probes, materials for low-voltage electron emitters, etc., are already being actively discussed in the literature (see, e.g., [1–4]).

Recently, Lozovik *et al.* [5] analyzed published data on the potential barrier for the relative shift in double-wall carbon nanotube (DWNTs) and on the force necessary to provide for such a shift (which can significantly vary depending on the ratio of translations in the component single-wall carbon nanotubes (SWNTs)). This study is devoted to a theoretical investigation of the binding energy of a DWNT as a function of the parameters—relative shift and rotation—characterizing the mutual arrangement of the component SWNTs.

Geometrically, an SWNT can be considered as a result of the "gluing" of a ribbon cut from a single graphite plane onto the surface of a cylinder. Figure 1 illustrates the selection of such a ribbon in the graphite plane. In order to identify the ribbon, it is necessary to construct a vector **C** defined in the basis vector set of the unit cell of a two-dimensional atomic lattice of the corresponding graphite plane. The basis vector set of the unit cell on the plane can be selected in different ways. Fig. 1 shows two such vector sets: $\mathbf{a}_1$, $\mathbf{a}_2$ and $\mathbf{a}_3$, $\mathbf{a}_4$. The selected vector **C**, being defined as $\mathbf{C} = i_1\mathbf{a}_1 + i_2\mathbf{a}_2$, determines a pair of SWNT with the chirality indices (i_1, i_2) and a chiral angle φ. The case illustrated in Fig. 1 corresponds to the selection of vector **C** with the chirality indices (12, 4).

When the selected ribbon is "glued" onto the cylinder, the points on the opposite long sides ("banks") of the band (spaced by vector **C**) are considered as identi-

cal. The basis set vectors $\mathbf{a}_1$, $\mathbf{a}_2$ of the graphite plane correspond to screw rotations S_1, S_2 on the tube, respectively; by the same token, vectors $\mathbf{a}_3$, $\mathbf{a}_4$ of the graphite plane correspond to screw rotations S_3, S_4. The basis set vectors $\mathbf{a}_1$, $\mathbf{a}_2$ and $\mathbf{a}_3$, $\mathbf{a}_4$ determine the corresponding unit cells, each containing two carbon atoms. Accordingly, the screw rotations S_1, S_2 and S_3, S_4 determine the unit cells with two carbon atoms on the tube. Use of the screw rotations S_3, S_4 is geometrically more illustrative from the standpoint of the symmetry analysis of carbon nanotubes.

As can be seen from Fig. 1, a carbon nanotube can be considered as a package of atomic rings. Each ring has a rotation symmetry axis C_n, where $n = 1, 2, \ldots$; accordingly, the ring contains n unit cells. For example, the nanotube with the chirality indices (12, 4) shown in Fig. 1 has $n = 4$. The atomic package of an SWNT can be considered to be a result of the action of the operators of screw rotations S_3, S_4 on the unit cell, which leads to a filling of the tube. The rings on the tube are
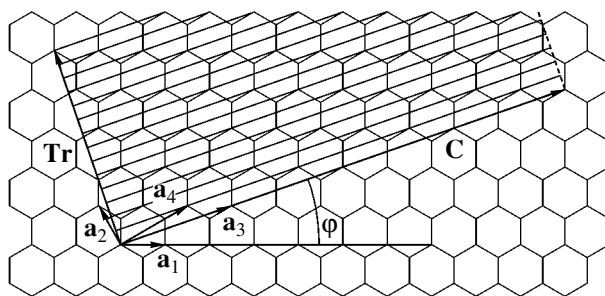
Fig. 1. Schematic diagram of a graphite plane and basis set vectors ($\mathbf{a}_1$, $\mathbf{a}_2$) and ($\mathbf{a}_3$, $\mathbf{a}_4$); **C** is a vector forming a tube with the chirality indices (12, 4); **Tr** is the vector of translation along the nanotube; φ is the chiral angle; parallel lines on the plane correspond to atomic rings on the nanotube.

situated at a fixed distance of Δz and rotated by an angle of $\Delta\varphi$ relative to each other, where the parameters $\Delta\varphi$ and Δz can be geometrically determined from Fig. 1.

The growth of carbon nanotubes leads to the formation not only of SWNTs, but of multiwall nanotubes as well, in which the spacing between layers is approximately the same as that between the planes in a graphite crystal. In what follows we restrict the number of layers to two and consider DWNTs.

Let us consider the possible rotations of SWNTs relative to each other in a DWNT. The position of each tube will be described in terms of angles φ_1 and φ_2. Each angle sets the spatial position of a certain (for definiteness, zeroth) tube cell. As can be readily seen, the binding energy of the two tubes as a function of these angles is a doubly-periodic function of φ_1 and φ_2. This is related to the fact that the rotation of each tube about its symmetry axis does not change their mutual orientation. Accordingly, by expanding the binding energy into the Fourier series, we obtain

$$E_{\mathrm{b}}(\varphi_1, \varphi_2) = \sum_{m_1, m_2} a_{m_1, m_2} \exp(i(m_1 n_1 \varphi_1 + m_2 n_2 \varphi_2)), \tag{1}$$

where the double sum is taken over all possible values of the integers m_1 and m_2; the values of n_1 and n_2 determine the rotation symmetry axes of the component SWNTs. It should be noted that the rotation of the inner tube by an arbitrary angle $\delta\varphi$ is equivalent to the rotation of the outer tube by the angel $-\delta\varphi$, so that $E_{\mathrm{b}}(\varphi_1 + \delta\varphi, \varphi_2) = E_{\mathrm{b}}(\varphi_1, \varphi_2 - \delta\varphi)$. This condition in (1) implies that the Fourier coefficients $a_{m_1, m_2} \neq 0$ for $m_1 n_1 = -m_2 n_2$, which reduces the double sum in (1) to a single sum. If the indices n_1, n_2 have no common divisors, then the binding energy (1) is a periodic function, with a period of $\dfrac{2\pi}{n_1 n_2}$ with respect to the difference of arguments. In the case where n_1, n_2 have a common divisor g, the binding energy (1) can be rewritten as

$$E_{\mathrm{b}}(\varphi_1, \varphi_2) = \sum_{m} a_m \exp\left(im\frac{n_1 n_2}{g}(\varphi_1 - \varphi_2)\right), \tag{2}$$

where the sum is taken over integers m.

Let us consider the possible shifts of SWNTs relative to each other in a DWNT. The position of each SWNT in space is defined by the values of z_1, z_2, whereby each parameter sets the spatial position of a certain (for definiteness, zeroth) tube cell. As can be readily seen, the binding energy of the two tubes as a function of these parameters is a doubly-periodic function

tion with the periods equal to the translations along each tube:

$$E_{\mathrm{b}}(z_1, z_2) = \sum_{q_1, q_2} a_{q_1, q_2} \exp(i(q_1 z_1 + q_2 z_2)), \tag{3}$$

where $q_1 = 0, \pm\dfrac{2\pi}{\mathrm{Tr}_1}, \pm\dfrac{4\pi}{\mathrm{Tr}_1} \pm \dfrac{6\pi}{\mathrm{Tr}_1}, \ldots; q_2 = 0, \pm\dfrac{2\pi}{\mathrm{Tr}_2},$ $\pm\dfrac{4\pi}{\mathrm{Tr}_2} \pm \dfrac{6\pi}{\mathrm{Tr}_2}, \ldots;$ and Tr_1 and Tr_2 are the values of translations for the inner and outer tubes, respectively. It should be noted that a shift of the inner tube by an arbitrary value of δz is equivalent to a shift of the outer tube by the value of $-\delta z$, so that $E_{\mathrm{b}}(z_1 + \delta z, z_2) = E_b(z_1, z_2 - \delta z)$. This condition in (3) implies that the Fourier coefficients $a_{q_1, q_2} \neq 0$ for $q_1 = -q_2$, which reduces the double sum in (3) to the following single sum

$$E_{\mathrm{b}}(z_1, z_2) = \sum_{q} a_q \exp(iq(z_1 - z_2)), \tag{4}$$

where the summation is performed over all q such that $q = q_1 = -q_2$.

It should also be noted that, if the ratio of translations of the SWNTs is an irrational number, the sum (4) contains a single term with $q_0 = 0$. This means that the binding energy is independent of the parameters z_1 and z_2 and is a constant quantity. Theoretically, this implies that the two tubes can be considered as a longitudinal slide nanobearing.

Let us consider the general case of an arbitrary variation of the spatial arrangement of the component tubes, including the shifts and rotations. In a simple variant, the binding energy can be represented as a product of the functions from the right-hand parts of Eqs. (2) and (4). Accordingly, an expression for the binding energy can be written as

$$E_{\mathrm{b}}(\varphi_1, z_1; \varphi_2, z_2)$$
$$= \sum_{m, q} a_{m, q} \exp\left(im\frac{n_1 n_2}{g}(\varphi_1 - \varphi_2) + iq(z_1 - z_2)\right). \tag{5}$$

We have performed numerical calculations for the interaction of tubes performing relative motions (rotations and longitudinal shifts). The pair interaction energy for atoms belonging to different tubes was described in terms of the Lennard-Jones "6–12" potential,

$$U(r) = -\frac{C_6}{r^6} + \frac{C_{12}}{r^{12}},$$

with the fitting parameters $C_6 = 20$ eV Å^6 and $C_{12} = 2.488 \times 10^4$ eV Å^{12} [6]. The total binding energy of the DWNT was calculated as the sum of the pair interaction energies of atoms belonging to different SWNTs for fixed rigid atomic geometries of both tubes. The results of these numerical calculations are presented in Fig. 2.

Figure 2a shows the curves of the DWNT binding energy as a function of the relative rotation angle. Here, curve *1* is constructed for SWNTs with the chirality indices (10, 1) and (19, 1). These tubes possess rotation symmetry axes of the first order ($n_1 = n_2 = 1$), and the binding energy is a periodic function with respect to the relative rotation angle with a period of 2π. Curve *2* in Fig. 2a corresponds to the case of two SWNTs of like chirality with the indices (10, 2) and (20, 4). These tubes possess rotation symmetry axes of the second and fourth order ($n_1 = 2$, $n_2 = 4$) and have a common divisor $g = 2$. According to formula (2), the period of the binding energy with respect to the relative rotation angle in this case is $\frac{\pi}{2}$. Curve *3* in Fig. 2a corresponds to SWNTs with the indices (10, 0) and (19, 1). Here, one of the tubes possesses a rotation symmetry axis of the tenth order and the other—of the first order; according to formula (2), the period of the binding energy with respect to the relative rotation angle in this case is $\frac{\pi}{5}$. Finally, curve *4* in Fig. 2a shows the case of SWNTs with the chirality indices (10, 0) and (19, 0). These tubes possess rotation symmetry axes of the tenth and nineteenth order, respectively. The binding energy appears as a rapidly oscillating function of relatively small amplitude with a period of $\frac{2\pi}{190}$. The latter example shows that a system of SWNTs with the chirality indices (10, 0) and (19, 0) can be used as an antifriction nanobearing.

The curves in Fig. 2a exhibit an oscillatory character, with the amplitude varying within a broad range: the relative amplitude decreases by one order of magnitude on the passage from curve *1* to the curves *2* and *3*, and then it decreases by one more order of magnitude on the passage to curve *4*.

Figure 2b presents the results of numerical calculations of the binding energy of DWNTs as a function of their relative shift. The characteristic SWNT lengths in these calculations were 200 Å for the inner tube and 40 Å for the outer tube. For the SWNT pair with the indices (10, 2) and (20, 4), the translations for both tubes are the same and are equal to Tr = 6.52 Å. For another pair of SWNTs with the indices (16, 6) and (22, 0) (see Fig. 2b), the translations are Tr_1 = 29.862 Å and Tr_2 = 4.266 Å, respectively, so that the common translation is 29.862 Å.

Thus, a DWNT can be considered either as a nanomechanical system that can be used to obtain slide and antifriction nanobearings, or as a molecular mechanism possessing nonlinear elastic properties with respect to the relative rotation and shift of the component SWNTs.

Restricting consideration to weak van der Waals interactions and taking into consideration only interactions between the adjacent component SWNTs in a
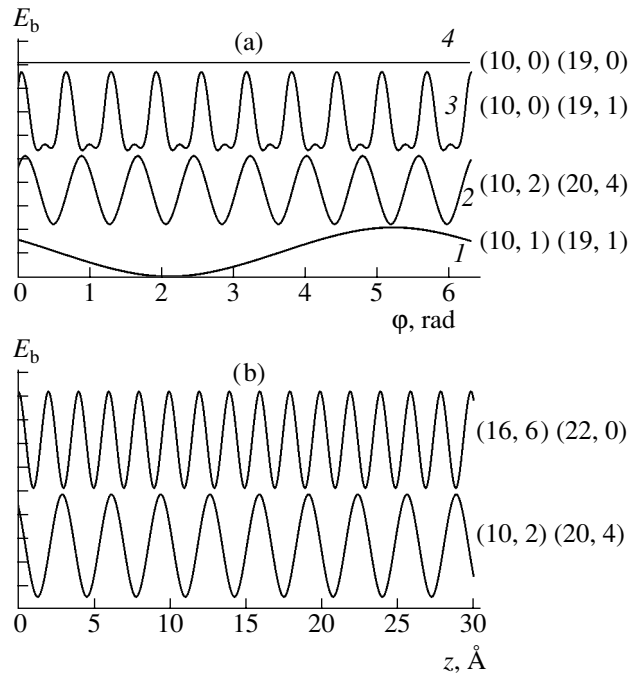
Fig. 2. The results of numerical calculations of the binding energy (plotted in relative units) for various DWNTs (a) as a function of the mutual rotation angle and (b) as the relative longitudinal shift of the component SWNTs (see the text for explanations).

multiwall carbon nanotube, the relative shifts and rotations in such nanotubes can also be analyzed using the method proposed in this paper. In this analysis, the binding energy of the multiwall nanotube is considered as a sum of additive contributions due to adjacent SWNT pairs:

$$E_b(\varphi_1, z_1; \varphi_2, z_2; \dots \varphi_N, z_N)$$
$$= E_b(\varphi_1, z_1; \varphi_2, z_2) + E_b(\varphi_2, z_2; \varphi_3, z_3) \quad (6)$$
$$+ E_b(\varphi_3, z_3; \varphi_4, z_4) + \dots + E_b(\varphi_{N-1}, z_{N-1}; \varphi_N, z_N),$$

where N is the number of SWNTs in the multiwall structure.

REFERENCES

1. A. V. Eletskiĭ, Usp. Fiz. Nauk **172**, 401 (2002) [Phys. Usp. **45**, 369 (2002)].

2. A. Phaeton, Acc. Chem. Res. **35**, 1026 (2002).

3. David S. Y. Hsu, Appl. Phys. Lett. **80**, 2988 (2002).

4. C. Journet and P. Bernier, Appl. Phys. A **67**, 2003 (1998).

5. Yu. E. Lozovik, A. M. Popov, and A. V. Belikov, Fiz. Tverd. Tela (St. Petersburg) **45**, 1333 (2003) [Phys. Solid State **45**, 1396 (2003)].

6. L. A. Girifalco, Phys. Rev. B **62**, 13104 (2000).

Translated by P. Pozdeev

Effect of Electron Irradiation on the Photopleochroism of ZnO/CdS/Cu(In,Ga)Se$_2$ Solar Cells

B. Kh. Baĭramov, Yu. A. Nikolaev, V. Yu. Rud', Yu. V. Rud',
E. I. Terukov, and M. V. Yakushev

Ioffe Physicotechnical Institute, Russian Academy of Sciences, St. Petersburg, 194021 Russia

St. Petersburg State Technical University, St. Petersburg, 195251 Russia

Strathclyde University, G 40 NG, United Kingdom

e-mail: rudvas@spbstu.ru

Received April 20, 2005

Abstract—The effect of irradiation with 1-MeV electrons to various doses on the photosensitivity of ZnO/CdS/Cu(In,Ga)Se$_2$ solar cells and related CdS/Cu(In,Ga)Se$_2$ and ZnO/Cu(In,Ga)Se$_2$ heterostructures has been studied. Both the photoconversion efficiency and the coefficient of induced photopleochroism of ZnO/CdS/CIGS solar cells remained practically unchanged upon irradiation up to a total dose of 10^{-17} cm^{-2}. It is suggested that the method of polarization photoelectric spectroscopy can be used for evaluating the effect of electron irradiation on the photosensitivity of semiconductor photoconverters. © *2005 Pleiades Publishing, Inc.*

Investigations into the physicochemical properties of a broad class of diamondlike semiconductors, the rules of formation for which were originally formulated by Goryunova [1], provided a large group of new materials interesting for the physics and promising for the technology of semiconductors and led eventually to the creation of some novel types of semiconductor devices. The discovery of semiconductor properties in A^{III}B^V compounds favored the formulation of new concepts in the physics of semiconductors and stimulated the development of highly efficient heterolasers, heterophotocells, etc. [2]. The first investigations of the ternary analogs of binary semiconductors led to the synthesis of new direct-gap materials, the discovery of photopleochroism, the attainment of record nonlinear susceptibility, creation of thin-film radiation-resistant solar cells with a record high quantum efficiency of photoconversion, etc. [3–7]. All these achievements confirmed that the study of diamondlike semiconductor phases with increasing complexity of atomic composition is a fruitful direction of research [1–3].

In continuation of the research in this promising direction, we have studied for the first time the effect of electron irradiation on the induced photopleochroism in thin-film polycrystalline solar cells based on quaternary Cu(In,Ga)Se$_2$ solid solutions with a crystal lattice structure of the chalcopyrite type.

Sample preparation and characterization. Polycrystalline films of a CuIn$_{0.9}$Ga$_{0.1}$Se$_2$ (CIGS) solid solution with a thickness of $d_1 = 2$ μm were obtained by codeposition of the component elements (Cu, In, Ga, and Se) onto the surface of molybdenum-coated ($d_2 =$

1 μm) soda-ash glass substrates. Then, a CdS film ($d_3 = 50$ nm) was grown by chemical vapor deposition onto the post-growth homogeneous CIGS film surface, and a ZnO layer was deposited by magnetron sputtering onto the CdS film. This layer was not doped intentionally over a thickness of $d_4 = 50$ nm, while subsequent growth was accompanied by doping with aluminum. At the final stage of the solar cell fabrication, a current collector grid of pure aluminum was formed on the ZnO:Al film surface by thermal evaporation and deposition in vacuum via a mask. The obtained ZnO/CdS/CIGS solar cells in the initial state were characterized by the quantum efficiency $\eta^{in} \approx$ 13–14% (AM, 1.5) and the open-circuit voltage $U^{in} \approx 620$ mV at $T = 300$ K.

In addition to the complete ZnO/CdS/CIGS heterostructures, we have also grown and studied the related photosensitive ZnO/CIGS and CdS/CIGS structures representing pair combinations of layers entering into the solar cell. Investigations of such heterojunctions can provide useful data from the standpoint of the optimization of the parameters of ZnO/CdS/CIGS solar cells.

The obtained heterostructures were irradiated on an electron accelerator in air at room temperature with high-energy (1 MeV) electrons to doses within $D \approx 10^{16}$–10^{17} cm^{-2}. Before and after exposure, the samples were characterized by photoelectric parameters. The spectra of the relative quantum efficiency of photoconversion $\eta(\hbar\omega)$ were measured in natural and linearly polarized light. The induced photopleochroism coefficient P_I was measured either as a function of the light
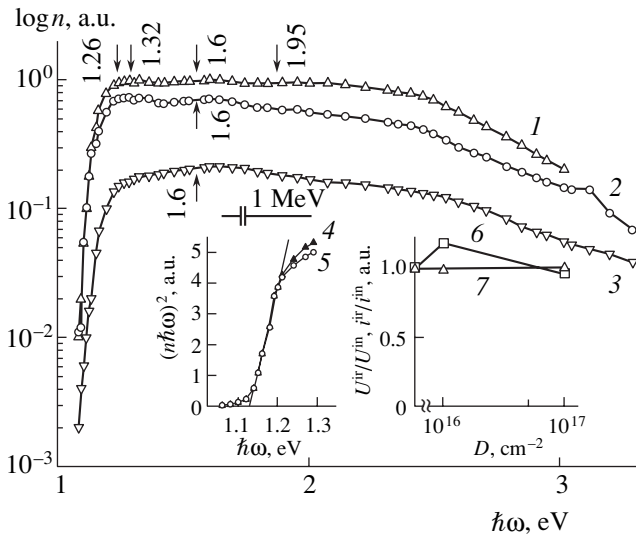
Fig. 1. Spectral dependences of the relative quantum efficiency of photoconversion for (*1*, *2*) ZnO/CdS/CIGS solar cells (*1*) before and (*2*) after electron irradiation to a dose of $D = 10^{17}$ cm^{-2} and (*3*) unirradiated ZnO/CIGS structures measured using unpolarized light at $T = 300$ K. Arrows indicate the energy positions of local maxima ($\hbar\omega^m$, eV; see table). The inset shows the $(\eta\hbar\omega)^2 = f(\hbar\omega)$ curves (*4*) before and (*5*) after electron irradiation to a dose of $D = 10^{17}$ cm^{-2} and the dose dependences of the relative (*6*) open-circuit voltage and (*7*) short-circuit current for ZnO/CdS/CIGS solar cells irradiated with 1-MeV electrons at $T = 300$ K.
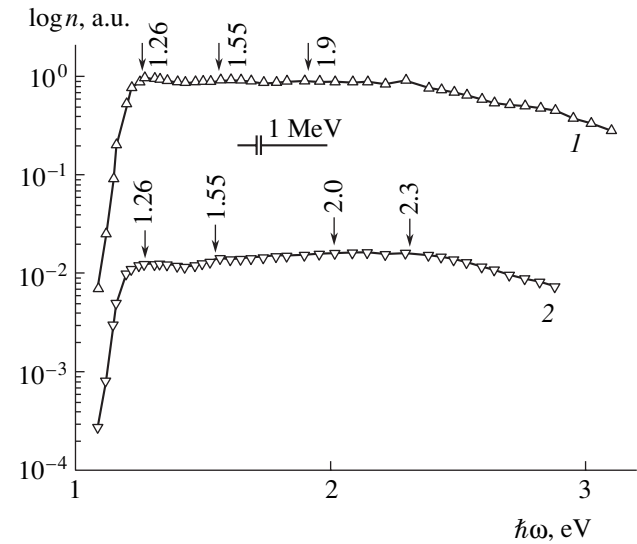
Fig. 2. Spectral dependences of the relative quantum efficiency of photoconversion for CdS/CIGS structures (*1*) before and (*2*) after electron irradiation to a dose of $D = 10^{17}$ cm^{-2}, measured using unpolarized light at $T = 300$ K. Arrows indicate the energy positions of local maxima ($\hbar\omega^m$, eV; see table).

incidence angle Θ at a fixed photon energy $\hbar\omega$ or as a function of $\hbar\omega$ at Θ = const.

Results and Discussion

Photoconversion efficiency. Figures 1 and 2 show the typical curves of $\eta(\hbar\omega)$ determined as the ratio of the short-circuit current to the number of incident photons in the initial state (i^{in}) and after irradiation (i^{ir}) with 1-MeV electrons. Some characteristics of photosensitivity of the structures studied are presented in the table. The main results of our experiments are as follows.

A comparative analysis of the results of photoconversion efficiency measurements for various thin-film structures studied (see Figs. 1 and 2) showed that their $\eta(\hbar\omega)$ curves have similar shapes, which are retained upon the electron irradiations up to doses $D \approx 10^{17}$ cm^{-2}.

Indeed, the onset of the exponential growth of η in all samples was observed at similar photon energies $\hbar\omega \approx$ 1.08 eV and was characterized by the typical high slope $S = \Delta\ln\eta/\Delta(\hbar\omega) \approx 50$–110 eV^{-1} (characteristic of direct interband transitions). The maximum S values were usually observed for the ZnO/CdS/CIGS solar cells (see table). The decrease in the slope on the passage to ZnO/CIGS and CdS/CIGS structures is probably indicative of a certain smearing of free-electron band edges and an increasing role of transitions between tails of the density of states.

It should also be emphasized that, despite significant differences in the structure of samples studied, the long-wavelength edge of $\eta(\hbar\omega)$ obeyed a relation that is characteristic of direct interband transitions [8]:

$$\eta\hbar\omega = A(E_g - \hbar\omega)^{1/2}, \qquad (1)$$

where A is a constant factor and E_g is the bandgap width. Extrapolation of the obtained data to $(\eta\hbar\omega)^2 \longrightarrow 0$ for all the photosensitive structures based on the quaternary CIGS solid solution gave similar values of the

Photoelectric properties of Cu(In,Ga)Se$_2$ thin-film structures at $T = 300$ K

Sample structure	D, cm^{-2}	$\hbar\omega^m$, eV	δ, eV	S, eV^{-1}	E_g, eV	P_I, % ($\Theta \approx 70°$)
ZnO/CdS/CIGS	0	1.26; 1.6	1.46	115	1.13	
	10^{17}	1.26; 1.6	1.38	110	1.13	
CdS/CIGS	0	1.26; 1.6	1.66	46	1.15	11
	10^{17}	1.26; 1.55	1.66	58	1.13	10
ZnO/CIGS	0	1.6	1.46	50	1.13	
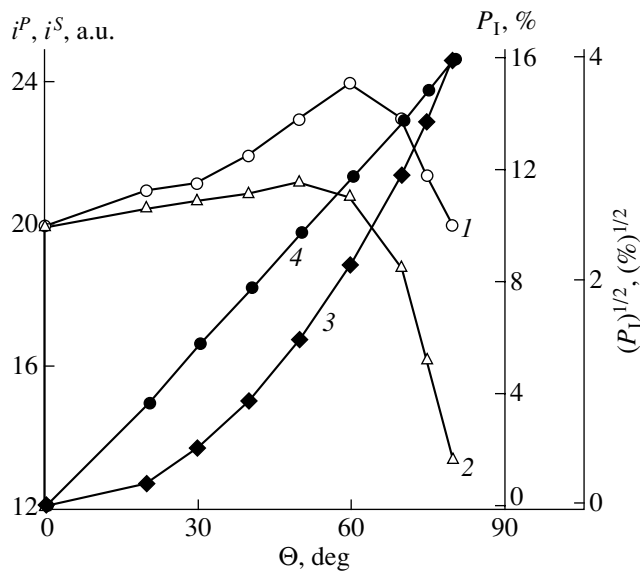
Fig. 3. The typical curves of photocurrents (*1*) i^P and (*2*) i^S and the induced photopleochroism coefficient (*3*) P_I and

(*4*) $P_\mathrm{I}^{1/2}$ as functions of the angle Θ of LP light incidence onto the working plane of a ZnO/CdS/CIGS solar cell irradiated with 1-MeV electrons ($D = 10^{17}$ cm^{-2}). The measurements were performed at $T = 300$ K using the light with $\hbar\omega = 2.07$ eV.

bandgap width: $E_\mathrm{g} \approx 1.13$ eV at $T = 300$ K both before and after electron irradiation (see table and the inset to Fig. 1, curves *4* and *5*). This E_g value agrees with the data on the optical absorption in CIGS films. On this ground, the long-wavelength edge observed in the $\eta(\hbar\omega)$ spectra of the structures studied before and after the irradiation (Figs. 1 and 2) can be related to the interband absorption in CIGS films of identical atomic composition.

Another feature in common for the heterostructures based on CIGS films is the large width of their photosensitivity spectra (Figs. 1 and 2). It should be noted that, despite the electron irradiation and the difference in type of the structure, the energy positions of maxima ($\hbar\omega^\mathrm{m}$) in the photosensitivity spectra (indicated by arrows in Figs. 1 and 2 and presented in the table) are well reproduced, and the photosensitivity level is retained on a high level in a broad range of photon energies.

The table gives the values of the full width at half maximum δ for the observed photosensitivity spectra. These values are also quite large and very close to each other for the structures of various types measured both before and after irradiation. This result is evidence for a rather high quality of interfaces and their stability under electron irradiation to high doses, at least at the level of $D = 10^{17}$ cm^{-2}. It should be emphasized that the short-wavelength decay in $\eta(\hbar\omega)$ of the ZnO/CdS/CIGS and CdS/CIGS structures (Fig. 1, curves *1* and *2*) is not enhanced upon the electron irradiation. Moreover, in

the latter case this edge even significantly shifts toward shorter wavelengths (Fig. 2, curve *2*), which indicates that the electron irradiation has no negative effect on the interface quality.

Data on the dose dependence of the open-circuit voltage and short-circuit current (normalized to their initial values for unirradiated samples) in ZnO/CdS/CIGS solar cells (see the inset to Fig. 1, curves *6* and *7*) confirmed a high radiation resistance of these structures up to doses at the level of $D = 10^{17}$ cm^{-2}, in agreement with published data [5–7]. On the passage to the CdS/CIGS structure, both the open-circuit voltage and short-circuit current significantly decrease in the range of electron irradiation doses from 10^{16} to 10^{17} cm^{-2}. For example, $U^\mathrm{ir}/U^\mathrm{in} \approx 0.68$ and $i^\mathrm{ir}/i^\mathrm{in} \approx 0.1$ for $D = 10^{17}$ cm^{-2}. This result confirms the importance of the introduction of a ZnO layer in the solar cell structure, which eliminated the undesired degradation of photosensitivity under the action of high-energy electrons.

Photopleochroism. The illumination of strongly electron-irradiated ZnO/CdS/CIGS solar cells by linearly polarized (LP) light showed that the photocurrent in the entire range of photosensitivity depends on the spatial orientation of the electric field vector **E** in the light wave, provided that the angle of light incidence Θ (measured from the normal direction) is nonzero (Fig. 3). If the solar cell is illuminated by LP light along the normal, the photocurrent is insensitive to the azimuthal angel φ between **E** and the plane of light incidence, which is related to isotropic optical absorption of the polycrystalline ZnO, CdS, and CIGS films forming the heterojunctions. In the case of oblique incidence ($\Theta \neq 0$) of the LP light beam, the photocurrent measured as a function of φ exhibits periodic variations and obeys the relation

$$i_\varphi = i^P \cos^2\varphi + i^S \sin^2\varphi, \qquad (2)$$

where i^P and i^S are the photocurrent values corresponding to the vector **E** oriented parallel and perpendicularly to the plane of light incidence.

Figure 3 shows the typical curves of photocurrents i^P and i^S and the induced photopleochroism coefficient P_I as functions of the LP light incidence angle Θ. The main features of these angular dependences are as follows. First, the photocurrents i^P and i^S exhibit a maximum in the vicinity of $\Theta = 60°$ (Fig. 3, curves *1* and *2*), which is indicative of a simultaneous decrease in the reflection losses for both *P* and *S* polarizations of the incident light. It should be pointed out that the experimental behavior of $i^P(\Theta)$ agrees with that expected on the basis of analysis of the LP light transmission through the air–ZnO interface, whereas the observed behavior of $i^S(\Theta)$ differs from that predicted by the theory [9, 10]. Second, the experimental angular dependence of the photopleochroism coefficient obeys the quadratic law $P_\mathrm{I} \sim (\Theta)^2$ (Fig. 3, curves *3* and *4*) in agree-
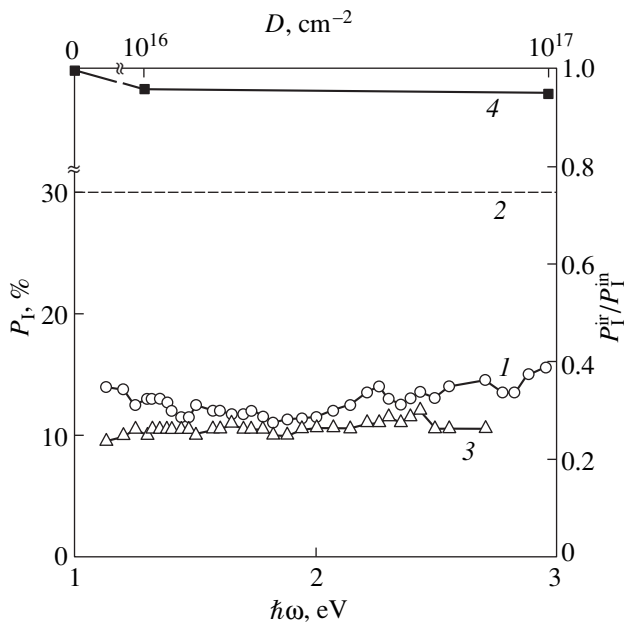
Fig. 4. Induced photopleochroism of ZnO/CdS/CIGS solar cells: (*1*, *3*) experimental spectral dependences of the coefficient P_I measured at $T = 300$ K and $\Theta = 70°$ before and after electron irradiation to a dose of $D = 10^{17}$ cm^{-2}, respectively; (*2*) theoretical spectral dependence for the unirradiated solar cell [11]; (*4*) dose dependence of the coefficient P_I measured at $T = 300$ K, $\hbar\omega = 2.0$ eV, and $\Theta = 70°$.

will make it possible to exceed the existing record level of quantum efficiency for such photoconverters.

To summarize, we have studied the photosensitivity of ZnO/CdS/CIGS solar cells and related CdS/CIGS and ZnO/CIGS heterostructures using both natural and linearly polarized light and have determined the dependence of the photoelectric characteristics of such cells on the dose of irradiation with 1-MeV electrons. It is established that both the photoconversion efficiency and the coefficient of induced photopleochroism of ZnO/CdS/CIGS solar cells remained practically unchanged upon irradiation up to a total dose of 10^{17} cm^{-2}. These results suggest that it is possible to use the phenomenon of photopleochroism for evaluating the effect of electron irradiation on the properties of semiconductor photoconverters.

ment with [11], and P_I measured at $\Theta = $ const remains virtually unchanged in the entire photosensitivity range.

Figure 4 (curves *1* and *3*) shows the typical spectra of the coefficient of induced photopleochroism measured for a ZnO/CdS/CIGS solar cell at $\Theta = 70°$ before and after electron irradiation. As can also be seen from the obtained experimental data, the P_I value of the samples irradiated with increasing doses of 1-MeV electrons (up to $D = 10^{17}$ cm^{-2}) remains virtually constant (Fig. 4, curve *4*), in agreement with the dose dependences of the photoelectric parameters of such cells measured using unpolarized light (see the inset to Fig. 1, curves *6* and *7*). On the other hand, a decrease in the experimental values of the induced photopleochroism relative to its theoretical estimate for the air–ZnO interface [11] (Fig. 4, line *2*) is indicative of a reduction in the losses for reflection in the obtained ZnO/CdS/CIGS structures in the entire spectral range of high photosensitivity [11, 12].

The experimental $P_I(\hbar\omega)$ spectra also point to the good prospects for further increase in the photoconversion efficiency of ZnO/CdS/CIGS solar cells, which can be achieved through optimization of the parameters of antireflection coatings. The quality of such coatings can be directly monitored by means of polarization photoelectric spectroscopy in the spectral region of maximum photosensitivity [11, 12]. This optimization

REFERENCES

1. N. A. Goryunova, *Compound Diamond-Like Semiconductors* (Sov. Radio, Moscow, 1968) [in Russian].
2. Zh. I. Alferov and B. V. Tsarenkov, Fiz. Tekh. Poluprovodn. (Leningrad) **19**, 2113 (1985) [Sov. Phys. Semicond. **19**, 1303 (1985)].
3. V. D. Prochukhan and Yu. V. Rud', Fiz. Tekh. Poluprovodn. (Leningrad) **12**, 209 (1978) [Sov. Phys. Semicond. **12**, 121 (1978)].
4. Yu. V. Rud', Izv. Vyssh. Uchebn. Zaved., Fiz., No. 8, 68 (1986).
5. O. Lundberg, M. Edoff, and L. Stolt, in *Proceedings of the ISES Solar World Congress, Goteborg, 2003*, p. 57.
6. A. Jasenek and U. Rau, J. Appl. Phys. **90**, 650 (2001).
7. A. Jasenek, U. Rau, K. Weinert, *et al.*, Thin Solid Films **387**, 228 (2001).
8. S. Sze, *Physics of Semiconductor Devices* (Wiley, New York, 1981).
9. G. S. Landsberg, *Optics* (Nauka, Moscow, 1976) [in Russian].
10. R. M. Azzam and N. M. Bashara, *Ellipsometry and Polarized Light* (North-Holland, Amsterdam, 1977).
11. F. P. Kesamanly, V. Yu. Rud', and Yu. V. Rud', Fiz. Tekh. Poluprovodn. (St. Petersburg) **33**, 512 (1999) [Semiconductors **33**, 483 (1999)].
12. V. Yu. Rud', Yu. V. Rud', and V. P. Khvostikov, Fiz. Tekh. Poluprovodn. (St. Petersburg) **33**, 747 (1999) [Semiconductors **33**, 689 (1999)].

Translated by P. Pozdeev

Nonlinear Optical Properties of Gold Nanoparticles Synthesized by Ion Implantation in Sapphire Matrix

A. L. Stepanov[a,b,*], C. Marques[c,d], E. Alves[c,d], R. C. da Silva[c,d],
M. R. Silva[c,d], R. A. Ganeev[e], A. I. Ryasnyansky[e], and T. Usmanov[e]

[a] *Institute for Experimental Physics and the Erwin Schrödinger Institute for Nanoscale Research,*
Karl-Franzens-University, A-8010 Graz, Austria

[b] *Kazan Physicotechnical Institute, Russian Academy of Sciences,*
Kazan, Tatarstan, 420029 Russia

[c] *Dep. Fisica, Instituto Technólogico e Nuclear, E.N. 10, 2695-953 Sacavém, Portugal*

[d] *CFN, Universidade de Lisboa, Av. Prof. Gama Pinto 2, 1649-003 Lisboa, Portugal*

[e] *NPO Akadempribor, Academy of Sciences of Uzbekistan, Tashkent, 700125 Uzbekistan*

* e-mail: andrey.stepanov@uni-graz.at; anstep@kfti.knc.ru

Received February 18, 2005

Abstract—Single crystal Al_2O_3 substrates have been implanted with 160-keV Au^+ to a dose of 0.6×10^{17} or 1.0×10^{17} cm^{-2}, with a postimplantation annealing for 1 h at 800°C in air. The obtained composite layers were studied by the method of linear optical reflection; the nonlinear optical characteristics were determined by the *RZ*-scan technique using picosecond radiation pulses of an Nd:YAG laser operating at 1064 nm. The appearance of a characteristic surface optical plasmon resonance band in the linear reflection spectra was indicative of the formation of gold nanoparticles in a subsurface layer of ion-irradiated Al_2O_3. It is shown that the synthesized particles are responsible for the observed manifestations of nonlinear refraction. The composite layers were characterized by the nonlinear refractive index (n_2) and the real part of the third-order nonlinear susceptibility ($\mathrm{Re}\chi^{(3)}$). © *2005 Pleiades Publishing, Inc.*

Composite materials based on dielectric matrices containing dispersed metal nanoparticles are promising materials for optoelectronics and nonlinear optics. The phenomenon of the collective excitation of conduction electrons in such nanoparticles under the action of electromagnetic (light) waves and the subsequent enhancement of the local field stimulate various optical resonance phenomena in a broad spectral range [1–3]. Such effects can be used in nonlinear optical switches and limiters—key elements of dielectric waveguide conductors—capable of providing optical signal conversion at short (pico- or femtosecond) laser pulse durations. Promising optical waveguides for modern optoelectronic devices are offered by a heat-resistant layer of synthetic sapphire (Al_2O_3) deposited onto the surface or integrated into bulk of semiconductor substrates. In this context, it was of interest to study the optical properties of metal nanoparticles formed in this matrix, for example, by means of ion implantation [2, 3].

From the standpoint of the realization of nonlinear optical properties, the most promising implants are the metals with a high density of free conduction electrons, in particular, gold [1, 3]. According to the available published data, the synthesis of gold particles in sapphire by means of ion implantation was originally performed in 1988 [4], but a preliminary analysis of the nonlinear optical properties of such implanted layers was only reported in [5]. At the same time, the nonlinear optical properties were studied for Al_2O_3 matrices with gold particles formed by different methods [6, 7]. It should be noted that all the previous investigations of the optical properties of composites were restricted to the visible spectral range, that is, to wavelengths in the vicinity of the surface plasmon resonance (SPR) in metal nanoparticles [1].

We have studied the possibility of using Al_2O_3 with gold nanoparticles synthesized by ion implantation as a new nonlinear optical material for applications in the near infrared (NIR) spectral range. Interest in the nonlinear optical characteristics—in particular, the nonlinear optical refraction manifestations in metal nanoparticles in Al_2O_3—in the NIR range is related to practical applications in the field of telecommunications.

A composite material was obtained using single crystal $Al_2O_3(0001)$ substrates. These matrices were implanted with 160-keV Au^+ ions to a dose of 0.6×10^{17} cm^{-2} (samples 1 and 2) and 1×10^{17} cm^{-2} (samples 3 and 4) at a fixed ion beam current of 10 $\mu A/cm^2$. Following the ion implantation stage, samples 2 and 4

were annealed for 1 h at 800°C in air. The linear optical reflection spectra were measured using a Perkin-Elmer Lambda 19 double-beam spectrophotometer. The optical extinction spectra were simulated within the framework of the classical theory of interaction between electromagnetic waves and a spherical particle (Mie's theory), using a method described elsewhere [8]. The nonlinear optical refraction of the composite samples was determined by measuring normalized reflection $R(Z)$ on an RZ-scan setup [9–11]. Using this setup, it was possible to measure n_2 in a sample irrespective of the possible nonlinear absorption. The measurements were performed using radiation of an Nd:YAG laser with a wavelength of 1064 nm, a pulse duration of 55 ps, and a maximum laser beam intensity of 7×10^9 W/cm^2 in the focal spot.

Figure 1 shows the experimental optical reflection spectra of the initial Al_2O_3 matrix and the spectra of implanted sapphire with and without postimplantation annealing. In contrast to the initial matrix, all implanted materials are characterized by the presence of a broad selective band with a maximum at ~610 nm in the reflection spectrum. This band is direct evidence of the formation of isolated (not interacting with each other) gold particles in Al_2O_3. The appearance of this band is related to the SPR in metal nanoparticles [1, 2]. For comparison, Fig. 1 also shows a model spectrum of the extinction cross section calculated for a spherical gold particle with a diameter of 15 nm in the Al_2O_3 matrix, which exhibits a maximum in the same spectral interval. Thus, the model calculations confirm the formation of gold particles in the sapphire matrix.

As can be seen from a comparison of the optical spectra of samples 1 and 3 (Fig. 1), which were obtained by ion implantation to different doses, an increase in the ion dose leads to a significant growth in the intensity of reflection (from 35 to 50%) and to a shift of the SPR maximum to ~620 nm for sample 3. Apparently, these changes in the reflection spectra are related to an increase in the concentration of gold incorporated into the matrix. The implantation of a greater number of Au$^+$ ions into the target leads to the formation of greater gold inclusions and to their wider spread in dimensions, which is reflected by increasing reflection intensity in the NIR range [2, 8].

The additional thermal treatment (postimplantation annealing) of implanted samples virtually did not influence the positions of maxima of the SPR bands observed in the samples upon implantation. However, the annealed samples exhibited a sharp increase in the intensity of reflection in the log-wavelength (NIR) range. This change is especially pronounced for sample 2 in the region of 800 nm, where an additional maximum appears even exceeding in intensity the reflection band (~610 nm). The appearance of this maximum or a broad intense shoulder on the reflection band (for sample 4) can be explained by spectral changes caused by
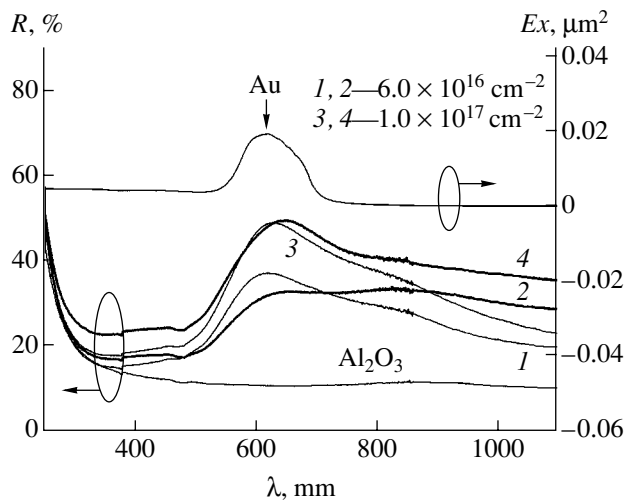
Fig. 1. Experimental optical reflection spectra of unirradiated sapphire crystals (Al_2O_3) and the samples implanted with gold to different doses (*1*, *3*) without and (*2*, *4*) with subsequent thermal annealing in air, in comparison with the model spectrum of the extinction cross section (*Ex*) calculated using Mie's theory for a single 15-nm spherical gold particle in the Al_2O_3 matrix. The numbers of curves correspond to the numbers of samples presented in the table.

redistribution of the metal phase in the volume of dielectric matrix at elevated temperatures, which probably leads to the formation of large arrays of closely spaced (and interacting with each other) metal nanoparticles or their aggregates. A similar transformation of the optical spectra was previously observed during the formation of fractal silver particles in solutions [10]. Alternatively, changes observed in the SPR spectra of metal nanoparticles can be explained by the nucleation of gold particles with isotropic shapes at elevated temperature [4].

Figure 2 shows the results of measurements of the nonlinear optical reflection in the ion-implanted composite structures. In all cases, the $R(Z)$ curves have the

Nonlinear optical characteristics of Au : Al_2O_3 composites

Sample	Irradiation dose, $\times 10^{17}$ cm^{-2}	I_0, $\times 10^9$ W/cm^2	n_2, 10^{-9} cm/W	Re$\chi^{(3)}$, 10^{-9} esu
1	0.6	2.3	−9.4	−7.8
2	0.6	2.8	−12	−10
3	1.0	2.3	−12.8	−11
4	1.0	1.8	−14.6	−12

The samples were obtained by ion implantation (1, 3) without and (2, 4) with subsequent thermal annealing; I_0 is the incident radiation intensity; n_2 is the nonlinear refractive index; Re$\chi^{(3)}$ is the real part of the third-order nonlinear susceptibility.
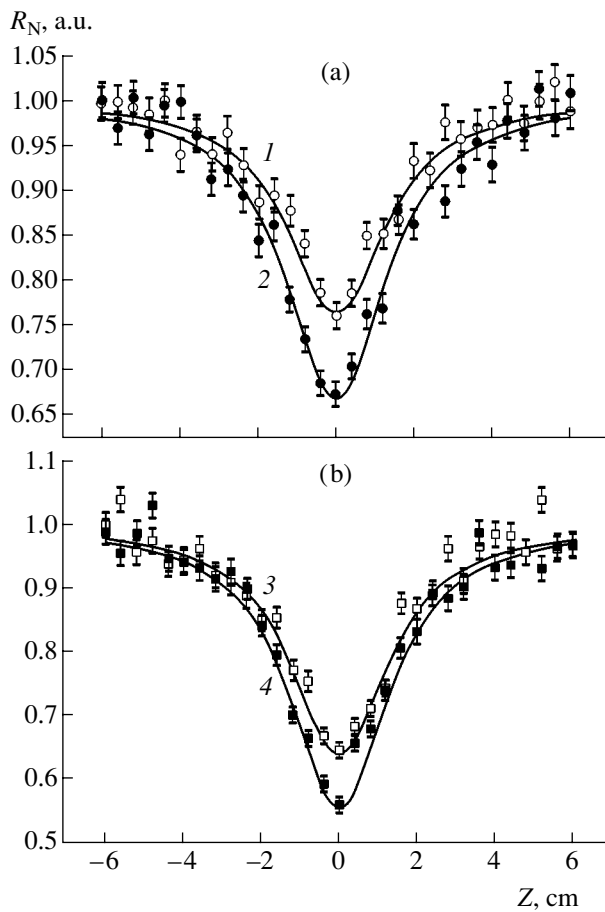
Fig. 2. Normalized reflection $R(Z)$ measured as a function of the sample position relative to the laser beam focus for Au:Al$_2$O$_3$ composites obtained by 160-keV Au$^+$ ion implantation to a dose of (a) 0.6×10^{17} and (b) 1.0×10^{17} cm^{-2} (*1, 3*) without and (*2, 4*) with postimplantation annealing for 1 h at 800°C in air. The numbers of curves correspond to the numbers of samples presented in the table (points present the experimental data, curves show the results of calculations).

inverted dome shape and are symmetric relative to the focal point ($Z = 0$) on the Z scale. As is known, this shape of the $R(Z)$ curve is characteristic of a self-action of laser radiation—in this case, nonlinear self-defocusing—with negative values of the nonlinear refractive index n_2 and of the real part of the nonlinear third-order susceptibility Re$\chi^{(3)}$. The values of n_2 and Re$\chi^{(3)}$ calculated from the experimental RZ-scan data using a method described in [1] are presented in the table.

As can be seen from data in the table, the composite materials obtained as a result of ion implantation exhibit nonlinear refraction, which is characterized by a relatively high value of Re$\chi^{(3)}$ (~10^{-8} esu) in the NIR spectral range. Since no such optical nonlinearity was observed in unirradiated Al$_2$O$_3$ even at a maximum

laser intensity, it was concluded that the nonlinear properties of the composite layers are directly related to the presence of gold particles in the sapphire matrix. Previously, the n_2 value for pure sapphire at 1064 nm was evaluated at 3×10^{-15} cm^2/W [12], which was several orders of magnitude lower than n_2 for the gold-implanted composite layers obtained in our study (see table). It should also be noted that the optical nonlinearities have been measured using laser radiation with a wavelength outside the region of SPR absorption for gold particles. Nevertheless, the observed nonlinear refraction related to the metal nanoparticles is of an electronic nature (the Curr effect), rather than being caused by the laser-induced heating of a sample (which also can, in principle, affect the refraction of the medium studied). The absence of significant laser-induced heating of the matrix is explained by ultrashort laser pulse duration and their low repetition frequency.

In conclusion, we have experimentally demonstrated that it is possible, in principle, to synthesize gold nanoparticles in a subsurface layer of Al$_2$O$_3$ by means of Au$^+$ ion implantation followed by thermal annealing. Using this method, we obtained a new composite material (Au:Al$_2$O$_2$) possessing nonlinear optical properties, featuring the phenomenon of laser self-defocusing, and characterized by a high value of Re$\chi^{(3)}$. These results are of considerable practical significance and show that there are good prospects for using Au:Al$_2$O$_3$ composites in optical switches exhibiting a change in n_2 depending on the laser radiation intensity at a short time of action (on the order of picoseconds) in the NIR spectral range, rather than only in the region of SPR of gold particles.

REFERENCES

1. U. Kreibig and M. Vollmer, *Optical Properties of Metal Clusters* (Springer-Verlag, Berlin, 1995).

2. A. L. Stepanov and D. E. Hole, Recent Res. Dev. Appl. Phys. **5**, 1 (2002).

3. R. F. Haglund, Jr., L. Yang, R. H. Magruder III, *et al.*, Nucl. Instrum. Methods Phys. Res. B **91**, 493 (1994).

4. M. Ohkubo and N. Susuki, Philos. Mag. Lett. **57**, 261 (1988).

5. C. W. White, D. K. Thomas, D. K. Hensley, *et al.*, Nanostruct. Mater. **3**, 447 (1993).

6. H. B. Liao, R. F. Xiao, J. S. Fu, *et al.*, Appl. Phys. B **65**, 673 (1997).

7. Y. Hosoya, T. Suga, T. Yanagawa, *et al.*, J. Appl. Phys. **81**, 1475 (1997).

8. A. L. Stepanov, in *Metal-Polymer Nanocomposites*, Ed. by L. Nicolais and G. Carotenuto (Wiley, Hobolen, 2004), pp. 241–263.

9. R. A. Ganeev, A. I. Ryasnyansky, A. L. Stepanov, *et al.*, Opt. Commun. (2005) (in press).

10. S. V. Karpov, A. K. Popov, and V. V. Slabko, Izv. Akad. Nauk, Ser. Fiz. **60**, 43 (1996).

11. M. Martinelli, L. Gomes, and R. J. Harowicz, Appl. Opt. **39**, 2733 (2000).

12. R. Adair, L. L. Chase, and S. A. Payne, Phys. Rev. B **39**, 3337 (1989).

Translated by P. Pozdeev

A Distributed Model of the Organization of Joule-Heating-Induced Autooscillations in a Semiconductor

A. V. Melkikh*, F. N. Rybakov, and A. A. Povzner

Ural State Technical University, Yekaterinburg, Russia
* e-mail: mav@dpt.ustu.ru
Received March 1, 2005

Abstract—A model of autooscillations caused by self-heating in a semiconductor is proposed that takes into account the spatial temperature field in a thin-film sample. Dependences of the parameters of autooscillations on the similarity numbers are determined. The obtained relations can be used for controlling autooscillations in thermoresistors. © *2005 Pleiades Publishing, Inc.*

Several models describing the instability of the current in a semiconductor caused by its self-heating have been described in the literature [1–7]. It was established that, beginning with a certain value of the bandgap width, the current–voltage (I–U) characteristics of such a semiconductor acquires an S-like shape, which can lead to the organization of autooscillations of the current and voltage. Such autooscillations of the current and voltage in semiconductors have been used in some devices based on thermoresistors (see, e.g., [8–10]). However, a theoretical analysis of autooscillations with allowance for the sample temperature dependence on the coordinates has yet to be performed.

Previously, we developed a lumped model describing current autooscillations caused by self-heating in a semiconductor, in which the temperature was assumed to be the same over the sample [11]. However, under some conditions (including certain sample dimensions and the regime of heat exchange with the environment), the temperature will be distributed over the sample volume. Such a spatial distribution may significantly change the dependence of the amplitude and period of autooscillations on the sample properties as compared to their behavior predicted by the aforementioned lumped model.

Let us consider a semiconductor sample in the form of a thin film, to which a constant bias voltage is applied. This choice of the sample shape is related to the wide use of thin films in semiconductor technology and to the fact that this geometry admits exact solution of the problem. Consideration will be restricted to the case in which the temperature depends only on the transverse coordinate, $T = T(x)$, which is justified for a sufficiently thin film, while the potential depends only on the longitudinal coordinate, $\phi = \phi(z)$.

The conductivity of the sample is assumed to obey the well-known relation for the intrinsic semiconductors [5]:

$$\sigma(T) = \sigma_\infty e^{\frac{-(E_{g0} - MT)}{2kT}}. \tag{1}$$

The temperature dependence of the thermal conductivity of a semiconductor in the general case includes the phonon, electron–hole, photon, and exciton components [13]. However, in some semiconductor materials (e.g., InSb), the electron contribution becomes significant only at temperatures on the order of 500 K or above [12, 13], the exciton and photon components are negligibly small, and the phonon component in the interval above the Debye temperature is inversely proportional to the absolute temperature [12, 13]. For such materials, the thermal conductivity variation in a quite large temperature range can be described by the relation

$$\lambda(T) = \frac{C_\lambda}{T}. \tag{2}$$

The ambient temperature will be considered fixed at a constant level ($T = T_0$). The heat flow from the sample to the environment is proportional to the temperature difference between the sample surface and the ambient medium:

$$\hat{O} = \alpha(T_s - T_0), \tag{3}$$

where T_s is the sample surface temperature and α is the heat transfer coefficient.

The system of transfer equations for the problem under consideration is as follows:

$$\mathrm{div}(\lambda\,\mathrm{grad}(T)) + \sigma\,\mathrm{grad}(\phi)^2 = 0,$$
$$\mathrm{div}(\sigma\,\mathrm{grad}(\phi)) = 0,$$

(4)

where ϕ is the potential, σ is the specific conductivity, and λ is the thermal conductivity.

Upon introducing dimensionless variables and integrating Eqs. (4), we obtain a relation between the current density and the applied voltage:

$$c_2 ju - \int_{c_1+ju}^{\overline{AEi\left(Ei\left(\frac{-1}{c_1+ju}\right)-j^2c_2\right)}} \frac{1}{p\sqrt{1+\frac{1}{j^2c_2}\left(Ei\left(\frac{-1}{p}\right)-Ei\left(\frac{-1}{c_1+ju}\right)\right)}}\,dp = 0,$$

(5)

where

$$\sigma_0 = \sigma_\infty e^{\frac{M}{2k}}, \quad T_\sigma = \frac{E_{g0}}{2k}, \quad Ei(x) = \int_{-\infty}^{x}\frac{e^x}{x}dx,$$

$$X = \frac{JU}{2LH\alpha T_\sigma}, \quad c_1 = \frac{T_0}{T_\sigma},$$

$$c_2 = h\frac{\alpha T_\sigma}{C_\lambda}, \quad Y = \frac{J^2}{8L^2 C_\lambda \sigma_0},$$

$$j = \sqrt{\frac{Y}{c_2}} = J\frac{1}{2L\sqrt{2\sigma_0 h\alpha T_\sigma}},$$

$$u = X\sqrt{\frac{c_2}{Y}} = U\frac{1}{H}\sqrt{\frac{2\sigma_0 h}{\alpha T_\sigma}}.$$

The results of the numerical integration of Eq. (5) show that the *I*–*U* curve may have a region of negative differential resistance. As is known, the presence of such a feature may lead to the organization of autooscillations [6].

Using thermoresistors as autooscillators, it is possible to obtain ultralow-frequency autooscillations that can be used in various applications (e.g., for ambient temperature monitoring). The operation of such an oscillator is described by the following set of equations (in dimensionless variables):

$$\frac{d}{ds}p = \frac{u^2}{2c_3}\exp\left(\frac{-1}{p}\right) + \frac{d}{dr}\left(\frac{1}{p}\frac{d}{dr}p\right)\frac{1}{c_2 c_3},$$

$$\frac{d}{ds}u = 2j_0 - u\int_0^1 \exp\left(\frac{-1}{p}\right)dr,$$

(6)

$$\left(\frac{d}{dr}p\right)_{r=1} = -c_2 p_{r=1}(p_{r=1}-c_1), \quad \left(\frac{d}{dr}p\right)_{r=0} = 0,$$

where $c_3 = 2c\rho L\sigma_0 h^2/\alpha CH$ is a dimensionless constant quantity dependent on the heat capacity, electric capacitance, and geometry of the sample. Physically, this constant characterizes the ratio of the characteristic time of heat exchange and the capacitive time.

By numerically solving system (6), we determine the relations between the parameters of autooscillations and the properties of the semiconductor and the ambient medium. In particular, an increase in the c_2 value (which is proportional to the Nusselt number) leads to a significant difference between the lumped and distributed models (Fig. 1). This implies that the parameters of autooscillations in a system characterized by a large c_2 (i.e., by good heat exchange with the environment or by large film thickness) cannot be determined within the framework of a lumped model, and a more precise distributed model must be used. As can be seen from Fig. 2, the period of autooscillations increases with c_3.

Thus, by changing the conditions of heat exchange, the sample geometry, and/or the bandgap width, it is possible to optimize the operation of an autooscillator based on a thermoresistor, so as to obtain the required period and amplitude of autooscillations. In particular, the period of autooscillations can be increased by
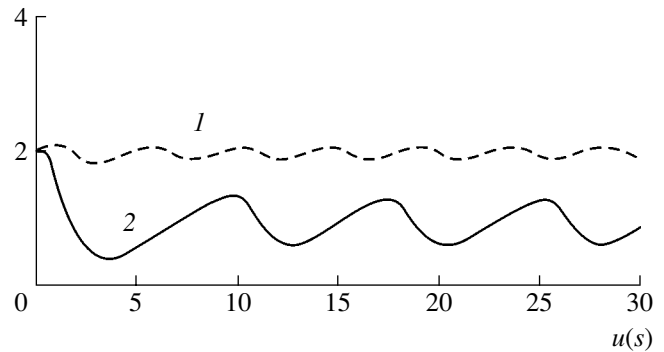
Fig. 1. Time variation of the voltage in a thermoresistor circuit with the parameters $c_1 = 0.24$, $c_2 = 10$, $c_3 = 0.1$, $j_0 = 0.1$, $u_0 = 2$, and $p_0 = c_1$, as described using (*1*) lumped and (*2*) distributed models.
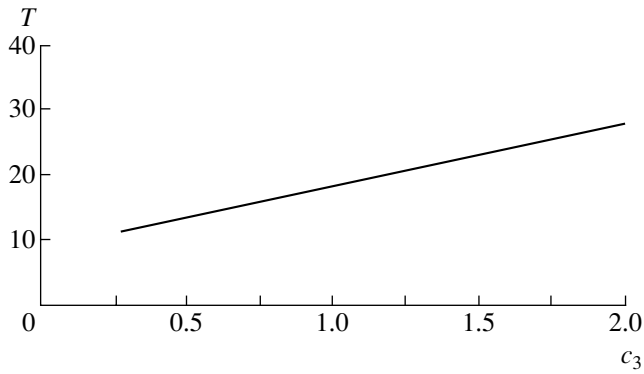
Fig. 2. Plot of the period of autooscillations (approximated as $T = 8 + 13c_3$) versus dimensionless parameter c_3 for a thermoresistor circuit with the parameters $c_1 = 0.24$, $c_2 = 10$, $j_0 = 0.1$, $u_0 = 0$, and $p_0 = c_1$.

decreasing the heat transfer to the ambient medium or by increasing the semiconductor dimensions.

REFERENCES

1. M. P. Shaw and N. Yildirim, Adv. Electron. Electron. Phys. **60**, 307 (1982).

2. L. Altchen and N. Klein, IEEE Trans. Electron Devices **20**, 801 (1973).

3. A. Alekseev, S. Bose, P. Rodin, and E. Scholl, Phys. Rev. E **57**, 2640 (1998).

4. P. Rodin, Phys. Rev. B **69**, 045307 (2004).

5. P. Yu and M. Cardona, *Fundamentals of Semiconductors: Physics and Materials Properties*, 3rd ed. (Springer-Verlag, Berlin, 2001).

6. E. Schöll, *Nonequilibrium Phase Transitions in Semiconductors: Self-Organization Induced by Generation and Recombination Processes* (Springer-Verlag, Berlin, 1987).

7. A. F. Volkov and Sh. M. Kogan, Usp. Fiz. Nauk **96**, 633 (1968) [Sov. Phys. Usp. **11**, 881 (1968)].

8. E. D. Macklen, *Thermistors* (Electrochem. Publ., Ayr, 1979; Radio i Svyaz', Moscow, 1983).

9. I. T. Sheftel', *Thermistors. Electrical Conduction of 3d Oxides: Parameters, Characteristics, and Applications* (Nauka, Moscow, 1973) [in Russian].

10. A. I. Krivonosov, *Semiconductor Temperature Sensors* (Énergiya, Moscow, 1974) [in Russian].

11. A. V. Melkikh and A. A. Povzner, Pis'ma Zh. Tekh. Fiz. **29** (6), 14 (2003) [Tech. Phys. Lett. **29**, 224 (2003)]

12. B. M. Mogilevskiǐ and A. F. Chudnovskiǐ, *Thermal Conduction in Semiconductors* (Nauka, Moscow, 1972) [in Russian].

13. K. Seeger, *Semiconductor Physics* (Springer-Verlag, Berlin, 1974).

Translated by P. Pozdeev

A Diplexer Based on an Open Resonator
with Corrugated Mirrors

**Yu. I. Koshurinov[a], V. G. Pavel'ev[a], M. I. Petelin[a],
I. V. Turchin[a],*, and D. Yu. Shchegol'kov[b]**

[a] *Institute of Applied Physics, Russian Academy of Sciences, Nizhni Novgorod, Russia*
[b] *Nizhni Novgorod State University, Nizhni Novgorod, Russia*
** e-mail: ilya@ufp.appl.sci-nnov.ru*
Received March 1, 2005

Abstract—A diplexer with a resonance frequency of 34 GHz has been created based on a four-mirror ring resonator with two corrugated mirrors. When the incident wave frequency varies by more than 20 MHz, the output wave beam is completely switched from one direction to another. A diplexer of this type can be used for discrete frequency scanning of high-power wave beams in systems for the suppression of the hydrodynamic instabilities of plasma in magnetic traps. Such diplexers can also be combined so as to form a multiplexer, which can be used in long-range multichannel communication and radar systems with synthesized frequency bands. © *2005 Pleiades Publishing, Inc.*

Multiplexers are devices used for adding and subtracting signals with different frequencies, which have various configurations depending on the particular application [1–6]. In particular, a high frequency selectivity is achieved with the aid of resonance multiplexers [1, 4–6]. In the millimeter wavelength range, it is expedient to use resonance multiplexers of the quasi-optical type [4–6].

This Letter presents the results of an experimental study of a diplexer in the form of the symmetric four-mirror ring resonator that is schematically depicted in Fig. 1. The resonator contains two corrugated mirrors *1* and *3*, in which the corrugation period and orientation are selected so as to ensure that, upon the scattering of a plane input wave incident onto the corrugated mirror *1*, only the (–1)-order diffraction beam will exist in addition to the mirror-reflected beam (nonresonant output wave) far from this mirror. The (–1)-order beam passes out of the plane containing the incident and mirror-reflected beams and is directed toward focusing mirror *2*. On the whole, the ring resonator has a symmetric design such as depicted in Fig. 1.
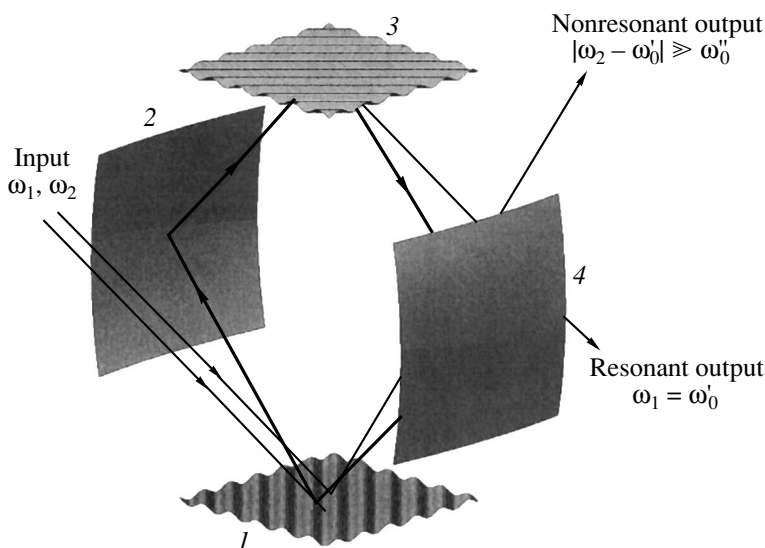
Fig. 1. Schematic diagram of the symmetric four-mirror resonator with two corrugated mirrors in the regime of separation of two signals with different frequencies (see the text for explanations).
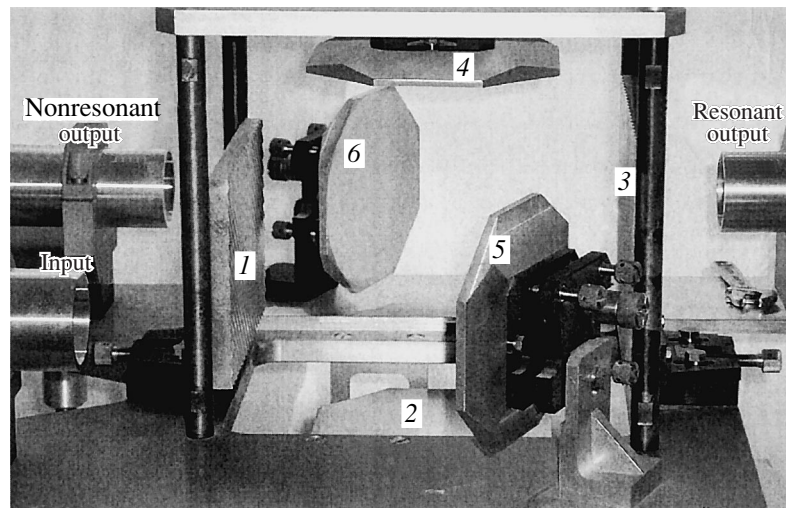
Fig. 2. Experimental setup for measurement of the diplexer transmission coefficient (see the text for explanations).

The corrugation height is selected based on the following considerations. On the one hand, it must be small so as to ensure that the intensity of the (–1)-order diffraction beam will be much lower than that of the mirror-reflected beam and that the resonance curves of high-Q modes will not overlap. On the other hand, the corrugation height must be large enough to ensure that the working radiation mode quality factor Q_{rad} (determined by the scattering of the circulating wave flux from corrugated mirrors) will be significantly lower than the values of Q_{ohm} and Q_{diff} determined by the ohmic losses and by the wave flux diffusion out of the mirrors, respectively. These competing conditions can be combined and formulated as

$$\omega L/c \ll Q_{rad} \ll Q_{ohm}, Q_{diff}, \tag{1}$$

where L is the beam circulation length inside the resonator.

Conditions (1) imply that the resonator is overloaded by coupling to the external waveguides. Since this coupling is symmetric (owing to the identical characteristics of the input and output corrugated mirrors), the resonator is fully transparent at the intrinsic resonance frequency ω_0': all the power of the radiation reflected from corrugated mirror *3* is extracted in the resonant output direction (Fig. 1). Should the incident wave frequency fall outside the working band $|\omega - \omega_0'| \gg \omega_0'' = \omega_0'/2Q_{rad}$, the field in the resonator will not be excited and the incident wave will be mirror-reflected in the nonresonant output direction.

For an arbitrary frequency in the vicinity of the intrinsic resonance, the frequency dependence of the coefficients of wave transmission (T) to the resonant output and its reflection (R) toward the nonresonant output is described by the universal functions [7]

$$R(\omega) = \frac{\omega - \omega_0'}{\omega - \omega_0' - i\omega_0''},$$
$$T(\omega) = \frac{-i\omega_0''}{\omega - \omega_0' - i\omega_0''}. \tag{2}$$

Below, we present the results of experiments with a diplexer prototype in which the input and output beams formed an angle of 45° with the plane of wave circulation in the resonator (Fig. 2). Flat gratings (corrugated mirrors) *1* and *3* had a sine-shaped corrugation, with the grooves oriented at an angle of 45° relative to the same plane. The wave field was E-polarized relative to the direction of corrugation grooves. The wave scattering was calculated using the method of integral equation [8]. The focusing mirrors *2* and *4* (Fig. 2) represented the segments of elliptic paraboloids with the parameters ensuring the circulation of a Gaussian beam whose size in the circulation plane was half of that in the perpendicular direction. This circumstance allowed us to use axisymmetric Gaussian beams at the resonator input and output. The table presents a set of the resonator parameters calculated using a method analogous to that described in [9].

A system of radiation feed in the diplexer comprised a junction from a rectangular H_{10}-waveguide to a round H_{11}-waveguide, a profiled horn converting the H_{11} wave into a linearly polarized Gaussian beam [10], and a mirror *5* (Fig. 2) focusing the beam on grating *1*. The output radiation was extracted from the diplexer using two systems analogous to the radiation feed-in system (Fig. 2).

The system used for the measurement of power reflection and transmission coefficients of the diplexer comprised a microwave generator based on the Gunn

P/P_0
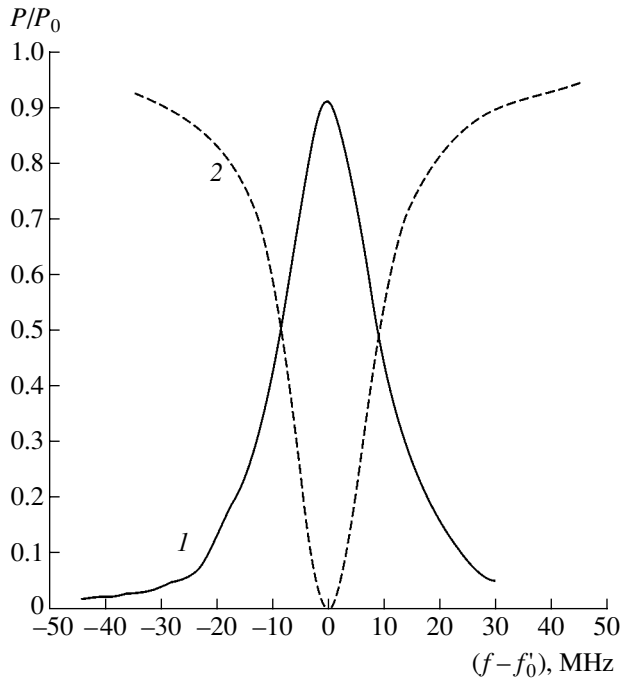
Fig. 3. The experimentally measured coefficients of (*1*) power transmission via the resonant channel and (*2*) power reflection to the nonresonant channel as functions of the frequency for a diplexer based on the resonator scheme depicted in Fig. 1.

diode with a capacity-tuned oscillator circuit (varicap), a ramp generator controlling the radiation source frequency, a high-precision waveguide attenuator, a diplexer, two microwave detectors, and a two-channel oscillograph. The signal frequency was modulated at a rate of 29 MHz/μs by variable control voltage on the microwave oscillator.

Parameters of an open resonator with corrugated mirror

Frequency, Hz	34.27
Transverse size of focusing mirrors, mm	184×223
Curvature radius of focusing mirrors, mm	1018×6003
Lateral size of corrugated mirrors, mm	156×221
Corrugation period, mm	8.75
Corrugation height, mm	0.76
Distance between centers of neighboring mirrors in resonator, mm	202
Coefficient of beam power coupling to (–1)-order reflection maximum in corrugated mirrors, %	13
Radiation quality factor Q_{rad}	2000
Resonator quality factor $(1/Q_{ohm} + 1/Q_{diff})^{-1}$ determined by ohmic losses and wave flux diffusion out of mirrors	50000

The experimental results are presented in Fig. 3, which shows plots of the output power measured in both output channels (normalized to the input signal power) as functions of the frequency. The line full width at half height is 18 MHz, which corresponds to the theoretically calculated value. The diplexer input signal power was determined taking into account that 87% of the incident radiation power in the resonator with absorber was transmitted to the nonresonant output, while about 13% is dissipated in the absorber.

Conclusions. The proposed resonance mirror diplexer can be used for discrete frequency scanning of high-power wave beams in the vicinity of a carrier frequency in the 140–170 GHz range used in the systems for the suppression of the hydrodynamic instabilities of plasma in magnetic traps [11, 12].

Diplexers of this type can also be combined so as to form a multiplexer [6], which can be used in long-range multichannel communication and radar systems with synthesized frequency bands [5, 13]. However, both amplitude and phase characteristics are important in the case of multiplexers for such applications. The phase properties of such devices will be studied separately.

REFERENCES

1. G. Matthaei, L. Young, and E. M. T. Jones, *Microwave Filters, Impedance-Matching Networks, and Coupling Structures* (McGraw-Hill, New York, 1964).
2. A. A. Kirilenko, S. L. Senkevich, V. I. Tkachenko, and B. G. Tysik, Élektron. Tekh., Ser. Élektron. SVCh, No. 6, 3 (1991).
3. P. S. Henry and J. T. Ruscio, IEEE Trans. Microwave Theory Tech. **26**, 428 (1978).
4. M. H. Chen, IEEE Trans. Microwave Theory Tech. **28**, 363 (1980).
5. M. I. Petelin, G. Garyotakis, A. A. Tolkachev, *et al.*, AIP Conf. Proc. **474**, 304 (1999).
6. I. V. Turchin, Radiotekh. Élektron. (Moscow) **48**, 684 (2003).
7. M. I. Petelin and I. V. Turchin, Radiotekh. Élektron. (Moscow) **46**, 1445 (2001).
8. G. G. Denisov and S. V. Kuzikov, Int. J. Infrared Millim. Waves **18**, 733 (1997).
9. M. I. Petelin and Yu. Yu. Danilov, Int. J. Infrared Millim. Waves **20**, 2023 (1999).
10. V. G. Pavelev, S. E. Tsimring, and V. E. Zapevalov, Int. J. Electron. **63**, 379 (1987).
11. H. Zohm, G. Gantenbein, G. Giruzzi, *et al.*, Nucl. Fusion **39**, 577 (1999).
12. G. Gantenbein, H. Zohm, G. Giruzzi, *et al.*, Phys. Rev. Lett. **85**, 1242 (2000).
13. G. Caryotakis, G. Scheitrum, M. Petelin, *et al.*, in *Proceedings of NATO Advance Research Workshop on Quasi-Optical Control of Intense Microwave Transmission, Nizhni Novgorod, 2005* (Kluwer Academic, New York) (in press).

Translated by P. Pozdeev

Influence of the State of Interfaces on the Character of Local Displacements in Fault-Block and Interfacial Media

S. G. Psakhie, V. V. Ruzhich, E. V. Shilko, V. L. Popov, A. V. Dimaki,
S. V. Astafurov*, and V. V. Lopatin

Institute of Strength Physics and Materials Science, Siberian Division, Russian Academy of Sciences,
Tomsk, 634055 Russia
Institute of the Earth's Crust, Siberian Division, Russian Academy of Sciences, Irkutsk, 664033 Russia
Berlin Technical University, Berlin, Germany
Research Institute of High-Voltage Equipment, Tomsk Polytechnical University, Tomsk, 634034 Russia
* e-mail: asta@usgroups.com
Received March 23, 2005

Abstract—We have studied the possibility of producing a directed action upon the process of local stress relaxation in interfacial media occurring in a complex stressed state by changing the state of boundaries between structural elements. The experiments were performed on the ice sheet of Lake Baikal, which represents a hierarchically organized fault-block structure and belongs to the class of interfacial media. It is shown that, by changing the state of boundaries between structural elements, it is possible to influence the regime of deformation of the interfacial medium as a whole. The general features of the observed effect are confirmed within the framework of a theoretical model. © 2005 Pleiades Publishing, Inc.

In recent years, increasing attention has been devoted to the class of so-called interfacial materials, which includes the media whose mechanical response is determined to a considerable degree by the process of strain localization at the boundaries (interfaces) between structural elements [1]. The most important example is offered by nanostructural materials, in which the extremely small grain size limits to a significant extent the traditional dislocation mechanisms of deformation [2]. The most important role is played by processes at the grain boundaries, which provide deformation on a higher (mesostructural) level by means of relative displacements of the structural elements (blocks) [3].

The class of interfacial materials also contains the so-called fault-block media, including, in particular, natural systems such as the Earth's crust. A characteristic feature of the Earth's crust is a multilevel, hierarchically organized block structure [4], which accounts for the relatively high deformability of this complex system. In accordance with the concepts of the physical mesomechanics, the release of elastic energy accumulated in a medium is related primarily to the process of strain localization in the zones of the so-called active boundaries of contacting blocks, which are determined by the stressed state of a given fault-block medium and by its structural features [5]. It should be noted that the regime of energy dissipation in such systems bears a spatially correlated character.

The character of relative motions of the structural elements in fault-block media is determined to a con-siderable degree by the state (i.e., by a set of mechanical characteristics) of the active interfacial zones. Therefore, we can expect that the mechanism of local stress relaxation in such media can be controlled by means of changing the state of the active boundaries (interfacial zones) between blocks. In the case of natural interfacial media, the state of the active fault-block interfaces can be changed, for example, by flooding these zones. This possibility has been demonstrated by the results of model and large-scale natural experiments [6, 7]. Additional indirect evidence is provided by the correlation between the seismic activity and the groundwater level in the course of groundwater recharge in the preexisting fault zones [8, 9].

It should be noted that the experimental investigation of real geological media encounters considerable difficulties related to the large spatial scale of these objects (in particular, the characteristic fault length varies from tens to thousands of kilometers) and the long characteristic times of geological processes (reliable data on the fault response to the action of external factors can only be obtained after many-year observations).

In this study, the possibility of directed action upon the regime of stress relaxation in interfacial media via modification of the state of active interfaces was studied in experiments on the fault-block system of the ice sheet of Lake Baikal.

The choice of an ice sheet as the object for investigation of the laws of behavior of a fault-block medium is justified by the close similarity of the rheological

behavior of this object to the behavior of typical fault-block media and by a number of other advantages. These include the possibility of choosing a desired characteristic block size within rather wide limits (from several meters to kilometers), the relatively short characteristic times of manifestation of the deformation and fracture processes (typically not exceeding several days), and the possibility of acting upon the ice sheet fragments throughout their thickness.

Figure 1 shows one of the active interfaces in the ice field of Lake Baikal, on which the experiments were carried out. The interfaces in ice bodies are called cracks. The total length of the crack presented in Fig. 1 is close to several kilometers. This interface was selected for investigation, in particular, because it represented an active crack by which the main shear displacements in the ice fault-block medium took place. The magnitude of this shear (~0.1 m) could be evaluated by determining the relative displacements of the ends of relatively old broken cracks, which are also well distinguished in Fig. 1. One of the signs of activity for the cracks in ice is the level of water. In the given crack, the water level occurred at a depth below 0.1 m from the surface, which indicated that the crack was rather active and, hence, convenient for experimental investigation. For comparison, it may be noted that the ice thickness in the adjacent blocks was 0.75–0.78 m.

The state of the crack was modified by drilling a series of through holes in the ice, which had a diameter of 25 mm and were spaced at 0.1–0.12 m. The holes were made over a rather extended part of the crack length, typically in excess of 100 m. This resulted in an elevation of the water level, that is, in artificial flooding of the fault-block system.

Figure 2 shows the results of monitoring of the relative displacements of the crack edges over a time period within 30–90 min after the onset of flooding (15:25). It is seen that, beginning with 16:10 (i.e., approximately 45 min after the onset of flooding), the normal displacements (Fig. 2a) exhibit a certain tendency to grow. The main growth stage begins approximately at 16:21 (about one hour after the onset of flooding). The total magnitude of irreversible normal displacements of the crack edges amounted to ~50 μm for half an hour.

The shear displacements (Fig. 2b) are also activated beginning with 16:10, but the initial stage reveals only a short-term (~3 min) outburst of reversible alternating-sign displacements with the maximum amplitude being several times greater than the background oscillation level. Subsequent monitoring of the crack edge displacements showed that modification of the state of the block interface led to a change in the character of elastic energy dissipation in the medium. This was manifested, in particular, by a jumplike shift of the crack edge (Fig. 2b). This displacement occurred within less than 1.5 min (between 16:37:25 and 16:38:40), after which the shear displacements were practically stabilized. As can be seen from Fig. 2b, the irreversible jum-
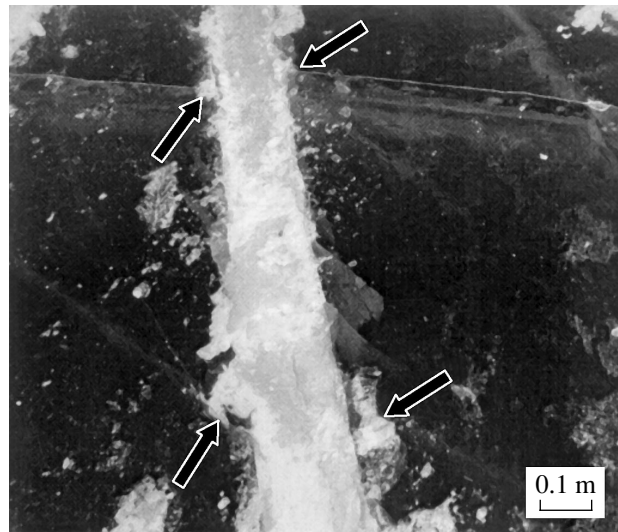

Fig. 1. A photograph showing the active interfaces of blocks in the ice field of Lake Baikal. Arrows indicate the ends of relatively old cracks broken by shear displacements.
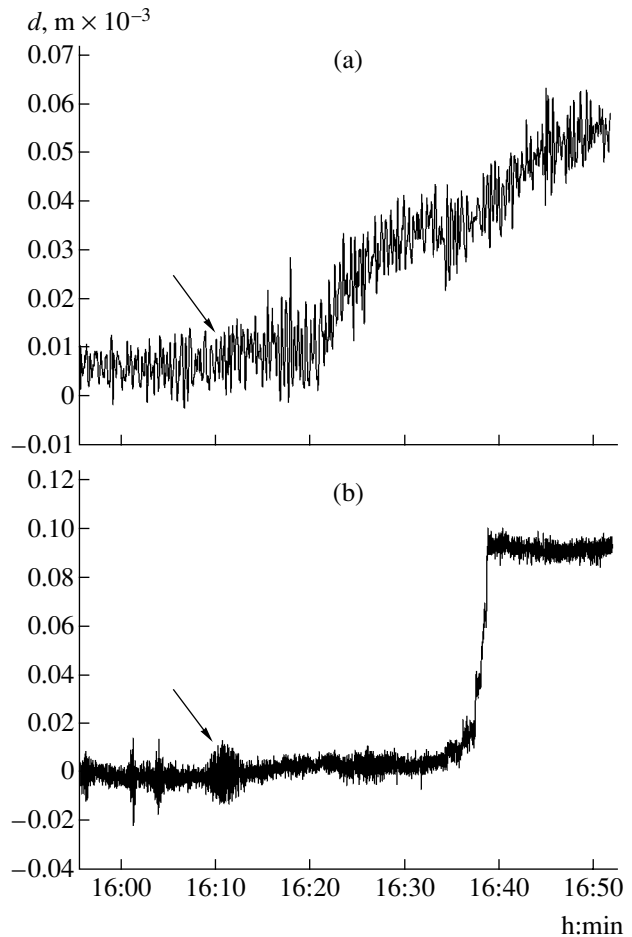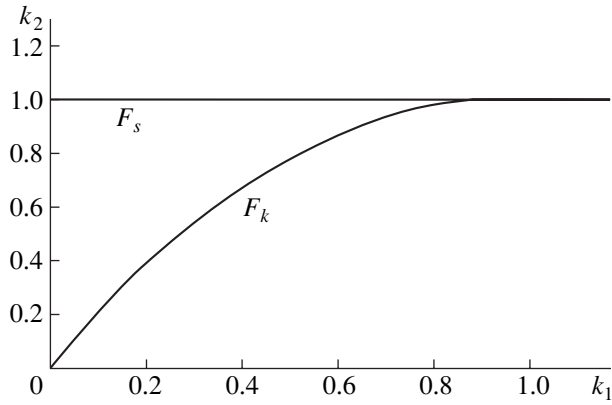

Fig. 2. Time series of the relative (a) normal and (b) shear displacements of the ice crack edges observed over a time period within 30–90 min after the onset of artificial flooding. Arrows indicate the onset of activation of the displacements.

Fig. 3. A phase diagram of the generalized one-dimensional Tomlinson model plotted on the plane of parameters (k_1, k_2).

plike displacement exceeded 90 μm within less than 5 min, which corresponded to the typical natural daily shear displacement in such cracks.

The results obtained in this study reveal certain laws in the behavior of fault-block medium fragments. Considering the interface between blocks as a trivial tribological contact, we can analyze the behavior of this model system in terms of the generalized Tomlinson model [10]. This model considers the one-dimensional motion of a body with mass m under the action of force F in the field of a periodic potential drag force with amplitude N and period a. The corresponding equation of motion can be written as

$$m\ddot{x} = F - \eta\dot{x} - N\sin(2\pi x/a), \qquad (1)$$

where η is the viscosity, x is the coordinate, $\dot{x} = dx/dt$, $\ddot{x} = d^2x/dt^2$, and t is the current time. Passing to the reduced variables $\tilde{x} = 2\pi x/a$ and $\tilde{t} = t\sqrt{2\pi N/ma}$, we can rewrite Eq. (1) as

$$\tilde{x}'' + k_1\tilde{x}' + \sin(\tilde{x}) = k_2, \qquad (2)$$

where $\tilde{x}' = d\tilde{x}/d\tilde{t}$, $\tilde{x}'' = d\tilde{x}^2/d\tilde{t}^2$, $k_1 = \eta/\sqrt{2\pi Nm/a}$, and $k_2 = F/N$.

As can be seen, Eq. (2) contains only two parameters (coefficients k_1 and k_2). Figure 3 shows a phase diagram of this model plotted on the plane of parameters (k_1, k_2), where the $F_s(k_2 = F/N = 1)$ horizontal line corresponds to the static friction force and the F_k curve shows the kinetic friction force (which is the minimum force necessary to maintain the motion). The region $k_1 < 1$ corresponds to motion in the stick-slip regime, with the jump amplitude decreasing with a growth in k_1. In the region of $k_1 \geq 1$, the body moves at a constant velocity.

In application to the problem of activating the displacements of interfaces in a fault-block medium, the situation in Fig. 3 can be interpreted as follows. The motion, once initiated, continues until the drag would exceed the acting internal stresses. Then, if the internal stresses again exceed the current level of the static friction force, the motion can be repeatedly initiated. The k_1 value increases with decreasing amplitude N of the drag force or with increasing viscosity η of the medium (i.e., when the state of the interface exhibits a change). Therefore, under otherwise equal conditions, the motion is more frequently initiated in a system with greater k_1, but proceeds with smaller amplitude. In the integral expression, this leads to an increase in the average velocity of the relative displacement of blocks. Apparently, in the case of a crack in the ice field, an increase in k_1 can be achieved at the expense of flooding.

To summarize, investigation into the behavior of block interfaces in an ice sheet demonstrated that, by changing the state of the active interfacial zone between structural elements of a fault-block (interfacial) medium occurring in a complex stressed state, it is possible to initiate or accelerate the relative displacements of blocks in the direction determined by the local stress field. This possibility can be considered as an effective means of providing relaxation of the excess local stresses in fault-block media of various natures. The obtained results and their analysis within the framework of the Tomlinson model provide a new approach to the explanation of results presented in [6–9].

REFERENCES

1. S. G. Psakhie, E. V. Shil'ko, and S. V. Astafurov, Pis'ma Zh. Tekh. Fiz. **30** (6), 45 (2004) [Tech. Phys. Lett. **30**, 237 (2004)].

2. A. I. Gusev and A. A. Rempel, *Nanocrystalline Materials* (Fizmatlit, Moscow, 2004; Cambridge Int. Sci. Publ., 2004).

3. Yu. R. Kolobov, R. Z. Valiev, G. P. Grabovetskaya, A. P. Zhilyaev, E. F. Dudarev, K. V. Ivanov, M. B. Ivanov, O. A. Kashin, and E. V. Naĭdenkin, *Grain-Boundary Diffusion and Properties of Nanostructural Materials* (Nauka, Novosibirsk, 2001) [in Russian].

4. M. A. Sadovskiĭ, L. G. Bolkhovitinov, and V. F. Pisarenko, *Deformation of Geophysical Media and Seismic Process* (Nauka, Moscow, 1987) [in Russian].

5. G. G. Kocharyan and A. A. Spivak, *Dynamics of Block Massif Deformation* (IKTs "Akademkniga," Moscow, 2003) [in Russian].

6. V. V. Ruzhich, S. G. Psakhie, S. A. Bornyakov, *et al.*, Fiz. Mezomekh. **6**, 41 (2003).

7. S. G. Psakhie, V. V. Ruzhich, E. V. Shil'ko, *et al.*, Fiz. Mezomekh. **7**, 23 (2004).

8. J. K. Costain, G. A. Bollinger, and J. A. Speer, Geology **15**, 618 (1987).

9. M. O. Saar and M. Manga, Earth Planet. Sci. Lett. **214**, 605 (2003).

10. G. A. Tomlinson, Philos. Mag. **7**, 905 (1929).

Translated by P. Pozdeev

Self-Organization
of Three-Dimensional Lead Telluride Nanoislands
under Conditions Close to Thermodynamic Equilibrium

V. N. Vodop'yanov*, A. P. Bakhtinov, E. I. Slyn'ko, G. V. Lashkarev**,
V. M. Radchenko, P. M. Lytvyn, and O. S. Lytvyn***

*Frantsevich Institute for Problems of Materials Science (Chernivtsy Department), National Academy of Sciences of Ukraine,
Chernivtsy, Ukraine*
Frantsevich Institute for Problems of Materials Science, National Academy of Sciences of Ukraine, Kiev, Ukraine
Lashkarev Institute of Semiconductor Physics, National Academy of Sciences of Ukraine, Kiev, Ukraine
*e-mail: * chimsp@unicom.cv.ua; ** georgl@imsp.kiev.ua; *** olytvyn@isp.kiev.ua*
Received April 14, 2005

Abstract—Three-dimensional lead telluride (PbTe) nanoislands were grown on (111)BaF$_2$ substrates by hot-wall epitaxy (HWE) from vapor phase under conditions close to thermodynamic equilibrium and their surface morphology was studied by atomic force microscopy in various growth stages, including the initial stage of nucleation and the subsequent evolution of the size and shape of nanoislands. The distributions of island dimensions in the samples grown under various thermodynamic conditions were statistically analyzed. It is shown that the proposed HWE method ensures the formation of dense (~8×10^{10} cm^{-2}) self-organized arrays of PbTe quantum dots with parameters comparable with those of the quantum dots of the same material grown by molecular beam epitaxy according to the Volmer–Weber mechanism. © *2005 Pleiades Publishing, Inc.*

The self-organization of quantum dots (QDs) of A^{IV}B^{VI} semiconductors has been extensively studied, which is related to the prospects for obtaining lasers operating in the middle IR spectral range [1]. The formation of three-dimensional (3D) nanoislands of such semiconductors was studied using molecular beam epitaxy (MBE) under conditions corresponding to epitaxial growth according to the Stranski–Krastanow (S–K) [2, 3] and Volmer–Weber (V–W) [4] mechanisms. As is known, the QD size distribution depends both on the nucleation conditions and on the subsequent growth dynamics [3]. These processes also determine the properties of a buffer lead telluride (PbTe) layer (called the "virtual substrate" [5] or "quasi-substrate" [3]) used for obtaining lead telluride QDs [2, 3] as well as the dispersion of these QDs grown on (111)-oriented single crystal barium fluoride (BaF$_2$) substrates [4].

The role of thermodynamic and kinetic factors in the nucleation and growth of PbTe nanoislands according to the V–W mechanism remains insufficiently studied. It was of interest to obtain such QDs by means of hot-wall epitaxy (HWE) from the vapor phase—a method used for the growth of A^{IV}B^{VI} epilayers [6] and related superlattices [7]. Using the HWE process, it is possible to grow the epilayers under conditions close to thermodynamic equilibrium, with a small supersaturation of the vapor phase, and to provide for independent monitoring of the growth temperature and the vapor supersaturation in the zone of condensation. This method for

the growth of QDs of A^{IV}B^{VI} was recently suggested in [8].

This Letter presents the results of an analysis of the growth process and the surface morphology characteristics of PbTe nanoisland arrays grown by HWE under various thermodynamic conditions on (111)-cleaved BaF$_2$ substrates. The surface morphology of PbTe nanoislands was studied by atomic force microscopy (AFM). The measurements were performed on a Nanoscope IIIa Dimension 3000SPM instrument (Digital Instruments) in the tapping mode. The probe tip radius did not exceed 10 nm. The sample morphology was studied in air (*ex situ*) after HWE deposition of PbTe nanoislands.

PbTe nanoislands were grown at a residual pressure of ~1.3×10^{-5} Pa using a modified HWE method with the aid of a special device [6] mounted in a cooled vacuum chamber. The (111)BaF$_2$ substrates had a block structure with a block size of ~1–5 mm. The AFM measurements were performed in the regions situated inside the blocks and characterized by a dislocation density from 2×10^4 to 10^5 cm^{-2}. The HWE growth was carried out at various substrate temperatures within $T_s = 573$–673 K. In contrast to the conditions used in [6, 9], where scanning and transmission electron microscopy methods were used to study the nucleation of PbTe epilayers on BaF$_2$ at evaporator temperatures within $T_{ev} = 800$–830 K, we used a lower source temperature:

$T_{ev} = 673$ K. According to [10], a decrease in the evaporator temperature from 773 to 673 K leads to a decrease in the saturated PbTe vapor pressure from $P_{PbTe} \sim 6.5 \times 10^{-2}$ Pa to 4.6×10^{-5} Pa.

The quartz reactor used for the HWE growth can be considered as a short tube with $L/d < 30$, where L and d are the reactor length and diameter, respectively. For this reactor geometry and the values of saturated vapor pressure $P_{PbTe} \sim 4.6 \times 10^{-5}$ Pa and the two-component vapor viscosity $\mu \sim 5 \times 10^{-5}$ Pa s [10], the Knudsen number is $N_K \gg 1$. On this level of PbTe evaporation, the reactor features a molecular regime of vapor flow in the hot-wall reactor and provides for a growth rate of $v \sim 0.01$–0.1 ML/s (ML = monolayer ~ 3.73 Å for PbTe). These values are comparable with the deposition rates used in MBE ($v \sim 0.05$–0.15 ML/s [2, 3, 4]). The source of vapor was a preliminarily synthesized stoichiometric PbTe, which provided a minimum total pressure of the vapors of components at a selected sublimation temperature; under such conditions, PbTe exhibits congruent evaporation [10]. In selecting T_s, we took into account that tellurium exhibits re-evaporation from the substrate temperature at temperatures above 673 K [4, 7].

It should be noted that we will not consider processes involving nanoisland nucleation on surface defects such as cleavage steps, small-angle boundaries, and traces of (100) dislocation glide planes.

The results of AFM investigations showed that, under the conditions of thermodynamic equilibrium, the HWE growth (as well as MBE [4, 5]) of PbTe proceeds according to the V–W mechanism. Direct nucleation of 3D nanoislands of PbTe on the (111)BaF$_2$ surface (in the absence of a 2D wetting layer [2, 3]) under conditions of a ~4% lattice mismatch and partial wetting is explained by the fact that the specific free surface energy of the (111) substrate for PbTe is greater than that for BaF$_2$ [5, 6]. This condition holds, provided that substrate wetting is not significantly modified by atoms of the residual atmosphere present in the chamber and striking the substrate. We observed 3D growth at a coverage of $d < 1$ ML, whereas a spontaneous formation of 3D islands of A^{IV}B^{VI} according to the S–K mechanism usually takes place at a wetting layer thickness of $d > 1.5$ ML [2, 3]. The surface density of PbTe nanoislands obtained at $T_s = 608$ K and a wall temperature $T_w = 763$ K increases with the amount of deposited material: from ~2.2×10^{10} cm^{-2} at $d = 0.8$ ML to 4×10^{10} cm^{-2} at $d = 2.7$ ML. New 3D nuclei were continuously formed during the growth of existing islands over a time period of 3 min. During this time, the aspect ratio r of the nanoislands, which is defined as the ratio of the vertical (h) to the lateral (l) size, increases from $r \sim 0.07$ at $d = 0.8$ ML to $r \sim 0.19$ at $d = 2.7$ ML. Such a change in the equilibrium shape of PbTe quantum dots was also observed in [4], where it was explained by the fact that
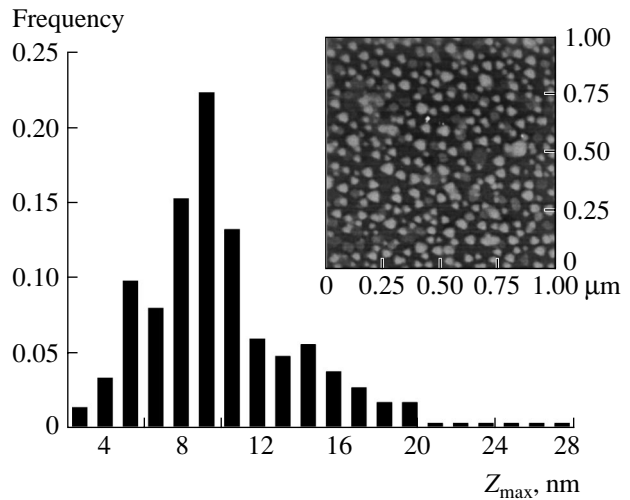

Fig. 1. A histogram of the distribution of PbTe nanoislands with respect to height obtained after deposition of 4 ML of PbTe onto (111)BaF$_2$ surface. The data were obtained by statistical processing of an AFM image presented in the inset (top view; 1×1 μm area). Deposition regime: $T_{ev} = 673$ K; $T_s = 623$ K; $T_w = 763$ K.

the strain energy accumulated in coherently grown 3D islands counteracts the substrate wetting [11].

In the absence of defects (which could act as the nucleation centers [3]) on the BaF$_2$(111) surface, the formation of 3D nuclei is a random process involving the activation barrier for nucleation. The values of the stable critical nucleus size and the activation barrier height depend on the degree of supersaturation [11]. At a low supersaturation ($T_s = 623$ K, $T_w = 718$ K), the number of critical nuclei is small (below 10^{10} cm^{-2}) and they are characterized by a large spread in both height ($h = 6$–10 nm) and aspect ratio ($r = 0.06$–0.15) [8]. An increase in the wall temperature from ~718 to 763 K leads to a growth in the molecular flow of PbTe and in the vapor phase supersaturation in the zone of condensation. The activation barrier for nucleation decreases [11] and the surface density of nanoislands increases to ~2.9×10^{10} cm^{-2} (Fig. 1). As can be seen from the histogram of the nanoisland height distribution (determined for 290 points) presented in Fig. 1, the ensemble of nanoislands becomes more homogeneous: $h = 8.9 \pm 2.3$ nm, the rms deviation is ~26%, and $r = 0.28$–0.32.

According to the Wulff theorem, the equilibrium shape of the 3D nanoislands of PbTe grown on BaF$_2$(111) is a trihedral pyramid with a triangular base and the side faces formed by the intersecting (100) planes corresponding to minimum values of the free surface energy for lead salts [5]. We have also observed the growth of nanoislands with such faceting upon reaching a certain surface coverage ($d > 2$ M L) for the substrate temperatures $T_s > 600$ K (Fig. 2).

Z: 23 nm

XY: 282 nm
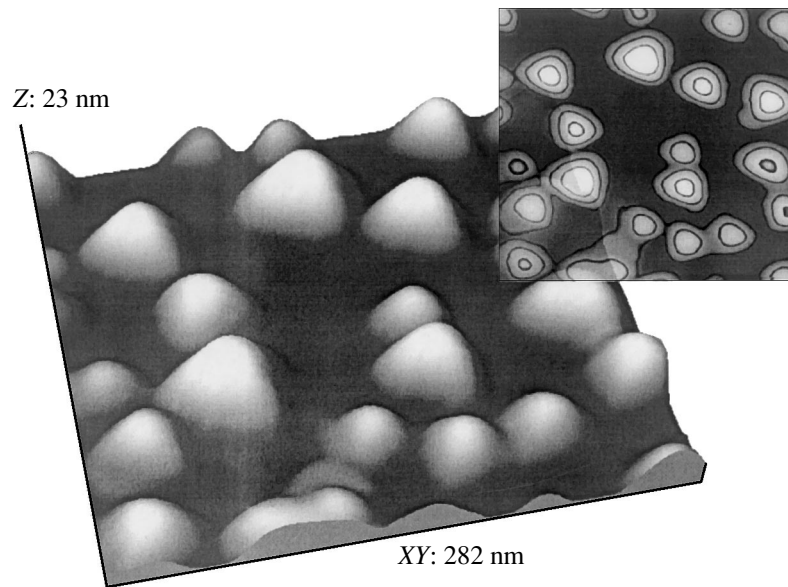
Fig. 2. Magnified 3D and 2D (top view) AFM images of a 282 × 282 nm area of the region imaged in Fig. 1. Vertical scale is indicated in the *Z* axis.

Since the nucleation of nanoislands according to the V–W mechanism in the presence of free sites on the substrate continuously takes place during the growth, the dispersion of nanoisland dimensions in this case is greater than that for the $A^{IV}B^{VI}$ quantum dots grown according to the S–K mechanism [2, 3]. The distribution of 3D nanoislands with respect to size in the case of heteroepitaxial nucleation is determined by their lateral dimensions (*l*), the distance (*D*) between nanoislands [11], and the process of the adsorption and desorption of molecules on the substrate surface. By changing the wall temperature T_w (which determines the degree of supersaturation in the zone of condensation) at a given substrate temperature T_s (which controls the surface diffusion of PbTe molecules), it is possible to provide for a relation between the surface diffusion length λ_α and *D* such that the nanoisland size dispersion will be minimized [3]. The new PbTe molecules arriving at the substrate surface are more readily adsorbed on the nanoislands than on BaF_2 [4], which is confirmed by an increase in the rate of deposition with increasing volume of nanoislands. Thus, if a large number of nuclei were formed within a time period much shorter than the total time required for the formation of an ensemble of nanoislands, the new incident molecules more readily build into the existing nanoislands than form new nuclei. Then, the elastic interaction between nanoislands via the substrate in the case of heterogeneous nucleation for $l \sim D$ must lead to an increase in *r* [11]. Indeed, dense (~8×10^{10} cm^{-2}) arrays of 3D nanoislands with an average height of $h = 10.1 \pm 2.1$ nm formed under conditions close to thermodynamic equilibrium are characterized by $r = 0.4$–0.45.

REFERENCES

1. G. Springholz, T. Schwarzl, W. Heiss, *et al.*, Physica E **13**, 876 (2002).
2. M. Pinczolits, G. Springholz, and G. Bauer, J. Cryst. Growth **201–202**, 1126 (1999).
3. K. Alchalabi, D. Zimin, G. Kostorz, and H. Zogg, Phys. Rev. Lett. **90**, 026104 (2003).
4. S. O. Fereira, B. R. A. Neves, R. Magalhaes-Paniago, *et al.*, J. Cryst. Growth **231**, 121 (2001).
5. A. Y. Ueta, G. Springholz, and G. Bauer, J. Cryst. Growth **175–176**, 1022 (1997).
6. H. Clemens, E. J. Fantner, W. Ruhs, and G. Bauer, J. Cryst. Growth **66**, 251 (1984).
7. G. Bauer, Surf. Sci. **168**, 462 (1986).
8. G. V. Lashkarev, V. N. Vodop'yanov, A. P. Bakhtinov, *et al.*, in *Proceedings of the 5th International Seminar "Nanophysics and Nanoelectronics," St.-Petersburg, 2004,* pp. 18–19.
9. P. Pongratz and H. Sitter, J. Cryst. Growth **80**, 73 (1987).
10. V. P. Zlomanov and A. V. Novoselova, *P–T–x Phase Diagrams of Metal–Chalcogen Systems* (Nauka, Moscow, 1987), p. 280.
11. P. Muller and R. Kern, J. Cryst. Growth **193**, 257 (1998).

Translated by P. Pozdeev